Abstract

The LHC collides two protons beams with an energy of 7 TeV each resulting in a aimed total particle rate of about 10^9 Hz. The particle rate is determined by the production cross section, a natural constant and the luminosity accelerator dependent parameter describing the particle beams. The luminosity depends on the number of particles in each beam linearly and on the transverse dimensions of the particle beam inversely. It increases with the particle beam density and therefore the probability of interactions. To optimize the transverse beams sizes, profile monitors are used to measure parameter depending changes. Within the LHC, three different types of profile monitors are installed: Wire scanner (WS), Synchrotron light monitor and Rest Gas Profile Monitor. The WS monitor is considered to be the most accurate of these monitors and serves as a calibration device for the two others. The WS is an electro-mechanical device which measures the transverse beam density profile in an intermittent way. As the wire passes through the beam, the particle-matter interaction generates a cascade of secondary particles. These are intercepted by a scintillator, which is attached to a photomultiplier in order to measure the intensity of the light thereby produced. The light signal amplitude is proportional to the density of the intercepted beam portion. The acquisitions of the wire position and the intensity signal are synchronized with the particle revolution frequency and are combined to construct the transverse beam density profile. The WS is installed and operated in all circular accelerators of CERN on a daily basis.

The aim of this PhD work is to design an actuator for the new generation of WS allowing to improve the accuracy and the reliability of measurement through higher performances than those currently achievable. These

new performances in particular include a wire travelling speed of up to 20 $m.s^{-1}$ and a position measurement accuracy of the range of $4\mu m$. Other requirements related to interfacing and environmental issues such as radiation, temperature, ultra high vacuum (UHV) and interactions with the beam must also be taken into account. The baseline solution consists in a small diameter rotary brushless synchronous motor with the rotor's magnetic field provided by permanent magnets which is installed inside the vacuum chamber. In order to minimize the out-gassing from the motor, the stator windings exciting the rotor are put outside the vacuum chamber. The air-vacuum interface is made in the magnetic gap through the use of a low magnetic permeability stainless steel wall. In order to perform the motor feedback control loop, a solid rotor resolver measures the absolute angular position. The wire position measurement is performed with an optical fiber based incremental transducer, both transducer are located inside the vacuum. The WS actuator including motor, linear power supply, angular sensors and its control has been designed, sized and validated by simulation and experimental tests. The electrical machines and drives theory has been successfully applied in the aim of developing and implementing an algorithm to control the proposed actuator. The obtained experimental results have been performed on a test bench especially built in the framework of this project and are decisive for its advancement in the forthcoming Long Shutdown 1 of all CERN accelerators in 2013-14.

Abstract

Le LHC met en collision deux faisceaux de protons avec une énergie de 7 Tev chacun, entrainant ainsi un taux de particules d'environ 10^9 Hz. Le taux de particules est déterminé la production d'une coupe transversale, une constance naturelle, la luminosité et un paramètre dépendant de l'accélérateur capable de décrire les faisceaux de particules. La luminosité dépend du nombre de particules dans chaque faisceau linéairement et des dimensions transversales du faisceau inversement. Elle augmente avec la densité du faisceau de particules et en conséquence, la probabilité d'interactions est accrue. Pour optimiser les tailles des faisceaux transversaux, on utilise des dispositifs de contrle de profile, qui permettent de mesurer les changements de paramètres dépendants. A l'intérieur du LHC, trois différents types de dispositifs de contrle des profiles sont installés, savoir le Wire Scanner (WS), le Synchroton Light Monitor et le Rest Gas Profile Monitor. Le WS est considéré comme étant le plus précis de ces trois dispositifs de contrle et sert d'appareil de calibrage pour les deux autres. Il s'agit d'un appareil électromécanique qui mesure l'état de densité du faisceau transversale de faon intermittente. Lorsque le cble traverse le faisceau, l'interaction particule-matière génère une cascade de particules secondaires. Ces derniers sont interceptés par un scintillateur, lequel est attaché un photo-multiplieur, et ce afin de mesurer l'intensité de la lumière ainsi produite. L'amplitude du signal lumineux est proportionnelle la densité de la portion de faisceau interceptée. L'acquisition de la position du fil et celle de l'intensité du signal sont synchronisées avec la fréquence de la révolution de particules puis sont combinées pour construire le profile de densité du faisceau transversal. Le WS est installé et mis en marche dans tous les accélérateurs circulaires du CERN sur une base régulière.

L'objectif de ce travail de thèse est de concevoir un actionneur pour la nouvelle génération de WS permettant d'améliorer la précision et la fiabilité des mesures au moyen de performances plus élevées que celles atteignables jusqu' présent. Ces nouvelles performances comprennent notamment une vitesse de déplacement du fil allant jusqu' $20m.s^{-1}$ et une précision de la position de mesure de l'ordre de $4\mu m$. D'autres conditions préalables liées aux questions d'environnement et d'interface, notamment la radiation, la température, le vide poussé (UHV) et les interactions, doivent également tre prises en considération. La solution de base consiste en un moteur synchrone aimant permanent, dont le champ magnétique du rotor est couplé celui du stator travers la chambre vide. Afin de minimiser le dégazage du moteur, les enroulements du stator qui excitent le rotor sons placés l'extérieur de la chambre vide. L'interface air-vide est créé dans un interstice magnétique travers l'utilisation d'une barrière en inox d'une faible perméabilité magnétique. Pour accomplir la boucle de contrle du moteur, un solide résolveur du rotor mesure la position de l'angle absolu. Les mesures de la position du fil sont réalisées par un encodeur incrémental fibre optique, lequel est également placé l'intérieur de la chambre vide. L'actionneur du WS, comprenant le moteur, l'alimentation linéaire, les capteurs angulaires ainsi que son contrle, a été conu, dimensionné et validé par des simulations et des tests expérimentaux. La théorie des machines électriques et de leur contrle a été appliquée avec succès dans le but de développer et de mettre en uvre un algorithme de contrle de l'actionneur proposé. Les résultats expérimentaux ont été obtenus sur la base d'un banc de test spécialement élaboré dans le cadre de ce projet et sont décisifs pour l'avancement du projet. Ainsi, le nouveau WS sera installé en tenant compte de ces résultats dans le prochain Long Shutdown 1 de tous les accélérateurs du CERN pour l'année 2013-2014.

Acknowledgements

First of all, my thanks are due to the rapporteurs, Prof. Gianpaolo Vitale and Prof. Mohamed El Hachemi Benbouzid, and the examiners, Prof. Pascal Brochet, Prof. Maurizio Cirrincione, Prof. Michel Hecquet, who all were members of the committee of my thesis. Thank you for your interest in my project, for your proofreading of my work, for all your comments and your attention during the oral defense of my thesis. It was a pleasure to have this thesis approved by your committee. Achieving this PhD is probably the most exciting and satisfactory (but also exhausting) challenge of all my studies. These years of research were a journey shared with a number of persons I would like to thank here and without whom this thesis would not have been possible. First and foremost I want to thank my supervisor Bernd Dehning for his dedication of time and knowledge in my thesis project. He continuously advised me and encouraged me throughout my thesis. He brought me constructive critics, ideas and guidelines which were definitely necessary and made my PhD experience stimulating and challenging. I am also thankful to him for his proofreading of my paper and his precious comments. His art of management gave me the necessary space to be innovative and the positive pressure to produce good work. Through our exchanges, I learned a lot on a scientific point of you but also humanly. It was an honor to work under his supervision. A special thank goes to Jan Koopman (1957-2009) who believed in me and offered me the opportunity to live such a great experience, by hosting my project at CERN. Rest in peace. I also would like to extend my gratitude to my colleagues in the BLM section, for our discussions, brainstorming, knowledge sharing, and for the useful advises in every step of the project. Many thanks to Jonathan Emery (my office colleague, direct source of information), Juan Herrenz Alvares (for his valuable competences in mechanics and his great support until the end), Marius Sampinski (for his explanations and translations of physics concepts and his welcome at my arrival at CERN) and Delio Duarte Ramos (for his advices in project management and his mechanical contribution). My years at CERN stay unforgettable thanks to my others colleagues Jos Luis, Giuseppe, Ewald, Christos, William, Claudine, Eva Barbara, Slava, Agnieszka, Christophe, Raymond, Ion, Sophie, Anika, Eduardo, Marcel, Csaba, Aurlien and Julien who shared all my ups and downs, stood all my moods, encouraged and helped me in the completion of this PhD. More generally, my thanks go also to Mike, Madeleine, Mourad, Grard, Roland and Benjamin, and all the other people at CERN, who I interacted with and who helped me during these years of studies. If the completion of my thesis project has been taken place at CERN, its conception has been done within the University of Technology Belfort-Monbliard (UTBM) under the auspices of Dr. Abdesslem Djerdir who has proposed me to carry out my thesis on this subject. From discussions to recommendations, from listening to advises, from encouragement to relief, Dr. Abdesslem Djerdir went with me throughout this project until the end, just like a coach. May he be thanked here for all the time and energy that he has invested, without hesitating to answer me beyond reasonable working hours. His advices went beyond the simple framework of this thesis, he supported me morally and his calmness in every situation helped me a lot to reduce my stress, especially at the very end. It was a great pleasure and a chance to work with him. Many thanks to Dr. Youcef Ait Amirat who covers scientific topics with wisdom. The discussions we had on different chapters of my thesis helped me a lot and his contributions to the chapter Control were valuable. I also would like to thank people who were not in my professional environment but who are my close friends and mentors who helped, guided, assisted and advised me during the completion of this thesis but also during my life. A deep gratitude to Manual Acosta who has always been a mentor since years, thanks to Kerim whose philosophical sentences were like a welcome relief during my scientific studies, thanks to Hamid who's an artist able to bring laughs and lightness in the most difficult moments. Thank you to Hakan and his family for their generosity and sens of hospitality.

An exhaustive list would be too long to be put here, but every friend will recognize him/her in this dedication. A special thank to Leila, this thesis would not have been written without her immense support. She was the rock to rely upon and she supported me throughout the whole time. She was also a powerful source of inspiration and energy. Thank you habibou ! Finally, I express my deepest gratitude to my family for its support and encouragement, and especially to my father who has always been an example of courage, patience, perseverance and uprightness. His strengh was my motivation.

Contents

List of Figures

List of Tables

1

Introduction

The LHC will collide two proton beams with an energy of 7 TeV by each and the aimed total particle rate is about 10^9 Hz. The particle rate is determined by the production cross section, a natural constant and the accelerator dependent parameter luminosity. The luminosity depends linearly on the number of particles in each beam and inversely on particle beam transverse dimensions. It is increasing with the particle beam density and therefore the probability of interactions. To optimize the transverse beam sizes, profile monitors are used to measure parameter depending changes. In the LHC three different types of profile monitors are installed, Wire scanners, Synchrotron light monitors and Rest Gas Profile Monitors. The wire scanner monitor is considered to be the most accurate of these monitors and serves as a calibration device for the other one. Its application for the circulating beams is limited to lower beam intensities due to the heat deposition of the particle beams in the wire and of secondary particles in superconducting magnets. A wire scanner is an electro-mechanical device which measures the transverse beam density profile by means of a thin moving wire targeted in an intermittent way. As the wire passes through the beam the interaction generates a cascade of secondary particles. These are intercepted by a scintillator, coupled with a photomultiplier, which measures the intensity of the light thereby produced. The light signal amplitude is proportional to the intercepted beam portion. The acquisitions of the wire position and the intensity signal are synchronized with the particle revolution frequency and are combined in order to construct the transverse beam density profile. Wire scanners are installed and operated in all circular accelerators of CERN on a daily basis. However, they have several drawbacks: For high intensity beams the energy deposited by the incident particles on the wire, this situation can also arise from the energy transferred by the beam to the wire through its accompanying electromagnetic field. Another disadvantage lies in the inaccuracy of position measurement primarily due to vibration on the wire and the mechanics and finally bellows vacuum leakage.

The new performances level needed for the Large Hadron Collider (LHC) at CERN define a very challenging set of specifications combining high acceleration motion with very accurate position measurement, in a difficult environment of temperature and ionizing radiation.

The baseline solution consists in a small diameter rotary brushless synchronous motor with the rotors magnetic field provided by permanent magnets, installed inside the vacuum chamber. This rotor is supported on a shaft by roller bearings with materials and solid lubricants to be selected for low outgassing and friction characteristics in a vacuum environment. Two arms are attached to the same shaft on which the wire is stretched. In order to minimize the outgassing from the motor, the stator windings which excite the rotor are placed outside vacuum chamber. The air vacuum interface is made in the magnetic gap through a low magnetic permeability stainless steel wall.

The aim of this doctoral thesis work is the design and the construction of a high acceleration motion actuator, its control for a fast wire scanner and qualification tests of the complete actuator (electrical motor, position detector and controller assembly), from theorical study to experimental validating tests. Through this PhD thesis, we present the approach applied to achieve these objectives and the tools developed, results, their potential but also their limitations:

- The first Chapter is introduction where we give briefly the context and the objectives of this work, and the plan by which the ideas of this manuscript are exposed.

- In the second chapter, we expose the work principle of accelerators chain and show how a particle beam size can be measured. So, different types of wire scanner already working at CERN are described, as well as the issues met by using them. Then a focus is made on the drawbacks of these devices. Thus, the specifications to improve the available wire scanner device are expressed in terms of accuracies of the position and speed travel of the wire, but also in terms of environment constraints, that is to say high temperature, ultra high vacuum, radiation and electromagnetic compatibility. Finally, the conceptual design solution proposed to answer all these constraints presented.

- The Chapter 3 presents the design of the actuator dedicated to move the fast and high accuracy Wire Scanner system. This system has to resist a bake-out temperature of 200oC and ionizing radiation up to tenths of kGy/years. The requirements imply a maximum angular speed of 200 $rad \cdot s^{-1}$, an acceleration of 40 000 $rad \cdot s^{-2}$ and an angular position measurement accuracy of 5 $arcseconds$. The system must deal with extremely low vibration and low electromagnetic interferences. So, after exposing the main characteristics of the selected motor and its power supply based the performances of the designed actuator are investigated through simulations using Matlab/Simulink software.

- The Chapter 4 is focused on the selection and the experimentation of the high accuracy angular position of the Wire Scanner. It will be shown that the accuracy of this sensor is no less than 25 rad r.m.s during the scanning part of the stroke as it was expected by the wire scanner specifications. The design process of this sensor including a technological comparative study of five position sensors, a flexible test setup development and validating experimental tests will be highlighted.

- In the Chapter 5, we discuss the proposed control algorithm of the Wire Scanner actuator. After exposing this control global diagram and explaining its main loops, we present a theoretical study on the different regulators to show how these devices are designed in the framework of this thesis work. For a more realistic control of the WS system, we carry out a vibration study on the fork-wire system in particular to optimize the speed and position profiles with respect to the wire vibrations. We finish this chapter with some results of simulations to check the validity of the proposed algorithm of control notably in terms of precision and robustness.

- The Chapter 6 is entirely dedicated to the experimental test bench especially developed to check the validity of our design process. First, all the elements of the setup are described through the presentation of their technical characteristics and the identification of their physical parameters used for modeling and control. Once all the models parameters identified, the control algorithm is simulated under Simulink software and implemented on the DSPACE device to show the actuator behaviors according to the expected functionalities. Also, the obtained experimental and simulation results are compared to each other in order to validate the design of the actuator and its controller.

- The Chapter 7 is the general conclusion highlighting the initial objectives of this research work as well as the key points of the results obtained after three and a half years of PhD study.

- In the last Chapter, we give some Appendices to help the readers of our manuscript to more understand certain technical and theoretical choices used in the previous chapters.

2

Context of the study and specifications of the Wire Scanner actuator

This PhD thesis has been carried out at the European Organization for Nuclear Research (CERN) which is one of the worlds largest and most respected centers for scientific research in the area of fundamental physics and the structure of matter at the smallest scale. The electrical engineering technological research meets a practical need for the greatest experience in the world of nuclear physics, namely the CERN's LHC (Large Hadron Collider at the European Organization for Nuclear Research). Although at the forefront of technology, this experience has constantly needed to improve its performance notably using the latest technological developments in the field of electrical engineering. In this context, the present research work has as main objective to lead a project of improvement of the actuator wire scanner used for measurements of the accelerated beam inside the circular tunnel of the LHC. Firstly, this chapter exposes the work principle of accelerators chain and shows how a particle beam size can be measured. So, different types of wire scanner already working at CERN are described, as well as the issues met by using them. Then a focus is made on the drawbacks of these devices including the relatively insufficient repeatability of the wire position determination, the limited life time, the strong vibrations of the wire and fork and the problem of melting/sublimating of the wire. Thus, the specifications to improve the available wire scanner device are expressed in terms of accuracies of the position and speed travel of the wire, but also in *terms of environment constraints, that is to say high temperature, ultra high vacuum, radiation and electromagnetic compatibility. Finally, the conceptual design solution proposed to answer all the previous constraints is briefly presented with its principal advantages compared to classical designs but also with the challenges implied by it. Through this thesis work, technological bolts have been raised, as it is detailed in the next chapters.*

2.1 CERN - European Organisation for Nuclear Research

CERN, the European Organization for Nuclear Research (Fig. 2.1), is one of the worlds largest and most respected centers for scientific research. Its main research activity is fundamental physics and the structure of matter at the smallest scale. At CERN, the worlds largest and most complex scientific instruments are used to study the basic constituents of matter, the fundamental particles. By studying what happens when these particles collide, the laws driving the interactions of the particles are determined.

Figure 2.1: Aerial view of CERN.

The instruments used at CERN are particle accelerators and detectors. Accelerators boost beams of particles to high energies before they are made to collide with each other or with stationary targets. Detectors observe and record the results of these collisions.

Founded in 1954, the CERN Laboratory sits astride the FrancoSwiss border near Geneva. It was one of Europes first joint ventures and now has 20 Member States.

Currently, the key objective of CERN is to improve the performances and fully exploit the potential of the worlds largest research instrument, the Large Hadron Collider (LHC).

2.2 The LHC Injector Chain

CERN's accelerator complex consists of many different types of linear and circular accelerators and interconnecting transfer lines. At the beginning of the chain, the protons are taken from hydrogen gas jet and accelerated in the LINAC2 to the kinetic energy of 50 MeV and transferred to the Proton Synchrotron BOOSTER (PSB)(Fig. 2.3. The PSB accelerates them to 1.4 GeV and sends them to the Proton Synchrotron (PS). After having reached 25 GeV in the PS, the protons are injected to the Super Proton Synchrotron (SPS) and accelerated to 450 GeV. Finally, they are transferred to the two LHC rings and accelerated for 11 minutes to the energy of 4 TeV. It is foreseen to accelerate to the beam energy of 7 TeV after the stop in 2013 and 2014. The LHC is also accelerates and collides lead ions (Pb^{82+}) with the kinetic energy of 2.8 TeV per nucleon. These ions are produced in the LINAC3 and accumulated in the Low Energy Ion Ring (LEIR). Afterwards, they are injected into the PS and follow the same path as the protons up to the LHC.

Several injections from the smaller accelerator are generally needed to fill the subsequent machine so the filing of one LHC ring to the nominal intensity should take in total 4 minutes and 20 seconds. Once the nominal energy is reached, the particles should remain circulating in the LHC and colliding inside the four main experiments (ATLAS, CMS, LHCb and ALICE) for several hours (Fig. 2.2). There are two other smaller experiments in the LHC: the LHCf which is installed close to the ATLAS interaction point and the TOTEM which is nearby CMS. The complex of the CERN accelerators is very versatile and far from being just the injectors to the LHC. Most of the machines have their own dedicated experimental areas using fixed targets to explore wide range of physics phenomenon. The beam types range from high intensity neutrons for the n-ToF experiment, decelerated anti-protons for anti-matter production to neutrino beams sent to Italy by the CNGS project. Fig. 2.3 presents a general overview of the system of consecutive accelerators including the LHC.

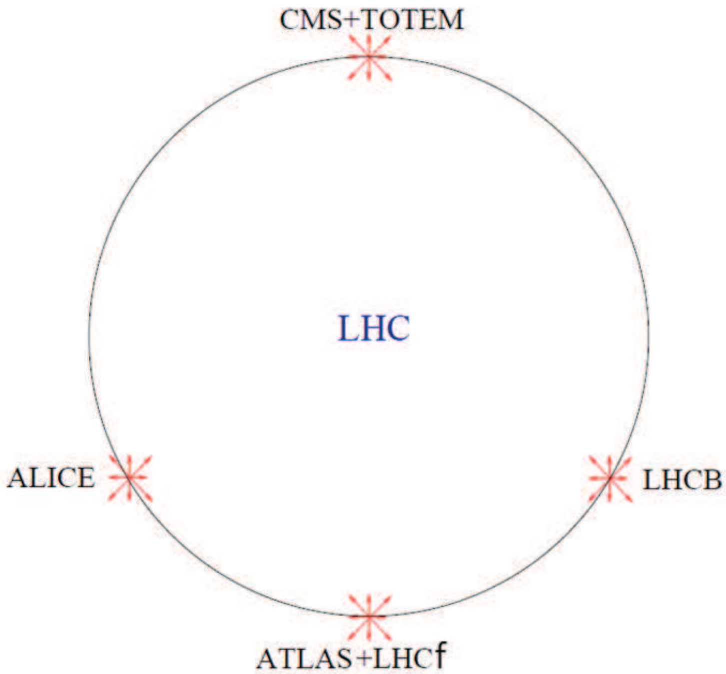

Figure 2.2: Location of the five experience zones where the proton beams are broad into collision around the LHC ring. ATLAS and CMS are optimized for all purpose proton-proton collision particles analysis, LHCb is optimized for the b-quark study, ALICE for heavy ion collisions study and LHCf and TOTEM for low angle proton-proton scattering.

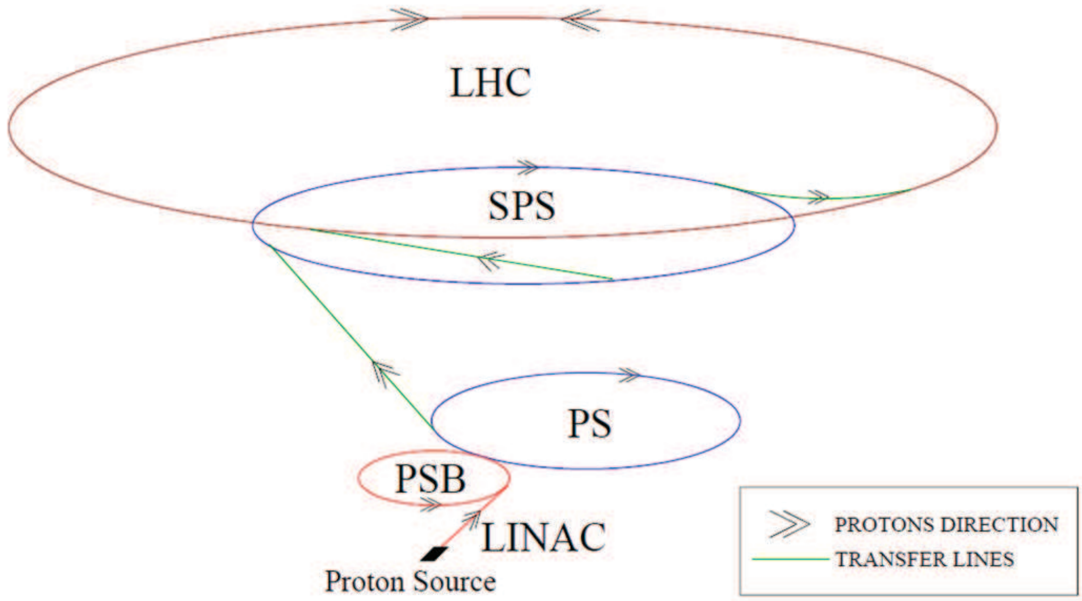

Figure 2.3: The LHC Injector Chain.

2.3 Luminosity

In a collider two particule beams, which circulate in opposite directions, are brought into head-on collisions in interaction regions. In this region, the interaction event rate $\dot{n}$ (i.e. the number of interactions per second) is proportional to the particle cross section σ according to:

$$\dot{n} = L \cdot \sigma \tag{2.1}$$

The factor of proportionality L is called *Luminosity* and is expressed in units of $cm^{-2}s^{-1}$.

When two bunches containing n_1 and n_2 particules, collide at zero crossing angle, with a repetition frequency f, then the luminosity is given by (Fig. 2.4)

$$L = f \frac{n_1 n_2}{4\pi\sigma_x\sigma_y} \tag{2.2}$$

where σ_x ans σ_y are the parameters describing the width of the Gaussian beam profile in x and y plan (Fig. 2.6). This shows that the luminosity is inversely proportional to the beam size at the collision points. The beam size must be as small as possible to maximize the number of interaction events.

The design luminosity of LHC is $L = 10^{34}\ cm^{-2}s^{-1}$ and the total hadronic cross section is $8.10^{-26}\ cm^2$. Consequently the event rate equals to $8.10^8\ s^{-1}$. Fig. 2.5 shows the evolution of the luminosity in the LHC during 2011.

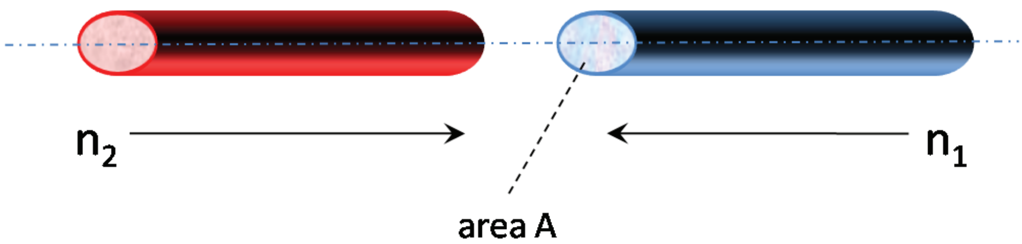

Figure 2.4: Two bunches containing n1 and n2 particles in an interaction region. The increase in the instantaneous luminosity is due to the optimization of the beam parameters during the running period.

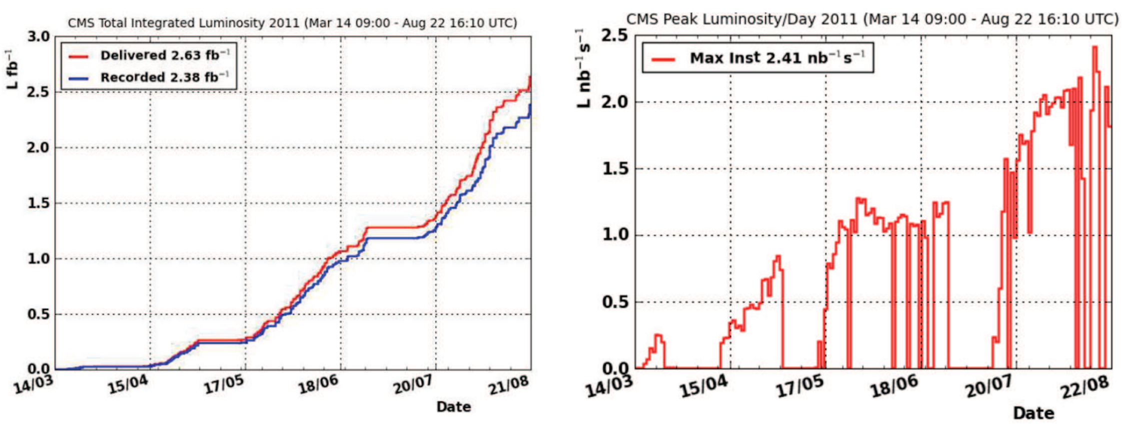

(a) (b)

Figure 2.5: Evolution of the (a) integrated (b) instantaneous luminosity during 2011.

2.4 Beam size measurement

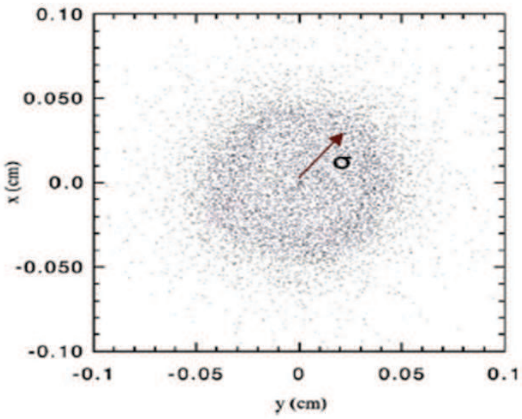

Figure 2.6: Indicated transversal beam intensity scatter plot is the 1 σ radius which contains 62% of all particles.

The strong dependence of the interaction rate on the beam sizes motivates the requirement of an accurate measurement of the beam profiles.

CERN's accelerators are equipped with several beam profile monitors for measuring transversal beam density profile using phenomena as:

- secondary emission (SE)
- production of secondaries and Bremsstrahlung
- ionization of rest gas
- synchrotron light

These profile monitor types include (6):

- Beam Wire Scanners (BWS), which consist of thin wires intercepting the transverse beam distribution in a multi-turn scan during which the wire position is correlated with an intensity signal (secondary particles showers originating from beam particle interaction in the wire).
- Screen monitors, that provide 2D beam images by means of scintillating or Optical Transition Radiation (OTR) screens intercepted by the beam and observed with a TV camera detectors (Fig. 2.7, a).

- Ionization Profile Monitors, which provide a 1D profile (either horizontal or vertical depending on the monitor geometry) of the gas ionization at the beam passage. Electrons from the gas ionization are accelerated transversally in a high voltage field electrodes and collected to an amplifying micro-channel plate coupled to a phosphor and imaging system (Fig. 2.7, b).

- Synchrotron Radiation Monitors, that provide a 2D profile from the photons emitted by the beam in a bending section (Fig. 2.8).

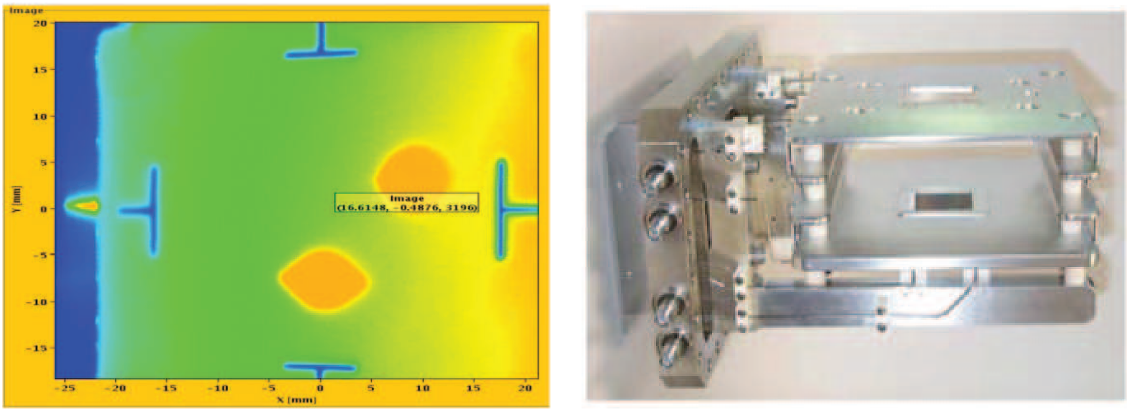

(a) (b)

Figure 2.7: (a) The first full turn in the LHC as seen by the screen monitor system (10/9/2008), (b) Picture of the Ionization Profile Monitors high voltage electrodes.

For the circulating LHC beam, the instrument of reference used for calibration of the other monitors is the BWS. However, the heat deposition in the wire and the possibility of quenching[1] the downstream superconducting magnets with the particle shower produced limit the use of this monitor to a few nominal bunches at 7 TeV (7).

2.5 Beam Wire Scanners (BWS)

2.5.1 Overview

Beam Wire Scanners are described as electro-mechanical devices which measure the transversal beam density profile by means of a moving thin wire passing through the

[1] A quench is an abnormal termination of magnet operation that occurs when part of the superconducting coil enters the normal (resistive) state.

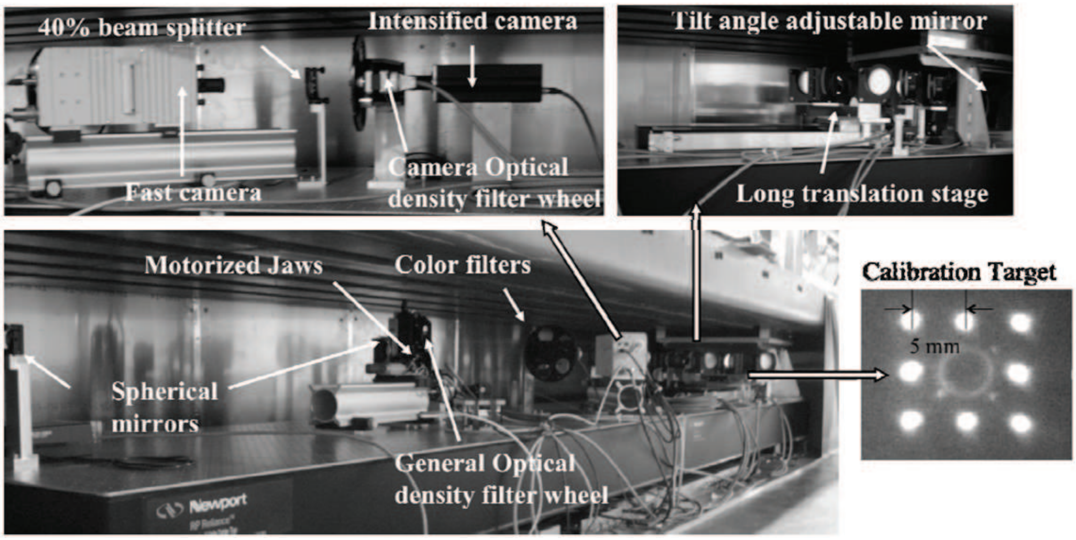

Figure 2.8: The LHC Synchrotron radiation monitor.

particles beam intermittently. When the wire passes through the particles beam, the interaction creates secondary particles showers with an intensity proportional to the number of beam particles traversing at the position of the wire. The secondary particles are intercepted by a high-speed scintillator positioned downstream of the wire and coupled with a photomultiplier, which amplifies the intensity of the light produced (Fig. 2.9, a). The acquisitions of the wire position and the signal intensity are combined in order to reconstruct the transversal beam density profile.

Another way to acquire information about the particle transversal distribution is to measure the current flowing through the wire. If the wire is made with a conductive material, the traversing particles knock out wire electrons near to its surface (secondary electron emission). This current is also proportional to the number of beam particles present at the wire position (Fig. 2.9, b).

Two BWS are used to measure beam transversal profiles in horizontal and vertical plans . One wire is horizontal and travels vertically through the beam, producing a vertical profile. The vertical wire that travels horizontally through the beam produces the horizontal beam profile.

At CERN, Beam Wire Scanners are used in the PSB, PS, SPS and LHC rings (Fig. 2.3). The LHC has 8 wire scanners (including 4 spares), one for each plane (horizontal and vertical) and for each beam and are capable to measure the profile of

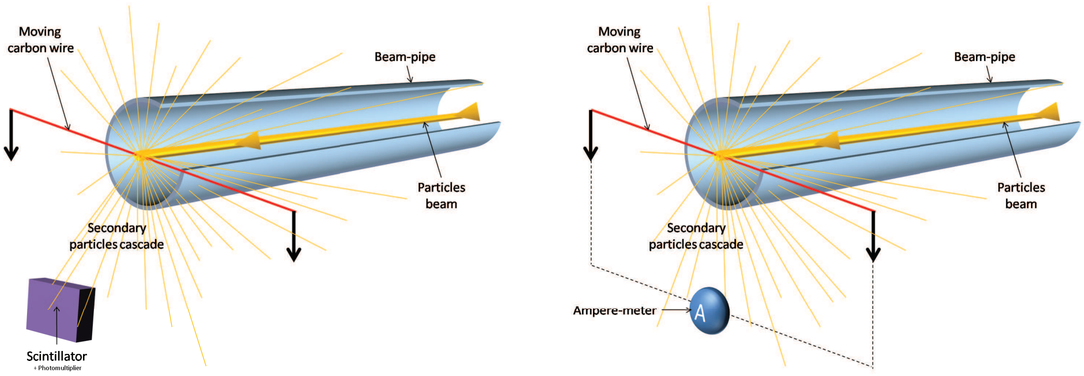

(a) (b)

Figure 2.9: (a) The secondary particles are intercepted by a high-speed scintillator positioned downstream of the wire, (b) The particles hitting the wire create secondary emission electrons generating a current on the wire.

each individual bunch. They are also used in the main hardron accelerator facilities, at Fermilab (Chicago, U.S.A.), Brookhaven National Laboratory (Long Island, U.S.A.), Los Alamos National Laboratory and DESY (Hamburg, Germany) (1).

Different generations of WS have been developed and improved around the world during more than 20 years. We only list hereafter the BWS types used at CERN, then one of them is described more in detail .

2.5.2 CERN Beam Wire Scanners types

CERN Wire Scanners can be classified in three main types related to their scanning movements:

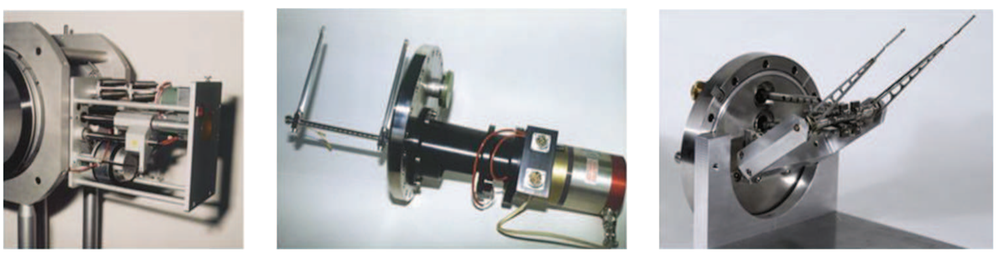

(a) (b) (c)

Figure 2.10: CERN Beam Wire Scanners: a) the linear displacement monitor, b) the rotatif movement monitor, c) the pendulum movement monitor called Fast Wire Scanner.

- the linear displacement monitors (Fig. 2.10, a) at a maximum speed of 1 ms^{-1}, using d.c. motors and a linear potentiometer or an optical linear transducer ,
- the rotatif movement monitors (Fig. 2.10, b) at a maximum speed up to 6 ms^{-1}, using d.c. motor and potentiometer angular position sensor,
- the pendulum movement monitors (Fig. 2.10, c) for speeds of up to 20 ms^{-1}, using d.c. motor and potentiometer angular position sensor.

All these types have in common the fact that the scanning movement is driven by a motor placed outside the vacuum chamber. Then, this movement is transmitted through the vacuum chamber by means of a bellows. This solution was chosen to limitate the complexity of introducing coils inside the vacuum and the issue of outgazing.

2.5.3 Presentation of the Fast Wire Scanner

In order to have an exemple of BWS system design, one of them is descibed hereunder. It is usually called "Fast Wire Scanner" (Fig. 2.11) and is used in the PSB and PS.

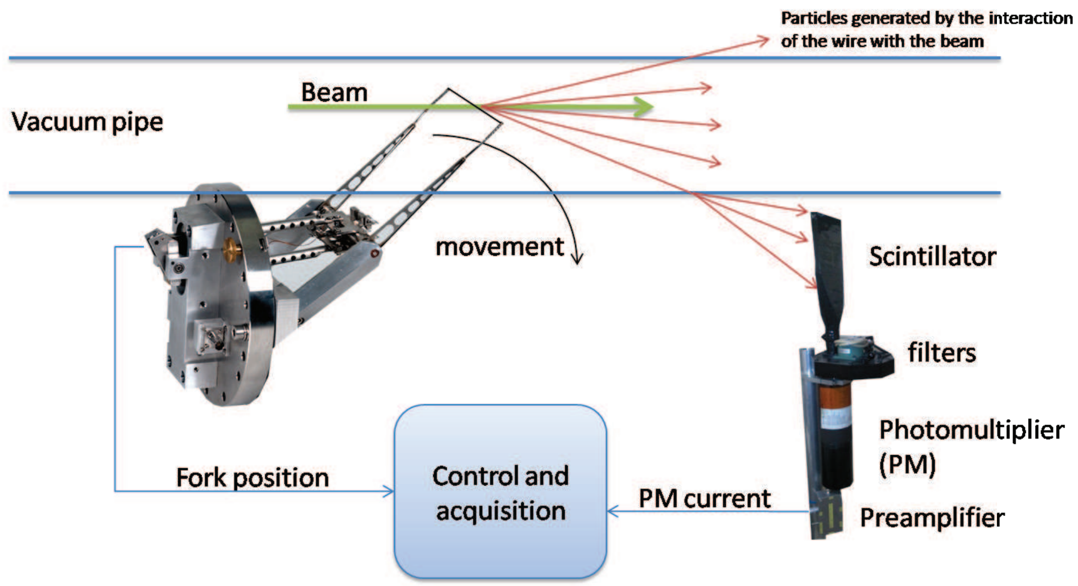

Figure 2.11: Working principle of the wire scanner.

2.5.3.1 Mechanism

A DC motor (400W) with a low inertia creates a rotation which is transmitted to the parts inside the vacuum chamber by a plate and two push-pull rods connected to the mobile end-flanges of two metallic bellows with a stroke of 7mm. A potentiometer is used as angular position sensor directly mounted on the motor axis.

Four rolling tapes around the cylindrical tube convert a 180^o rotation of the motor into a 130^o rotation of the fork support. This corresponds to the angle between the 'down' and 'up' position (Fig. 2.12).

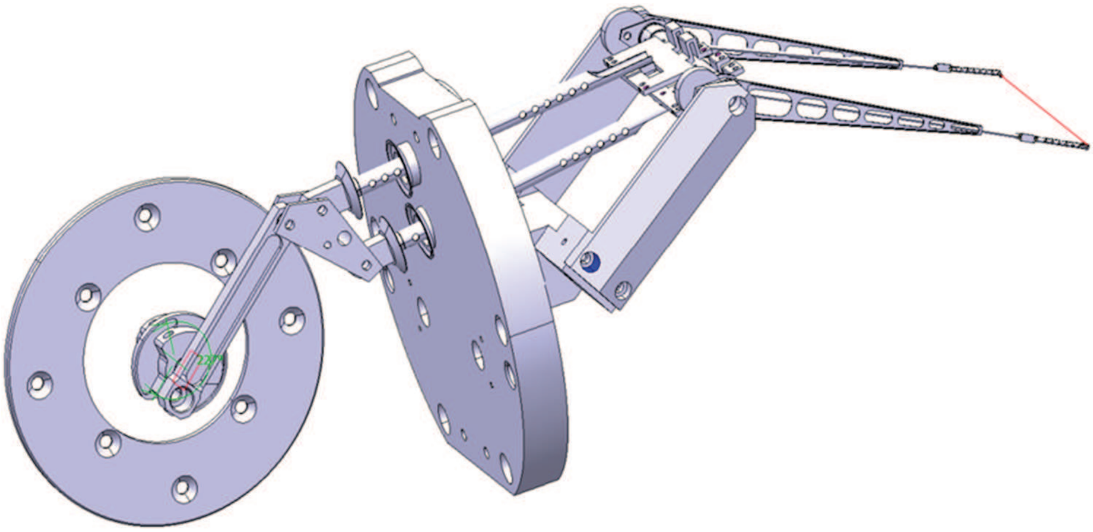

Figure 2.12: Diagram of the fast wire scanner mechanism.

The arms of the fork are build up with standard stainless-steel tubes of a 2 mm outside diameter, and a 0.25 mm wallthickness. At the ends, short flexible parts hold the carbon wire streched.

2.5.3.2 Wire position determination

The position of the motor shaft is measured by means of a precision rotary potentiometer which has a differential voltage read-out in order to increase the noise immunity along the long cablings. The voltage is amplified through a preamplifier, then digitalized by a 16-bits ADC before being stored in a 256k memory block. To overcome errors due to mechanical imperfections and electronic offsets, the uncertainties are determined by a laboratory calibration setup. The calibration method is based on a substitution of the particule beam by a laser beam whose position is well known. The wire scanning through the laser beam creates a shadow detected by a photo detector. Correlating the measured peak positions with the laser beam position allows the creation of lookup tables with calibrated positions of the wire perpendicularly to the beam which is implemented in a lookup table (8).

2.5.3.3 Driver and power converter

For electromagnetic interference reason a linear converter is used instead of a switching converter. The linear power supply (Fig. 6.19) is based on a bridge of two PA50, 40 A, 100 V linear power operational amplifiers, featuring 200 kHz of power bandwidth, a 50 V/s slew rate and a 400 watts of internal power dissipation.

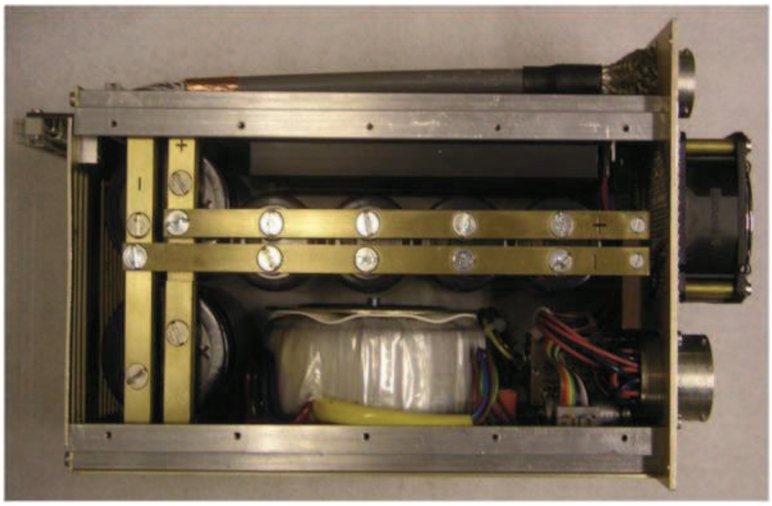

Figure 2.13: Compact linear power supply of the wire scanner. One left sidethe high charge capacitors are visible.

An integrated capacitors based energy storage unit allows to balance the peak power during the milliseconds scale scans.

2.5.3.4 Motion Control Card

The wire speed is selectable among three values 10, 15, 20 m/s. The wire position is sampled synchronously with the current of the photomultiplier at constant frequency in the PS Booster ring or synchronously to the revolution frequency of the beam PS ring.

An analog position control loop is implemented on a removal mezzanine card.

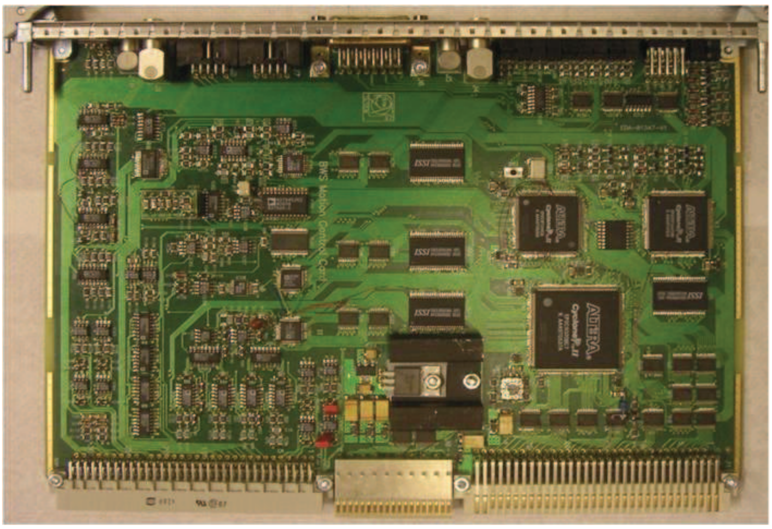

Figure 2.14: Wire scanner motion control board with 3 FPGA for digital signal treatment.

The Motion Control Card (MCC) (Fig. 2.14) controls the motion of the wire scanner by comparing the measured position with the requested position profile. The error is multiplied by a proportional (P) controller which sends the control voltage to the motor driver.

The software in the MCC waits for triggers on its parallel input lines to power up the system and to step through position profile table defining the motor voltage through its DAC module.

The MCC signal acquisition chain of the photomultiplier current digitalize its signal with an ADC after passing through a logarithmic amplifier to extend the dynamic range of the 14 bits initial data width. The software convert it back on a linear scale for display.

2.5.3.5 Scintillator and photomultiplier

The secondary particles produced by the beam-wire interaction are detected by a scintillating material which produces photons. The scintillator is coupled to a photomultiplier tube (PMT) which has two basic stages: the conversion of photons into electrons and the electron multiplication which is enhances the signal level in order to improve the signal over noise ratio.

2.5.4 Fast Wire Scanner limitations

Wire scanners have some drawbacks:

- The complexity of the mechanical system to move the wire is limitating the repetability of the wire position determination (it has only an indirect measurement of the fork position),
- Significant aging of the bellows after 6000 scans. A study for the improvement has been performed and in order to reach 100 000 scans. Conclusive results during 2011 have drove the complete exchange of this bellows in the PS,
- Inaccuracy of position measurement due to wire and fork vibration,
- For high intensity beams the energy deposited by the incident particles on the wire may be suficient to melt or sublimate the wire; this is particulary true for very small beams, in which case the energy transferred from the beam to the wire has potentially damaging effects,
- The wire can melt or sublimate also due to energy transferred by the beam to the wire by means of electomagnetic field coupling. The use of ferrite has reduced this effect in the current design.

2.6 General specification

2.6.1 Wire position accuracy requirement

The beam size measurement requirement for the LHC beams is derived from consideration of minimal observed beam size changes and the absolute accuracy needed for the luminosity determination.

The accuracy and reproducibility should be better as 1% (δ^{rel}) (1)on the beam size determination.

This error consists of a systematic (μ_σ) and statistical (σ_σ) contribution according to:

$$\delta^{rel} = \mu_\sigma \pm \sigma_\sigma \tag{2.3}$$

Assuming that the beam profile is parameterized by a Gaussian distribution only some measurements along the distribution (*bins per sigma*), expressed in term of *spacial resolution* are sufficient to fit with a Gaussian function and determined the measured beam size (Fig. 2.15).

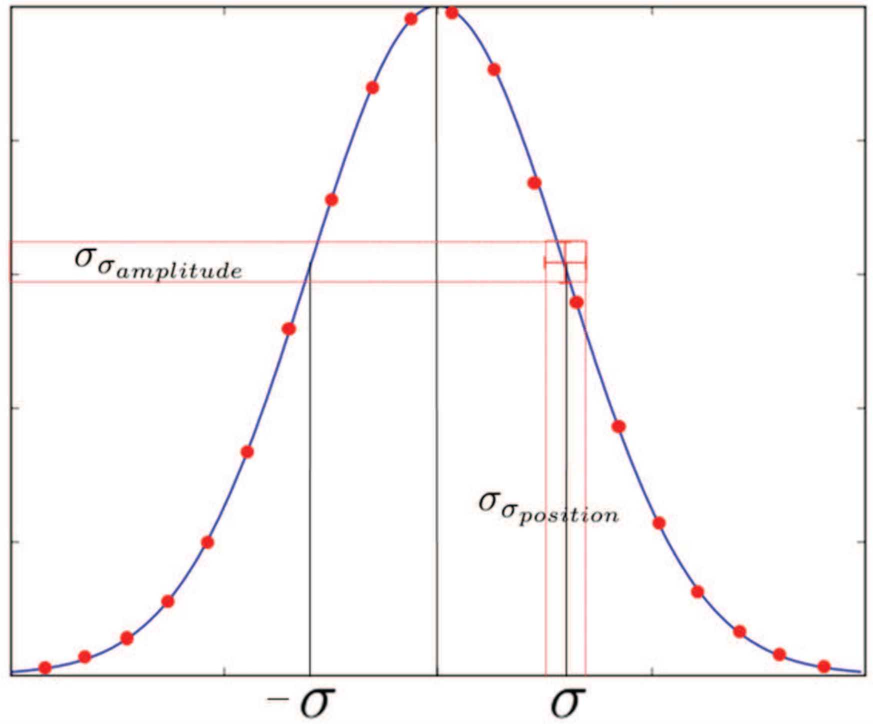

Figure 2.15: Beam Gaussian distribution fitted from spacing of 3 bins per sigma.

In this demonstration we assume a spacial resolution of 3 *bins per sigma* which gives a spacing between two position measurements of

$$res_{min} = \frac{\sigma_{LHCmin}}{3} \approx 54\ \mu m \tag{2.4}$$

With σ_{LHCmin}, the minimum beam size expected in the LHC which is equal to 160 μm.

We assume that the systematic error can be cancelled by calibration and we can say that:

$$\mu_\sigma \approx 0 \tag{2.5}$$

The *statistical error* has contributions from two main sources, the error on the transposed amplitude signal, $\sigma_{\sigma'_{amplitude}}$ (Fig.r̃efbinspersigma), i.e. caused by from photomultiplier and the error on the position signal, $\sigma_{\sigma_{position}}$. Assuming that these errors are random and uncorrelated they can be added quadraticaly:

$$\sigma_{\sigma}^2 = \sigma'^2_{\sigma_{amplitude}} \pm \sigma^2_{\sigma_{position}} \tag{2.6}$$

The required beam width measurement accuracy is estimated by assuming both error contribution should be equal and with a realistic amplitude error contribution.

From Fig. 2.16 and considering a Signal to Noise Ratio (SNR) of 100 on the photomultiplier, the beam size relative statistical error would be:

$$\frac{\sigma'_{\sigma_{amplitude}}}{\sigma'_{amplitude}}(SNR_{amplitude} = 100) = 0.005 \tag{2.7}$$

Assuming that the error contribution from amplitude and position are equal, 0.5%. From Fig. 2.17 for 0.5% relative statistical error on the position, the acceptable SNR on the position determination would be:

$$SNR_{position}(\frac{\sigma_{\sigma_{position}}}{\sigma_{position}} = 0.005) \approx 50 \tag{2.8}$$

Finally, we obtain a maximum allowable statisticalrms error on the position of

$$\Delta_{position} = \frac{\sigma_{LHCmin}}{SNR_{position}(\frac{\sigma_{\sigma_{position}}}{\sigma_{position}} = 0.005)} = 3.2\mu m \tag{2.9}$$

2.6.2 Wire travelling speed requirement

The travelling wire speed requirement is determined to overcome two critical issues.

The particle losses generated by wire-beam interaction could compromise the LHC availability if they provoke quenches of superconducting magnets. In order to investigate the quench limits for this loss mechanism, a quench test using a wire scanner has been performed and is described in (7).

Moreover, the energy deposited by the incident particles on the wire might be sufficient to damaged the wire. The wire can also be destroyed by the energy transferred by the beam to the wire through its accompanying electromagnetic field. A numerical model of heat flow with beam-induced heating and various cooling process for the

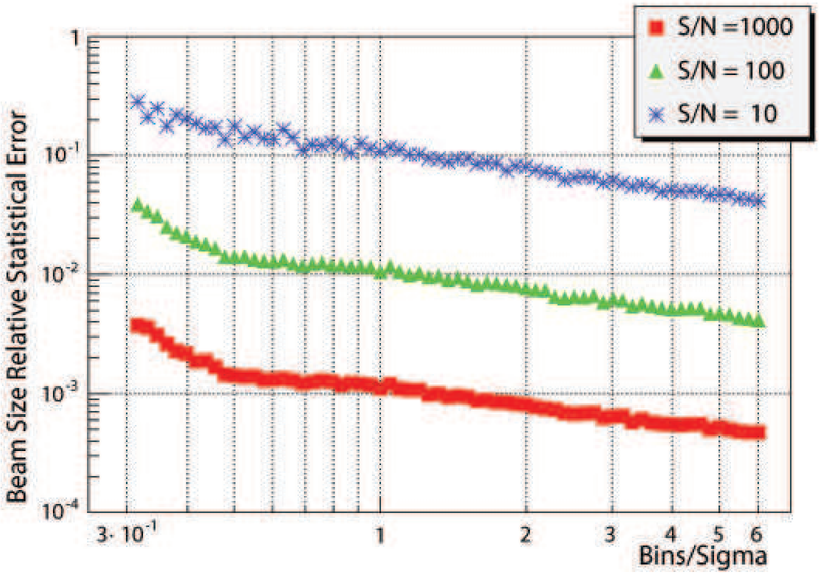

Figure 2.16: Relative statistical error as function of resolution and random noise on the amplitude signal (N events=1.10^8). The beam profile peak is at the bin center (1).

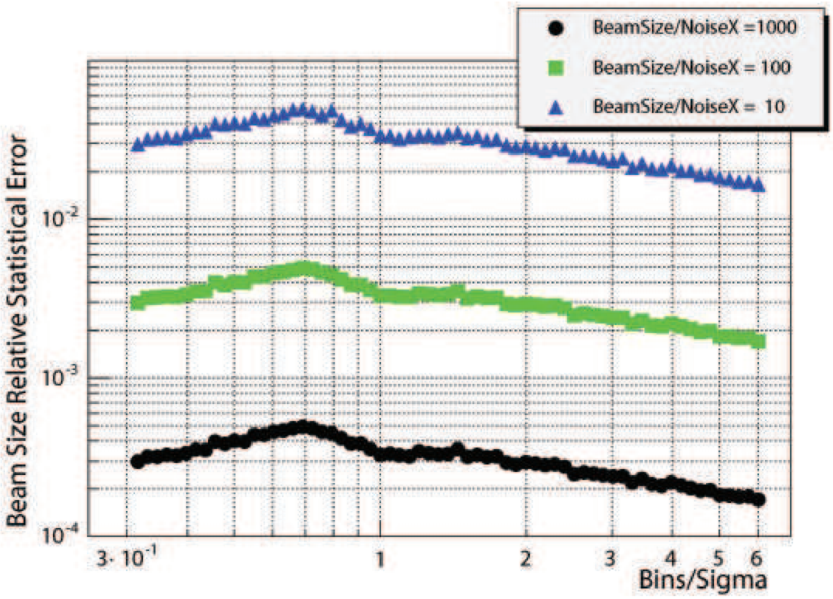

Figure 2.17: Statistical error as function of resolution and random noise on the position (x) signal (N events=1.10^8) (1).

carbon wire passing through a particle beam has been elaborated. Heating of the wire due to the beam-induced electromagnetic field has been taken into account. An estimation of the wire sublimation rate has been made. Then the model has been tested on SPS, LEP and Tevatron Main Injector (postmortem) data (2).

An increase of the scan speed would decrease the time of wire exposition to the particle beam and therefore the energy deposited in the wire. Fig. 2.18 shows the safe area of wire velocity according to the fraction of the full LHC beam. It is shown that increasing the wire speed to about 20 $m.s^{-1}$ would allow to scan full LHC beam at collision energy (7TeV). This value will be take as reference in term of wire traveling speed requierement for the new wire scanner design.

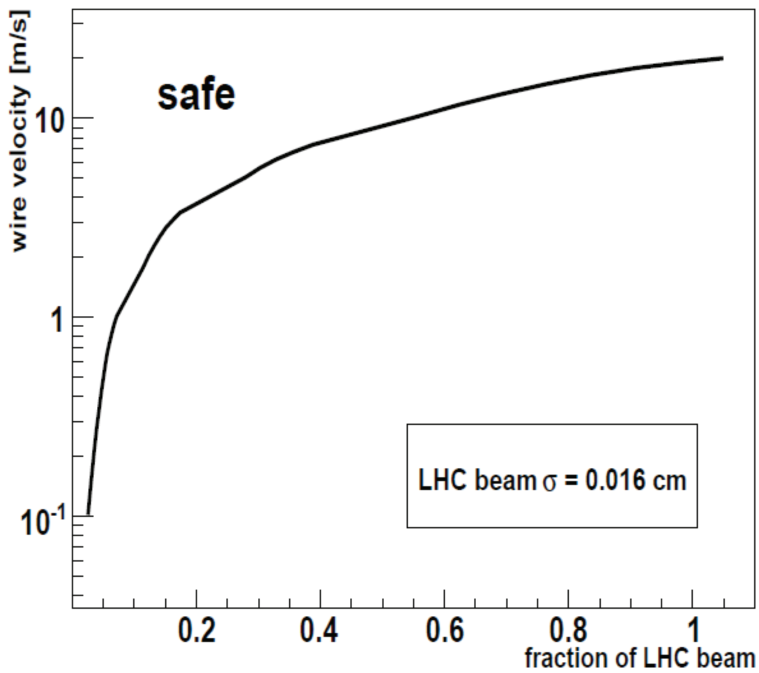

Figure 2.18: The region of safe operation of the wire scanner for LHC beam at collision energy (2).

2.6.3 Reliability / Safety improvement

The life time of the existing systems is limited by the bellows which link the outside motor driven movement into the part of mechanic located inside the vacuum tank. The mean time between failures of the bellows are between 6000 scans up to 100 000 scans for a last version of the system.

2.6.4 Environmental constraints

CERN equipment is subject to hard environmental constraints summarised in the Fig. 2.19 according to the localisation.

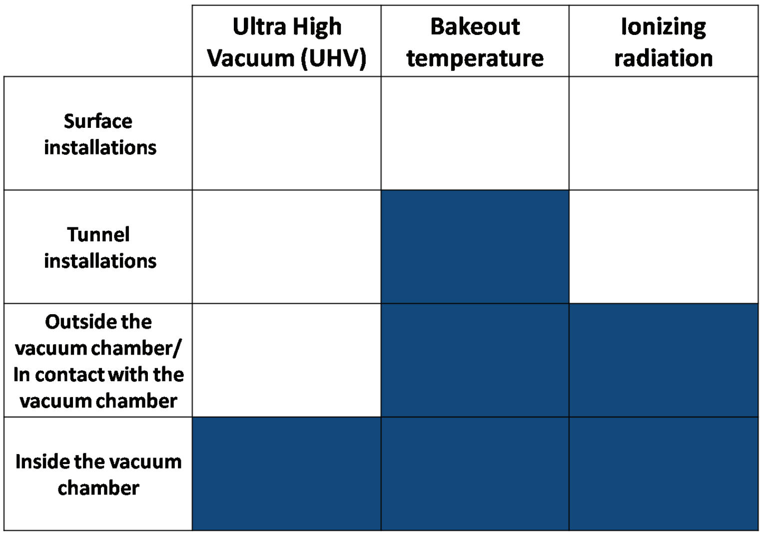

Figure 2.19: Environmental constraints versus localization.

2.6.4.1 Ultra High Vacuum

The pressure in the vacuum chamber is less than 10^{-8} Pa in the case of hadron storage rings in order to get such a low pressure, the main criteria are a low gas desorption rate and no penetration of gases from the outside to limit to the maximum the interation of the beam with the matter. So, elements, which are exposed to vacuum, must have, after bakeout, a total outgassing rate not exceeding 10^{-9} $Pa.m^3.s^{-1}$.

In addition to these properties the material should fulfil some further criteria (9):

- The material for the vacuum envelope must withstand the atmospheric pressure. This favours a material with a high modulus of elasticity and high mechanical strength.
- Since Ultra High Vacuum (UHV) systems are baked, the used materials should have a negligible equilibrium pressure at the foreseen baking temperatures. Thus metals like zinc, magnesium or lead, or alloys containing these, which have a significant vapour pressure at relatively low temperatures, should not be used.

2.6.4.2 Bake-out temperature

The WS system will operate at room ambient temperature; however, every exposure of the vacuum chamber to atmosphere requires a subsequent vacuum conditioning comprising a thermal cycling at high temperature. The elements installed in the vacuum chamber or in contact with it must withstand thermal cycles at 200^oC during 24 hours.

2.6.4.3 Radiation

All components installed in the tunnel must be resistant to a cumulated ionizing radiation dose of 20 kGy (roughly 1 kGy/year). Therefore, electronics need to be installed at the surface, which implies cables up to 250 m length.

2.6.4.4 Electromagnetic compatibility consideration

Wire scanners will be mounted in Electromagnetic Interference (EMI) sensitive environment. A special care must be take during the design of the power stage to minimise the transmission of high frequency that could induce perturbations on the nearby cablings.

2.7 Conceptual design solution

2.7.1 Description

The main idea of this design proposal is to avoid any moving parts outside the vacuum chamber.

The proposed solution to drive the forks, uses a permanent magnet rotor placed into a vacuum chamber coupled to a stator though a wall of low magnetic permeability stainless steel. By this way the use of bellows is avoided.

The rotor is fitted on a shaft supported by roller bearings. Materials and solid lubricants for the roller bearings have to be selected for low outgassing and friction requirement coming from the vacuum environment. Attached to the shaft there is a fork on which the wire is stretched in between. A position transducer, mounted on the rotating shaft, shall provide the absolute angular position for the feedback control loop of the motor and to determine the wire position accurately.

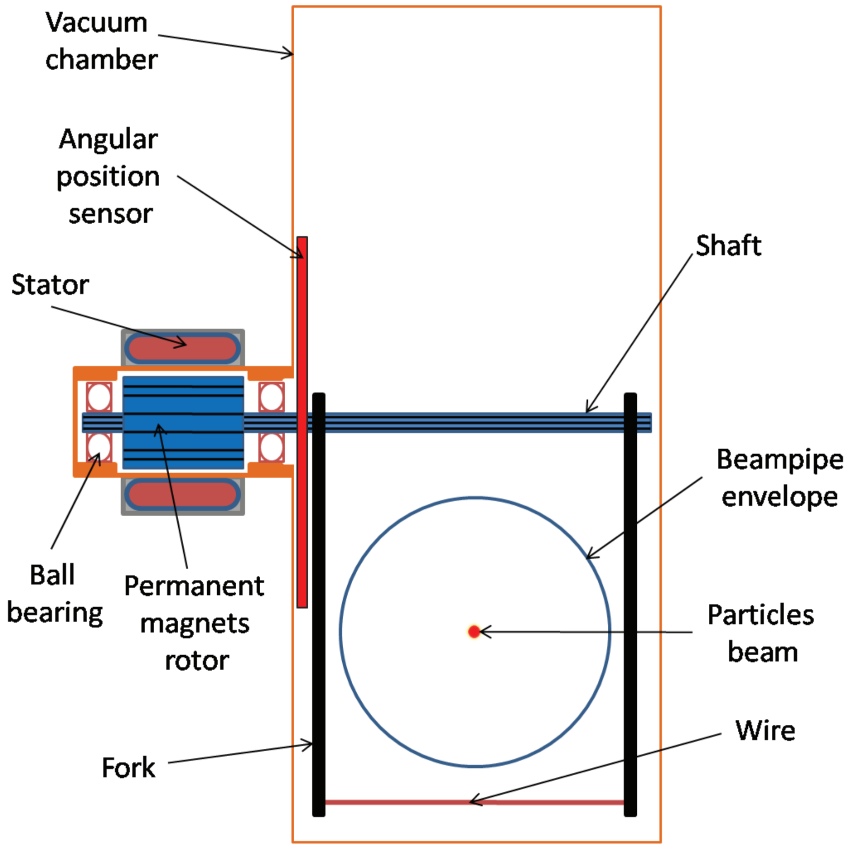

Figure 2.20: Simplified drawing of the future wire scanner. The orange lines show the vacuum barrier.

2.7.2 Advantages

This new conceptual design presents several avantages compared to classic designs described in 2.5.2 which can be listed as

- No bellow aging.
- Less friction i.e. less power needed to drive the fork.
- Direct drive i.e. no mechanisms which would introduce uncertainties in the fork position determination
- Less vibration.

It is expected that the accuracy of the system could be increased significantly to the specified value of 3.5 μm by taken these measures.

2.7.3 Challenges

Specifications (high accuracy, high acceleration), high environmental constraints and new design configuration imply high challenges which can be listed as

- Introduce a vacuum barrier in the motor airgap allowing a perfect tightness. It must be strong enough to avoid deformation due to vacuum pressure. The motor must reach very high acceleration.

- The permanenent magnets rotor must be vacuum compatible and must resist to radiation and bake-out temperature.

- The angular position sensor will be placed inside the vacuum chamber. It must be vacuum compatible and must resist to radiation and bake-out temperature. Morever, it must perform a very accurate measurment of the position.

- Wire scanners will be mounted in Electromagnetic Interference (EMI) sensitive environment. A special care must be take during the power supply design and the acquisition system.

- Vibration phenomenon.

- The disparities of physical parameters of the motor, power supply and long cables imply a high challenging control.

3

Sizing of the motor and its power supply

This chapter presents the design of the actuator for the fast and high accuracy Wire Scanner system. Such actuator consists of a Permanent Magnet Synchronous Motor (PMSM) with the permanent magnet rotor installed inside the vacuum chamber and the stator installed outside. Fork, permanent magnet rotor and two angular position sensors are mounted on the same axis and located inside the beam vacuum chamber. The system has to resist a bake-out temperature of 200^oC *and an ionizing radiation up to tenths of kGy/years. The requirements imply a maximum angular speed of* $210\ rad \cdot s^{-1}$, *an acceleration of* $40\ 000\ rad \cdot s^{-2}$ *and an angular position measurement accuracy of* $5\ arcseconds$. *The system must deal with extremely low vibrations and low electromagnetic interferences. To enable the chosen PMSM to resist these constraints, some material and mechanical modifications have been made on its rotor. So, after exposing the main characteristics of the new structure of the PMSM including all the changes operated on it, the power supply based on a 3-phase linear inverter is sized for the motor feeding. The performances of the designed motor and its power supply are investigated through simulations using Matlab/Simulink software. The sizing process is finished by formulating the main recommendations on the thickness and the material of the vacuum barrier.*

3.1 Introduction

The constraints of the WS include the load and environmental ones. The load of the WS is comparable to one of a lightweight fork with a thin wire on its extremity. Because of the speed and acceleration to be reached by the wire, acting the WS system requires a high power regarding the load size. So, in addition to the electromechanical performances of the motor to be used, a high performance of the power supply and its control has to be fulfilled to perform the predefined WS angular target, as accurate as possible. The second difficulty in the sizing process concerns the hard environmental conditions of operation of the motor and its control unit. These constraints include the high temperature, the UHV and the high radiation level.

In the following sections, all the WS constraints are firstly presented in terms of acceleration, speed, position and mechanical torque of the motors shaft and its load. Then, on the basis of a comparison study of four different motor technologies, a solution is proposed. Going through the load and environmental constraints, the proposed Permanent Magnet Synchronous Motor (PMSM) is sized considering some significant modifications of its rotor part. This allows to design the adequate power supply which is a 3-phase linear inverter capable of ensuring the currents and the voltages across the motor during the WS operating cycle. An electromagnetic study is also carried out in order to correctly choose the thickness and the material of the vacuum barrier. Finally, the expected WS behaviours are validated through a simulation study of the whole system (motor, power supply and load).

3.2 Specification

In this section, specifiaction of the motor including its load, its drive requirement and the environmental constraints are defined.

3.2.1 Definition of the drive requirements and load

A scan consists in a π rad rotating movement including 3 phases: firstly, starting from a home position, the motor is accelerated with high torque to a constant angular speed, at which the interaction between the wire and beam occurs. Then, the motor is rapidly decelerated to a final home position (Fig. 3.1).

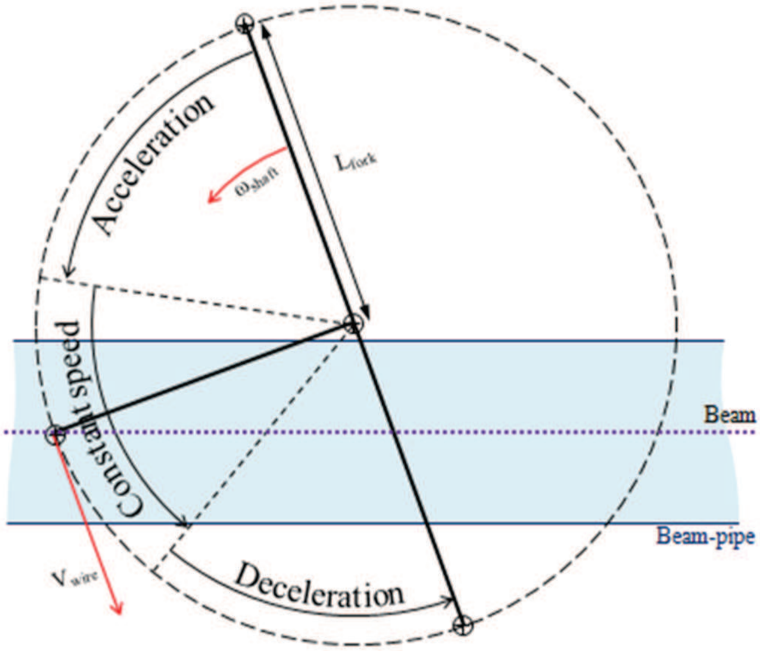

Figure 3.1: Scan movement.

As defined in the general specification, the requierment in terms of maximum speed of the wire during the scan is given by:

$$V_{max} = 20\ m.s^{-1} \tag{3.1}$$

Considering a fork lenght $L_{fork} = 100\ mm$, the maximum requiered angular speed is cumputed as following:

$$\omega_{r,max} = \frac{V_{max}}{L_{fork}} = 200\ rad.s^{-1} \tag{3.2}$$

In order to calculate a first estimation of the needed acceleration, we assume that the fork is driven as follows (Fig. 3.2, blue lines):

1. Constant acceleration from $0\ to\ \frac{\pi}{3}\ rad$

2. Constant speed from $\frac{\pi}{3}\ to\ \frac{2\pi}{3}\ rad$

3. Constant deceleration $\frac{2\pi}{3}\ to\ \pi\ rad$

In this configuration, the required maximum acceleration is given by

$$\alpha_{r,max} = 20\ 000\ rad.s^{-2} \tag{3.3}$$

This acceleration profile allows to reach the right speed. However, the brutal variation of acceleration implies jerk spikes which would generate vibrations in the system. These jerk spikes can be limited by reducing the slot of acceleration. In order to keep a margin of acceleration capability, we assume a maximum jerk limitation of 100% which implies twice higher peak acceleration (10) (Fig. 3.2, green lines).

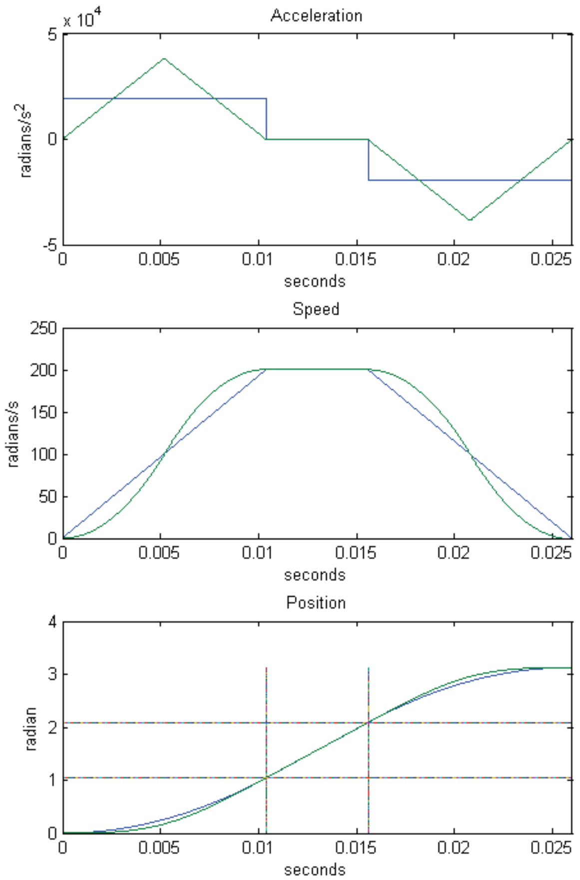

Figure 3.2: Blue lines: Angular acceleration, speed and position for a scan with no jerk limitation. Green lines: Angular acceleration, speed and position for a scan with 100 jerk limitation.

This acceleration can be calculated as follows:

$$\alpha_{r,jerk100\%} = 2.\alpha_{r,max} = 40\ 000\ rad.s^{-2} \tag{3.4}$$

Most of the time, the WS is used as an intermittent instrument. When a beam profile measurement is needed, CERN machine operators will ask for it. However, in certain cases, repetitive cycles can be asked to follow the evolution of the beam profile in time. These cycles can be defined through four steps as explained below

1. Scan IN, at a certain speed, ω_{IN}.
2. Delay 1 of a certain time value, T_1.
3. Scan OUT, at a certain speed, ω_{OUT}.
4. Delay 2 of a certain time value, T_2.

The worst-case cycle from an energy consumption point of view is given by the Table 3.1 (5).

Cycle parameters	Values
Scan IN angular speed, ω_{IN}	200 $rad.s^{-1}$
Time delay 1, T_1	10 ms
Scan OUT angular speed, ω_{OUT}	200 $rad.s^{-1}$
Time delay 2, T_2	1 s

Table 3.1: The worst-case cycle configuration from an energy consumption point of view (5)

The load can be defined as an inertial load. The total inertia is the sum of inertia values of shaft, angular sensor rotor, fork and rotor of motor (Fig. 3.3). The rotor inertia depends of the selected motor. The other estimation values of inertia are given in the Table 3.2. The friction torque is assumed to be negligible compared to accelerating and decelerating torque. Other resistive torque related to the Eddy current into the vacuum barrier depends of the selected motor and is discussed in Section 3.7.

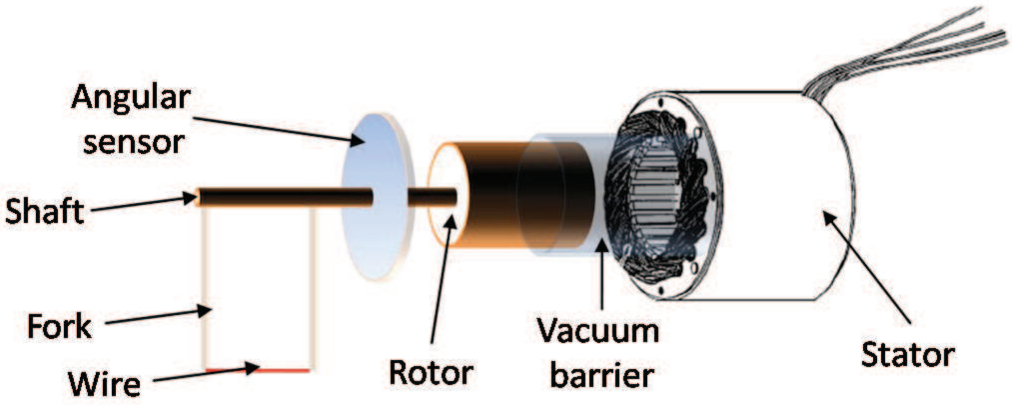

Figure 3.3: Diagram of the inertia sources.

Inertia of	Values
Shaft	$0.7.10^{-4}\ kg.m^2$
Fork	$1.1.10^{-4}\ kg.m^2$
Angular sensor rotor	$0.6.10^{-4}\ kg.m^2$

Table 3.2: Inertia values of the system

3.2.2 Definition of the mechanical constraints

First of all, the motor air-gap must be large enough to allow the introduction of a low magnetic permeability stainless steel wall of 0.3 mm (11). The moment of inertia of rotating parts (rotor, fork, shaft, angular sensors) also has to be minimised to reduce the requiered accelerating torque.

3.2.3 Definition of the environmental constraints

The rotor must be vacuum compatible i.e. not exceeding an outgassing rate of $10^{-9} Pa.m^3.s^{-1}$ after a bake-out phase. Therefore, the use of any glue or insulating material is not possible. The rotor must withstand a bake-out temperature of 200^oC and the whole motor must withstand an ionizing radiation of 1kG/year.

3.3 Types of motor selection

Four kinds of motor have been studied and compared to each other to make the best choice. These motors are:

- Permanent Magnet Synchronous Motor (PMSM)
- Induction Motor (IM)
- Switched Reluctance Motors (SRM)
- Permanent Magnet Assisted Reluctance Motor (PMASynRM)

The study allowed to highlight the advantages and drawbacks based on the following criteria demanded by the WS:

- Air-gap thickness
- Torque to inertia ratio
- Vacuum compatibility
- Radiation tolerance
- Temperature tolerance
- Torque ripple

3.3.1 Permanent Magnet Synchronous Motor (PMSM)

The PMSM is a 3-phase motor with permanent magnets on the rotor. By using appropriate sequence to supply the stator phases, a rotating field in the stator is created (Fig. 3.4). The rotor is attracted and rotates synchronously with the stator rotating magnetic field. The stator windings are distributed in the stator slots, so that the voltage induced by the magnet during rotor rotation (Back-EMF) is almost sinusoidal. This differentiates the PMSM from the commonly called Brushless DC Motor (BLDC), in which the back-EMF is trapezoidal (12).

The power density of a PMSM is higher than in other motors with the same rating due to a high magnetic field stored in the permanent magnets (13), (12). It is more

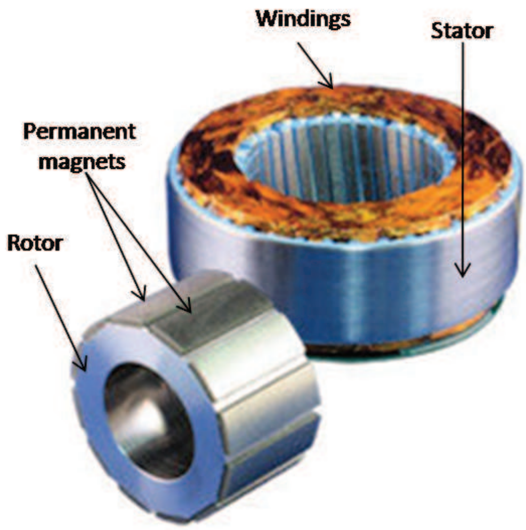

Figure 3.4: Picture of a frameless Permanent Magnet Synchronous Motor.

powerful and has a lower mass and a lower moment of inertia. Due to its high power density and smaller size, the PMSM has evolved in recent years as the preferred solution for high dynamics speed and position control drives (12). Moreover, it presents an excellent controllability with the possibility to minimize torque ripple. From the fact that there is no transfer of energy from stator to rotor, there is no copper losses in the rotor i.e. no heating. Since the magnetizing is provided from the permanent magnets rotor, the motor can be built with a large air-gap without losing performance (13). Moreover, the PMSM has a good tolerance regarding radiation issues. However, there are possibilities of permanent magnet demagnetization at high temperature or if a high peak of current occurs. Also, the glues which could be used to fix the pemanent magnets on the rotor, are not vacuum compatible.

3.3.2 Induction Motor (IM)

Fig. 3.5 shows a 3D view of a 3-phase induction motor having three windings on its stator and rotor (14). The 3-phase rotor windings are short-circuited. Only the stator is connected to the power supply and when its windings are fed with symmetric sinusoidal voltages, the resulting currents create a rotating magnetic field in the air-gap which induces electromotive forces in the closed rotor circuit. Unlike the PMSM, the rotor speed of IM is different from the stator field pulsation.

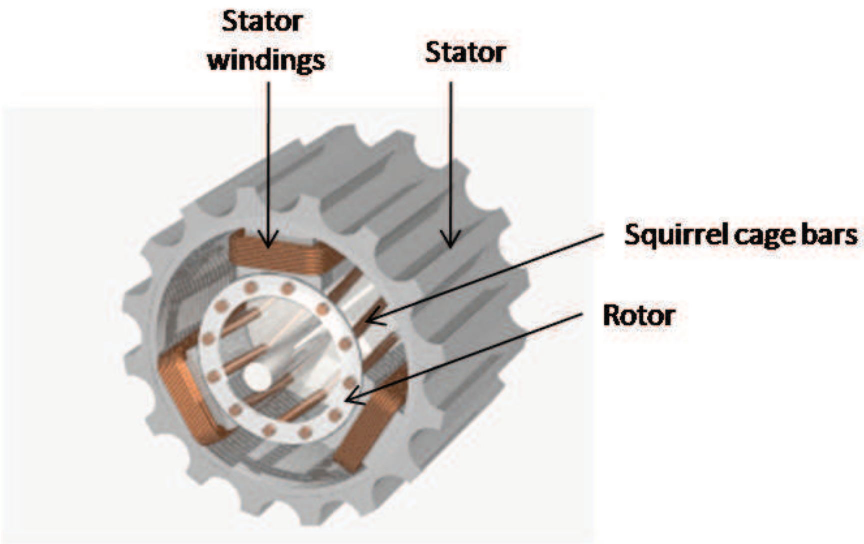

Figure 3.5: 3D view of an induction motor.

IM has no permanent magnets on the rotor. Because of its poor power factor and low efficiency, its average torque is largely lower than the PMSM torques, with the same ratings. This limits its use for strong acceleration application (14). Moreover, high thermal losses in the rotor would heat the vacuum chamber and without a cooling system, it would be difficult to cool down. In terms of air-gap thickness, the IM offers no space to insert the vacuum barrier. Otherwise, the IM has a good tolerance regarding radiation and temperature issues.

3.3.3 Switched Reluctance Motors (SRM)

The Switched Reluctance Motor (SRM) is usually used for positioning operation particularly with high speed/ low load positioning. It contains n_c different coils on the stator and a ferromagnetic slotted rotor with no permanent magnets nor windings (Fig. 3.6).

The working principle is based on the difference in magnetic reluctance of magnetic field lines between aligned and unaligned rotor position. When a stator coil is excited, the rotor experiences a force which pulls the rotor to the aligned position (15) (16). The number of poles on the SRM's stator is usually unequal to the number of the rotor poles in order to avoid the possibility for the rotor to be in a state where it cannot produce initial torque. It is the case when all the rotor poles are aligned with the stator poles.

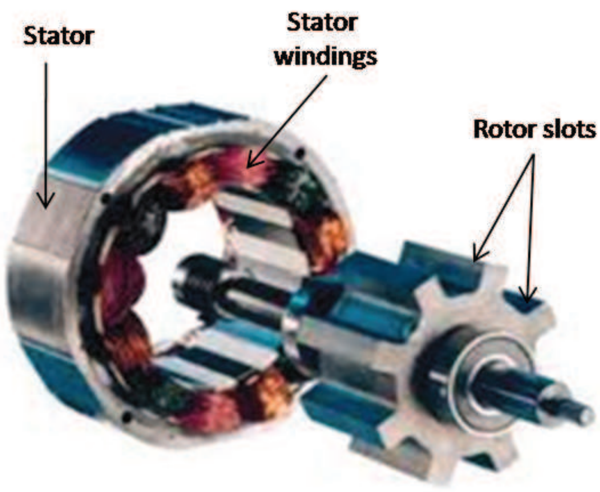

Figure 3.6: Picture of rotor and stator of a Switched Reluctance Motors.

With no permanent magnets and no windings in the rotor side, the SRM is a very good candidate for operations in high temperatures or in intense temperature variations. The rotor can easily be made as a vacuum compatible solid piece. Moreover, there is no transfer of energy between the stator and the rotor, unlike the induction motors, i.e. no thermal losses in the rotor which would be difficult to dissipate into the vacuum chamber. The SRM position control also is easier than the two previous machines (PMSM and IM).

However, there are some critical disadvantages, like high torque ripple due to switch operation and geometric structure including doubly salient motor, or an excessive bus current ripple generating electromagnetic interference (EMI) problems. Moreover, a low air-gap is required making more difficult the introducing of the vacuum barrier (17).

3.3.4 Permanent Magnet Assisted Synchronous Reluctance Motor (PMASynRM)

The Permanent Magnet Assisted Synchronous Reluctance Motor (PMASynRM) is a median solution between a permanent magnet synchronous motor and a switched reluctance motor (Fig. 3.7). The PMASynRM is obtained by replacing the rotor of a conventional AC machine by a rotor of SRM in which permanent magnets are inserted in order to have different inductances along its direct and quadrature axis (Ld and Lq) to develop a reluctance torque (18). The rotor can have various kinds of construction, but there is no excitation, unlike the IM, avoiding rotor copper losses.

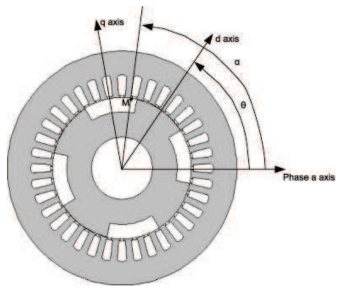

Figure 3.7: Cross-section of a cut-outs rotor PMASynRM.

The PMASynRM is superior to a switched reluctance motor because of low torque ripple. Moreover, since in the SynRM the permanent magnets are inserted inside the rotor, this motor is appropriate to vacuum.

However, the PMASynRM is generally not considered to be competitive in terms of power density and power factor whereas its efficiency and power density can be, in certain cases, comparable to induction machines (19), (20), (21).

3.3.5 Comparison and choice

To compare and choose the best motor technology a pentagon diagram has been used. Each apex traduces the degrees of suitability based on 6 criteria expressing the principal constaints of the WS application:

- Air-gap thickness
- Torque to inertia ratio
- Radiation tolerance
- Vacuum compatibility
- Temperature tolerance
- Torque ripple

A mark between 1 and 4 has been adopted to classify the motor's performances, as bellow :

- **Mark 1:** Hardly suitable.
- **Mark 2:** Possibly suitable.
- **Mark 3:** Suitable.
- **Mark 4:** Perfectly suitable.

On this basis, four pentagons have been obtained (Fig. 3.8).

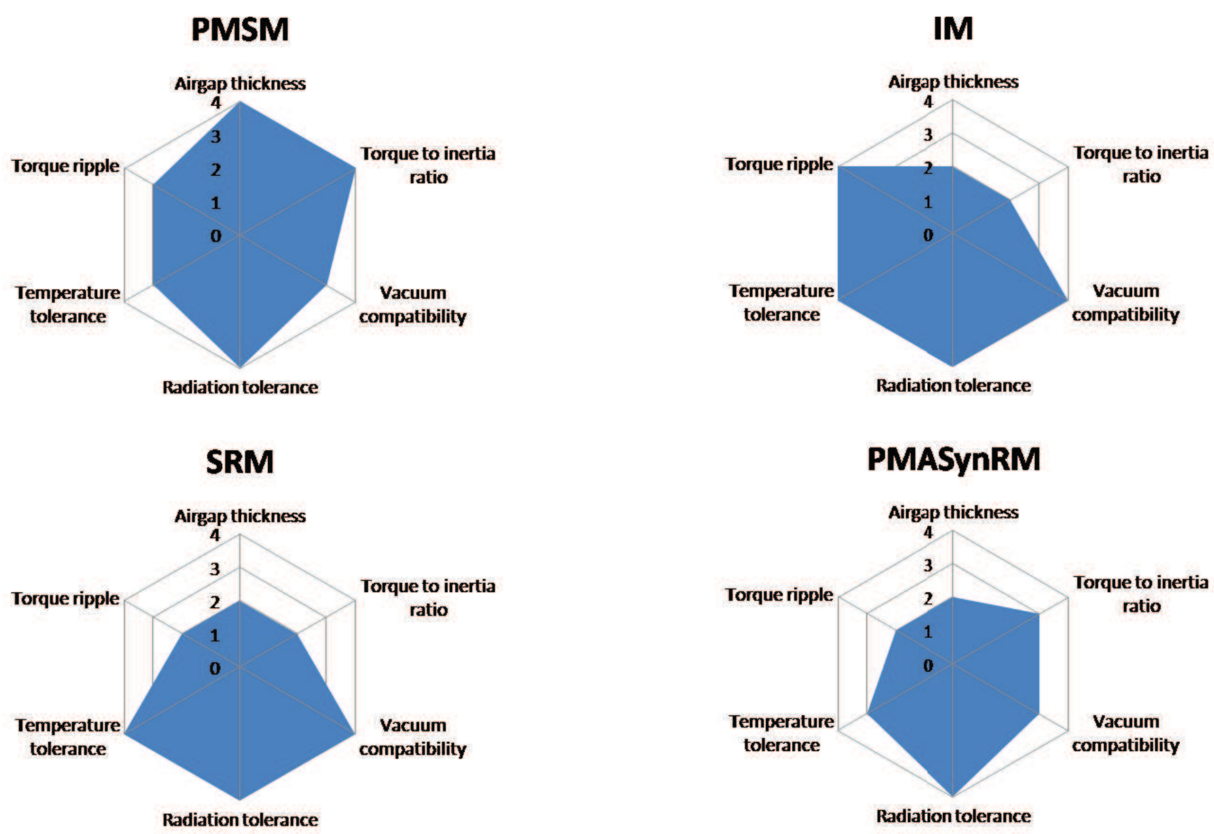

Figure 3.8: Comparison of different types of motor based on the criteria demanded by the WS actuator design. It is clearly shown that the PMSM is the most suitable.

From Fig. 3.8, it is possible to evaluate qualitatively which motor is most appropriate to our application regarding the comparison criteria. The most appropriate motor for our application is the PMSM for several reasons. The PMSM presents higher torque to inertia ratio than the other motors allowing high acceleration and deceleration rates. Unlike the IM and SRM, since the magnetizing is provided from the permanent magnets of the rotor instead of the stator, the motor can be built with a larger air-gap. This makes easier the introduction of a vacuum barrier in the air-gap. Moreover, it is superior than the IM by the fact that it has no thermal losses in the rotor and induces less torque ripple than the SRM does. However, a special care must be taken to make the rotor vacuum compatible and to prevent the permanent magnets from demagnetizing due to bake-out temperature.

3.4 Permanent Magnet Synchronous Motor configuration

In this section, the material and the configuration of the rotor and stator are discussed.

3.4.1 Discussion of stator materials

The stator being outside of the vacuum chamber, it does not need to be vacuum compatible. Then, as it can be dismounted during the backing phase, it is not concerned by the temperature issues. In theory, ionizing radiations damage the motor coils, in particular insulators material. However, a dose of 20 kGy is very low with damage levels (9). So, any standard stator should be suitable for this application.

3.4.2 Discussion of rotor structure and materials

In this part, we discuss the different structures and materials of the rotor before concluding by the most suitable configuration regarding our requirements.

The PMSM rotor consists of a iron core that may be solid or made of punched laminations on which the permanent magnets are fixed inside or outside. Punched laminations allow to reduce the Eddy current and to limit iron losses (13), (12). However, this configuration requires to fix isolated iron layers together and would make difficult the vacuum bake-out. For these reasons, we prefer using a solid core rotor than lamination core rotor.

There are mainly 3 types of PMSM rotor construction regarding the way the magnets are mounted on the rotor (13). Depending on the configuration, different properties of the motor can be obtained:

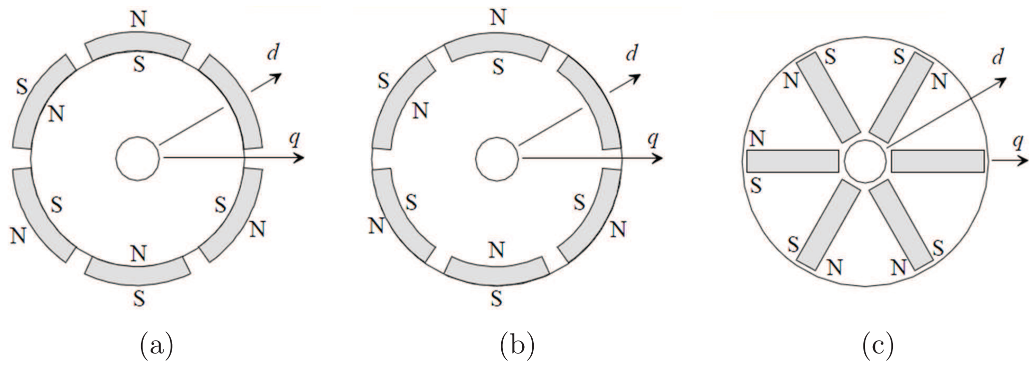

Figure 3.9: Different positions of the magnets on the rotor, PMSMs can be broadly classified into three categories:(a) Surface-mounted magnets (b) Inset-mounted magnets (c) Interior-mounted magnets.

On surface-mounted rotor (Fig. 3.9 , a), the permanent magnets are fixed to the cylindrical rotor outer surface using adhesives, and magnetized in the radiation direction. This construction makes the rotor easy to build and radially magnetized circumferential segments produce a smoother air-gap flux density and less torque ripples. Another reason that makes the surface magnet construction favorable for our application is the lower inertia due to the fact that the additional iron can be removed from the rotor to provide a lower inertia. As the rotor iron is approximately round and the stator inductance is low and independent of the rotor position, the control of the motor becomes simplier, as no account has to be taken for the reluctance effects.

On inset-mounted rotor (Fig. 3.9 , b), the magnets have better mechanical characteristics than on the surface-mounted rotor, but on the other hand, there is higher leakages between two adjacent magnets. In addition to the higher leakage, the torque production decreases more as the motor must operate at higher pole angle due to increased q-axis inductance compared to a non-salient rotor.

On interior-mounted rotor (Fig. 3.9 , c), each permanent magnet is mounted inside the rotor. In this case, the synchronous inductances vary as a function of rotor angle and the reluctance torque can be produced in addition to the excitation torque. Moreover, unlike the surface-mounted, it is a good candidate for high-speed operation. However, the variation of reluctance coming from the anisotropy of the rotor contributes to the production of torque ripples.

Finally, the preferred configuration is the surface-mounted rotor for its lower inertia, its simplicity of mounting, its low torque ripple and its control easiness.

After the selection of the rotor configuration, the next step is the selection of the most suitable magnets material. There are mainly four types of magnet materials used in PMSM application: Neodym-Iron-Bor (NdFeB), Samarium-Cobalt (SmCo), Aluminium-Nickel-Cobalt (AlNiCo) and Ferrite. The typical BH characteristics at room temperature of the materials in their sintered grades are shown in Fig. 3.10 (18).

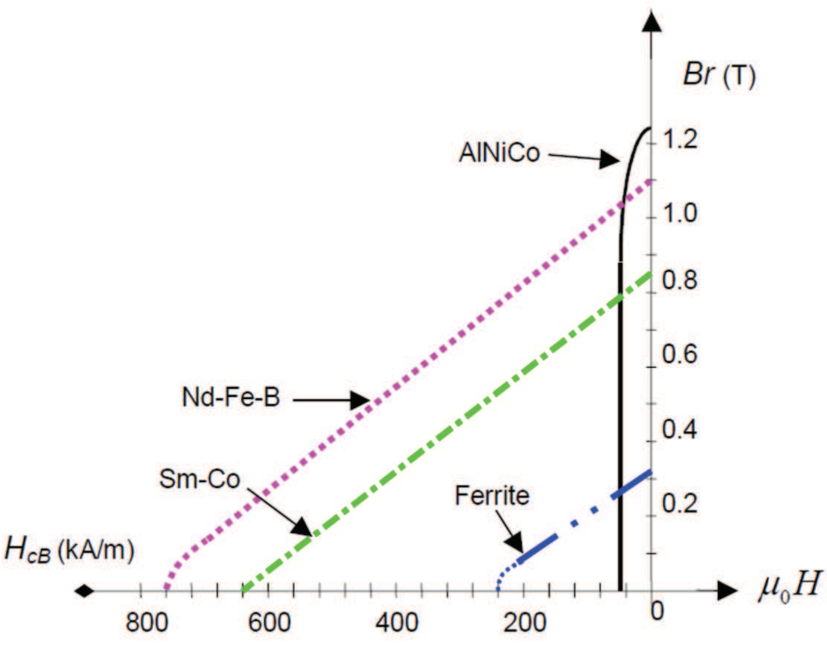

Figure 3.10: Demagnetizing curve of main magnet materials.

There is a number of different grades of each of these magnet materials, depending on their composition and manufacturing method. For servo motor application i.e. high dynamic performance, the choice stands between the high energy materials NdFeB and SmCo. NdFeB-magnets are generally cheaper than SmCo-magnets and have higher remanence at room temperature. However, NdFeB have a larger temperature dependency in both remanence and coercitivity, while SmCo is extremely resistant to demagnetization and presents a good temperature stability. It can be used around

250^oC without loosing the remanent flux density and its Curie temperature is from 700 to 800^oC (Fig. 3.11) (3).

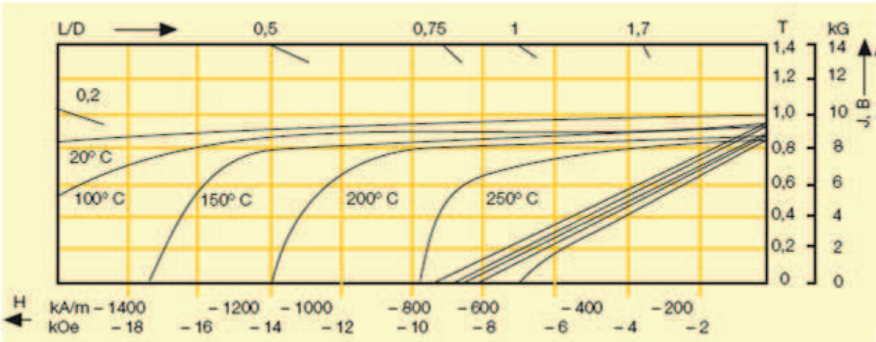

Figure 3.11: Temperature behaviours of the demagnetization curve of $SmCo_5$ (3).

Normally, permanent magnets are not used inside a UHV chamber, because they all show a considerably high outgassing rate. However, since the performance of insertion devices increases, some applications place the magnets inside the vacuum and is often accompanied by installation of a high pumping speed to evacuate the outgassing (9). Moreover, SmCo-magnets can be baked and are less sensitive to radiation damages.

The finally chosen configuration consists of a solid core rotor on which $SmCo_5$ magnets are mounted on the surface.

3.5 Motor sizing

In this section, a PMSM sizing model is presented before discussing the process used to select the appropriate motor. Then, the selected motor is described in details.

3.5.1 Sizing model

In this section, a simple classical model (22) of PMSM is presented in order to define the parameters characterizing the chosen motor and also to size its power supply. Assuming that the chosen surface mounted permanent magnets machine is a smooth pole machine which operates in the linear zone of its ferromagnetic material, the electrical part of this PMSM can be modeled by the equivalent single phase circuit shown on Fig. 3.12, a. For the sinusoidal steady state regime, the voltage equation in complex notations can be given by the equation 3.5. So, the vector diagrams of the corresponding voltage and magnetic flux can be represented on Fig. 3.12, b. All the electromagnetic parameters of the machine used in this report are represented on these two figures.

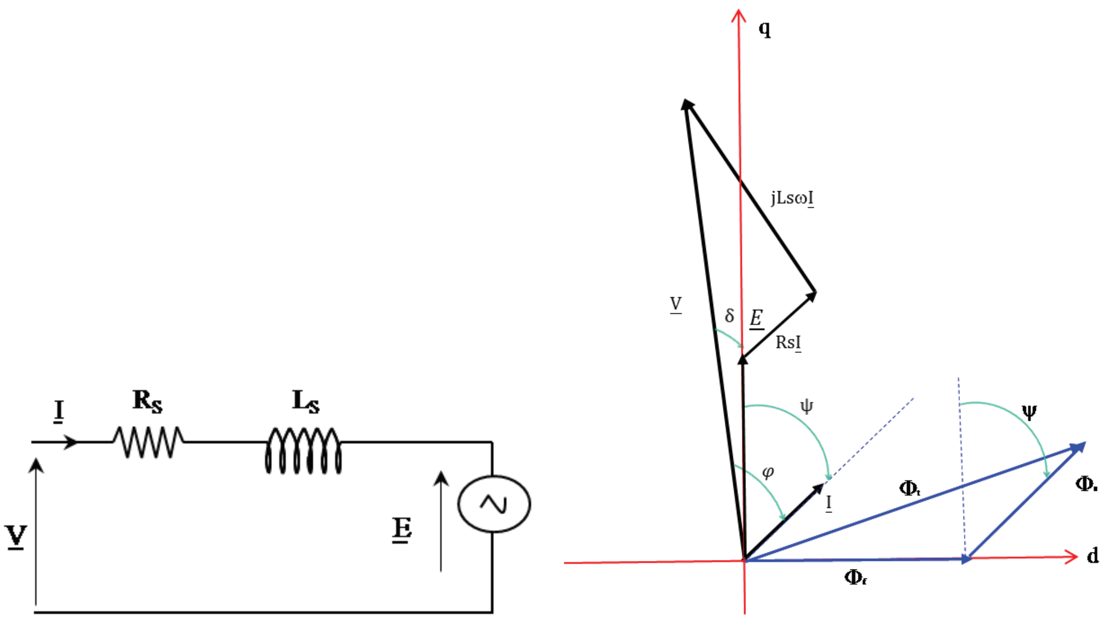

Figure 3.12: (a) Single phase equivalent scheme of the studied PMSM ; (b) Voltage and flux vector diagrams.

$$\underline{V} = \underline{E} + R_s\underline{I} + jL_s\omega\underline{I} \tag{3.5}$$

The electromagnetic torque in steady state can be expressed by the equation 3.6

$$T = p\sqrt{3}K_E I cos(\psi) = pK_T I cos(\psi) \tag{3.6}$$

Where, $\underline{V}$, $\underline{E}$ and $\underline{I}$ are the RMS values of respectively one phase stator voltage, one phase back-EMF and stator current; R_s and L_s are respectively the resistor and synchronous inductor of one phase of the machine; K_E and K_T are respectively the voltage and the torque constants with $K_T = \sqrt{3}K_E$ and p is the number of poles pairs number of the PMSM.

The resulting flux of the PMSM can also be computed in complex notations through the equation 3.7.

$$\underline{\phi_t} = \underline{\phi_f} + \underline{\phi_s} \tag{3.7}$$

With, $\underline{\phi_f}$ and $\underline{\phi_s}$ are the complex notations of fluxes under each pole of the stator windings and produced respectively by the permanent magnets and the stator currents. These two magnetic fluxes are related to the electrical magnitudes of the machine through the equations 3.8.

$$\begin{cases} E_{max} = pN\phi_f \\ \phi_s = L_s I \end{cases} \tag{3.8}$$

Where, E_{max} is the maximum of the back-EMF and N is the number of turns of one phase winding.

3.5.2 Motor selection process

Once the requirements have been established, the motor selection process can be performed according to the selection process presented on Fig. 3.13.

1. The angular speed limit of the motor must be higher than the required speed profile.

$$\omega_{m,limit} > \omega_{r,max} \tag{3.9}$$

2. The air-gap thickness must be larger than the vacuum barrier, to enable the introduction of the latter in the air-gap.

$$AG_{thickness} > VB_{thickness} \tag{3.10}$$

3. Each motor has its individual rotor inertia, which contributes to the system load torque (Torque = Inertia x Acceleration), so that the calculation of the system torques must be repeated for each considered motor.

4. The motor peak torque must be higher than the required maximum torque

$$T_{m,peak} > T_{r,max} \tag{3.11}$$

The required maximum torque can be calculated as follows:

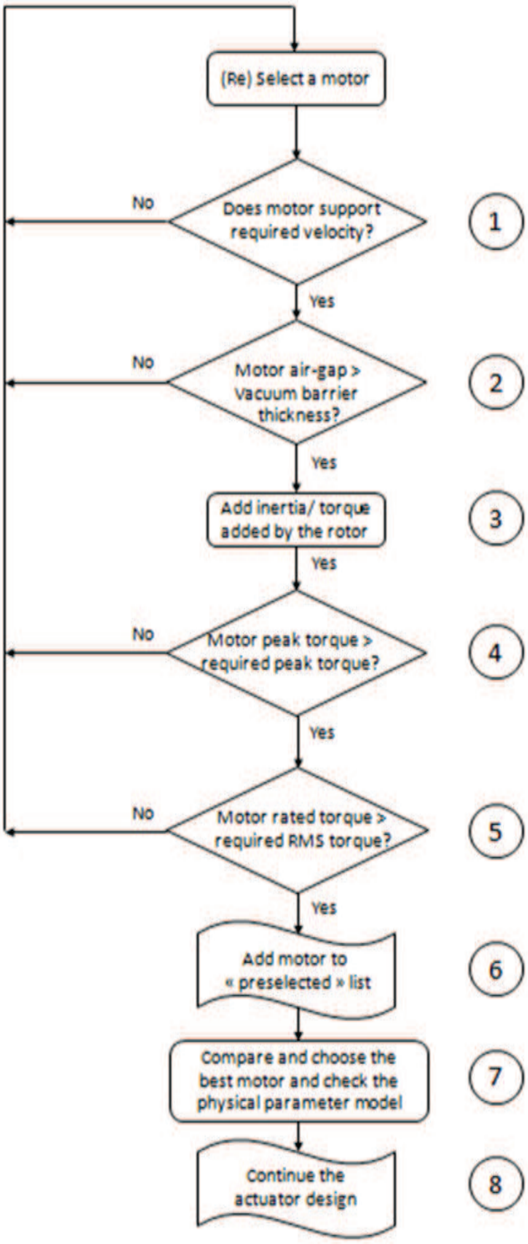

Figure 3.13: Motor selection process.

$$T_{r,max} = T_{acc} + T_{add} \tag{3.12}$$

with T_{acc}, the accelerating torque and T_{add}, the additional torque T_{add} which is dependant on the geometry, resistivity of the vacuum barrier, flux in the air-gap, friction and angular speed of the rotor. We assume that additional torque is negligible compared to accelerating torque

Accelerating torque T_{acc} is given by Newton's law:

$$T_{acc} = J_{total}.\alpha_{req} \tag{3.13}$$

where J_{total} is the total moment of inertia of shaft, fork, angular sensor and rotor and α_{req} is the required angular acceleration.

5. In order to avoid overheating, the continuous torque rating of the motor must be higher than the RMS torque.To calculate the RMS torque we suppose that the thermal time constant is largely greater than the worst-case cycle and that additionnal torques are neglected compared to accelerating and decelerating torque. The decelerating torque T_{dec} is assumed equal to accelerating torque T_{acc}.Thus, the help of the additional torque during the breaking is neglected. The RMS torque T_{rms} can be calculated as

$$T_{rms} \approx \sqrt{\frac{2.T_{acc}^2.t_{acc}}{t_{cycle}}} \tag{3.14}$$

with respectively $\mathrm{t_{acc}}$ is the acceleration time, $\mathrm{t_{cycle}}$ is the time of a cycle.

6. If all previous conditions are fulfilled, the motor is assumed to be able to drive the WS shaft and it is added in the list of selected motors.

7. By comparing the performances of the retained PMSM's list, the best solution is selected and identified starting from the manufacturer datasheet. The identification process consists in computing the physical parameters of the sizing model i.e. R_s, L_s, K_E, K_T, p and J_{total}.

8. After choosing the motor technology and doing the preliminary sizing, the next step consists in making the mechanical and material adjustments to have the most suitable motor possible to the environment constraints of the WS on the one hand and, on the other hand, in designing the motor power supply.

3.5.3 Presentation of the selected motor

Finally, selection process allowed to select the most appropriate motor which is the Parker K500150 frameless PMSM (Appendix 8.1). These types of motor are supplied in two independent parts: a 3-phase stator and a rotor with permanent magnets mounted on the surface. The kit motor approach allows a direct integration into the WS application. The rotor core is made of standard steel which is made vacuum compatible (23).

In this section, the geometrical parameters of the selected motor are presented before explaining how the rotor is modified in order to meet the WS requirements. Finally, the whole electrical, magnetic and mechanical rated characteristics of the machine are summarized.

3.5.3.1 Geometrical parameters

Starting from the manufacturer datasheet (24), the stator and rotor of the selected machine can be presented on Fig. 3.14. The most important geometrical dimensions are given directly on these figures.It is noticed that, the air-gap thickness between the rotor and the stator which is between 0.7 mm and 0.85 mm, is enough for vacuum barrier integration.

3.5.3.2 Rotor modification

The rotor core is made of standard steel which is vacuum compatible. Samarium cobalt has been chosen as adequate magnetic material for the rotor, instead of standard neodymium which withstands less well temperature. The standard glued mechanical fixation of the magnet on the rotor core has been replaced by an *ad hoc* designed mechanical fixation (Fig. 3.15, a) in order to match the vacuum requirements. Note that the used material has to be non-magnetic to not disturb the magnetic field circulation between the rotor and the stator which may deeply modify the initial performances of the motor. Thus, such mechanical fixation has been manufactured by using non-magnetic stainless steel (316LN) which has a relative permeability close to that of vacuum $\mu_r \simeq 1$.

Due to its low mechanical strength of samarium cobalt magnets and in order to avoid breaking them during the mounting, each pole magnet has been divided in 3 small parts of 17.71 $mm \times 12.69$ $mm \times 3.80$ mm (Fig. 3.15, b). These small magnets are magnetized

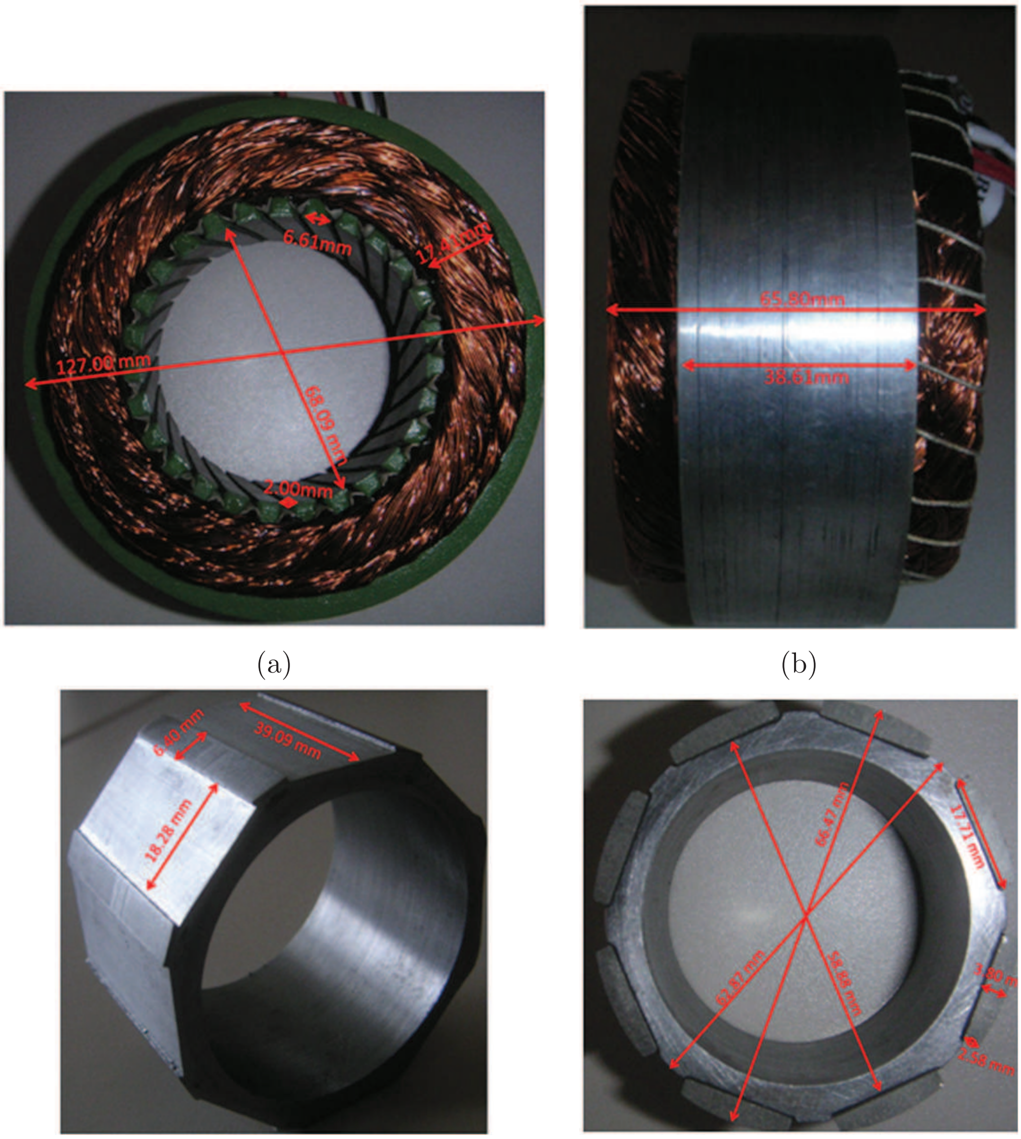

(a) (b)

(c) (d)

Figure 3.14: a) Transversal dimensions of the stator. b) Axial dimensions of the stator. c) Axial dimensions of the rotor. d) Transversal dimensions of the rotor.

in the radial direction before being positioned on the rotor surface in the manner shown in Fig. 3.15, c. Finally the designed mechanical fixation is used to secure definitively the permanent magnets on the rotor by opposing a pressure resistance (Fig. 3.15, d)(see Appendix 8.2 for calculation details).

For the choice of magnetic material of the rotor, the main constraint was the com-

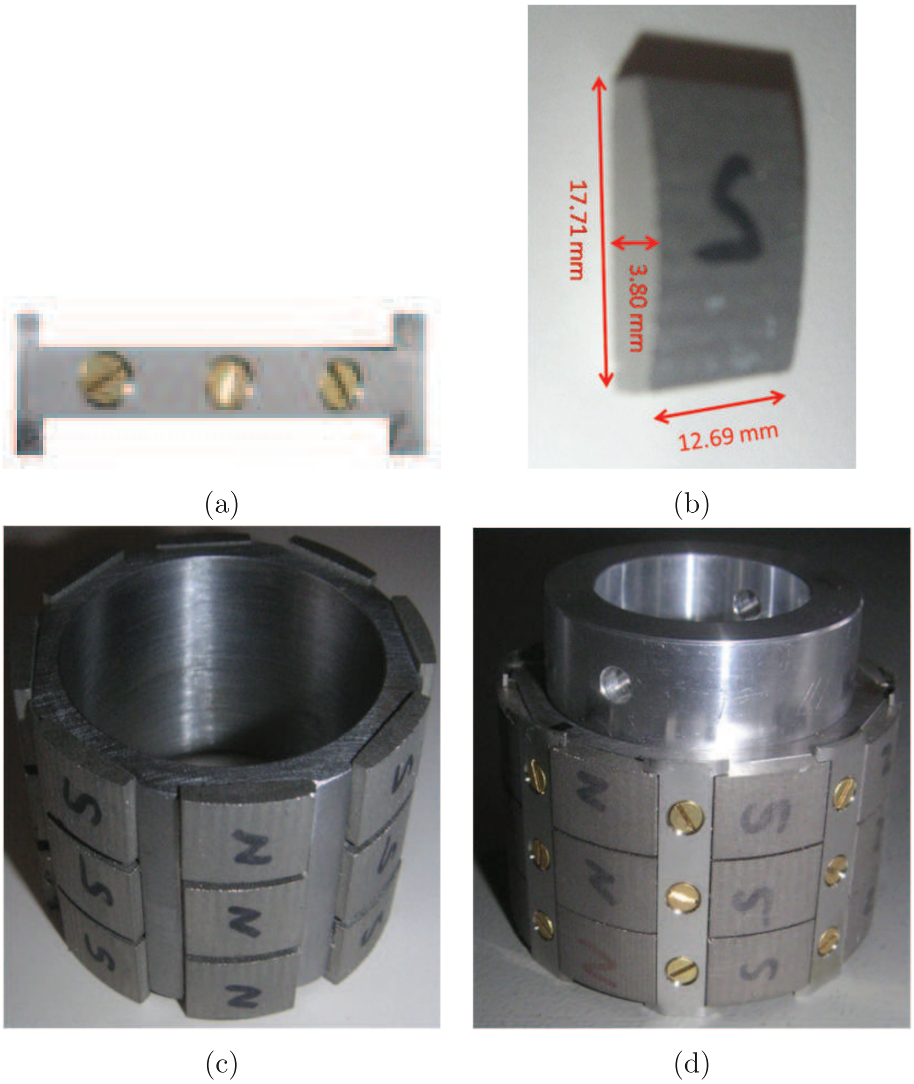

Figure 3.15: a) *Ad hoc* designed mechanical fixation. b) Magnets dimensioned specially to be easily integrated on rotor surface. c) Small magnets just positioned on the rotor. d) Whole rotor with all magnets mechanically fixed on it.

patibility with the vacuum environment. Indeed, the use of magnetic laminations was not possible due to the problem of outgassing of insulators between these elements. For this reason, a steel rotor was privileged (Fig. 3.14, c). Finally, in order to have a moment of inertia as low as possible, the shaft has been made using aluminium alloy (AW 6082).

3.5.3.3 Rated characteristics of the modified motor

Starting from the datasheet of the selected Parker frameless motor the rated characteristics of the proposed solution have been computed in Table 3.3 summarizes all these parameters.

PMSM parameters	Values	WS requirements	Values
Stator resistance R_s	0.245 Ω		
Stator inductance L_s	1.365 mH		
Voltage constant k_E	0.2598 $V.rad^{-1}.s^{-1}$		
Torque constant k_T	0.45 $N.m.A^{-1}$		
Pole pairs p	4		
Maximum frequency f	426 Hz		
DC bus voltage U_{dc}	300 V		
Nominal current I_N	18 A		
Peak current I_p	53 A		
Rotor inertia J_{total}	3.4×10^{-4} $kg.m^2$		
Max. mechanical speed Ω_m	670 $rad \cdot s^{-1}$	Max. angular speed	210 $rad \cdot s^{-1}$
Nominal mechanical speed Ω_N	355 $rad \cdot s^{-1}$		
Peak torque T_p	23.76 Nm	Max. troque	14.6 Nm
Nominal torque T_N	7.92 Nm	RMS torque	2.98 Nm
Maximum temperature	250^oC	Backout temp.	200^oC
Air-gap thickness e_0	0.8 mm	Vacuum barrier thick.	0.3 mm

Table 3.3: Selected motor parameters

3.6 Power supply definition and sizing

As the wire scanners will be mounted in a EMI sensitive environment, a special care has been taken to select the type of driver for the motor.

Power supplies based on the principle of Pulse Width Modulation (PWM) switching must be avoided because of effects of the high dV/dt. It would cause EMI effects in electrical networks which supply the PMSM, where often the measurments and power cables are close due to the space and installation constraints. This phenomenon would be amplified by the high cables length (up to 250 m).

A solution has been proposed inspired by the previous WS power supply design. It is based on 3-phase linear power supply, containing 3 power operational amplifiers used in non-inverting configuration.

The peak required current I_{peak} by the motor is given by:

$$I_{peak} = \frac{T_{max}}{k_T} \tag{3.15}$$

where k_T is the torque constant and T_{max} the maximum torque.

The maximum required voltage per motor phase V_{max} is the vector sum of maximum back-EMF E_{max} and the maximum voltage drop across the phase resistorR_s and inductor L_s when back-EMF is in phase with the current (assuming a perfect control of the current):

$$V_{max} = \sqrt{(R_s.I_{peak} + k_E.\omega_{max})^2 + (L_s.p.\omega_{max}.I_{peak})^2} \tag{3.16}$$

Where, ω_{max} is the maximum angular speed, p is the number of pairs of poles and k_E is the voltage constant.

Assuming that the back-EMFs are completely sinusoidal (no harmonics), the maximum required frequency is given by

$$f_{max} = \frac{p.\omega_{max}}{2\pi} \tag{3.17}$$

Starting from the specification above, the Apex PA52 power operational amplifier has been chosen. It can provide an output voltage of 200 V, a peak current of 80 Amps and a gain-bandwidth product of 3 MHz (25).

The required peak power during a wire scan (tens of ms) and the use of standard power plugs (230V, 10 Amps) imply to use capacitors based energy storage unit to balance the difference between the demanded power of the WS system and the supplied power of DC bus (Fig. 3.16).

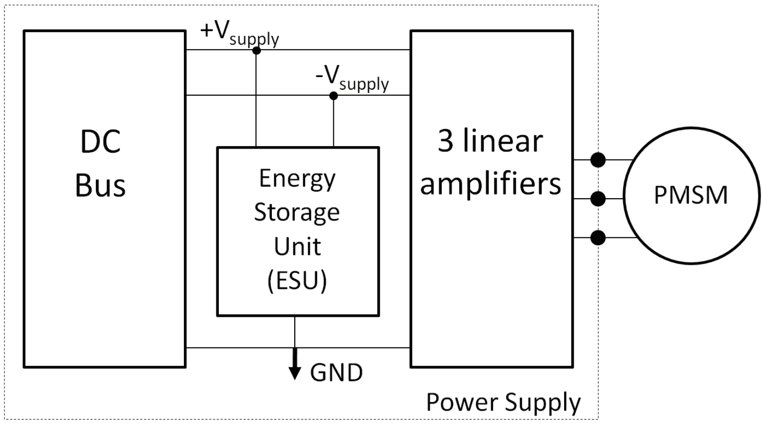

Figure 3.16: Schematic of the power supply including DC bus, energy storage unit and 3 linear amplifiers.

3.7 Recommendation on vacuum barrier sizing

Two kinds of criteria have to be considered for sizing the vacuum screen, the mechanical criteria and the electromagnetic criteria. In mechanical terms, ensuring a perfect insulation of the vacuum 3D space means that the vacuum barrier must support a low pressure of 10^{-8} Pa. From the electromagnetic point of view, it is necessary to choose a non-conductive material so that the generated power losses and the relative resistive torque can be neglected as assumed above. To do this, a quick model has been developed to evaluate the barrier power losses and their dependences on the material, the thickness and power supply frequency which is related to the motor speed and its number of pairs poles . In this section, a brief description of such model is exposed with some recommendations on the barrier material choosing.

The basis of this model consists in computing the Eddy current within the vacuum barrier when it is under the radial rotating magnetic field coming from the stator windings (Fig. 3.17).

Indeed, the symmetric 3-phase stator currents of the PMSM generate the rotation flux density $\overrightarrow{B}$ on which the rotor is fastened to rotate at synchronous speed. Located between the stator and the rotor, the vacuum screen is plunged in this flux density there through it in the radial direction.

$$\overrightarrow{B} = B_{max} sin(\omega t)\overrightarrow{e_r} \tag{3.18}$$

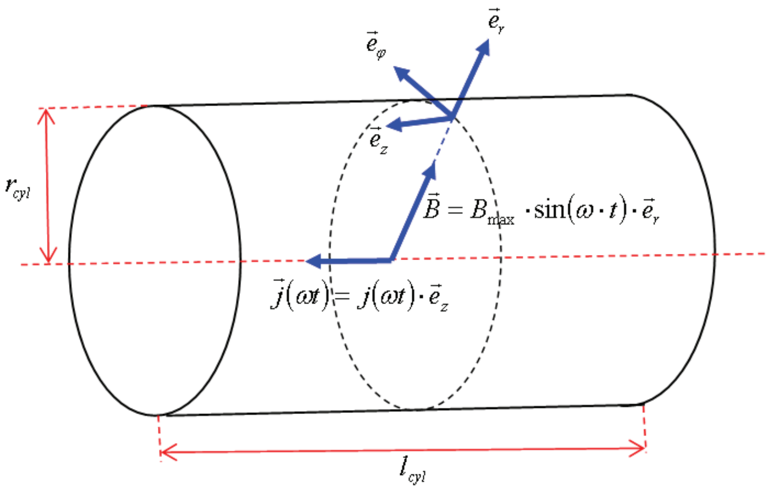

Figure 3.17: The vacuum barrier plunged in the radial flux density of the PMSM.

Assuming that there is no board effects in the PMSM and in the cylinder, the flux density $\overrightarrow{B}$, the cause of $\overrightarrow{j}$, are radial and invariant according to the 3D space coordinates (axial, azimuthal and radial coordinates: respectively, z, φ and r).

Consequently, one can conclude that $\overrightarrow{j}$ is independent on the 3D coordinates. On the basis of Lenzs law, specifying that the current density $\overrightarrow{j}$ induced by $\overrightarrow{B}$ produces a magnetic flux density which opposes the origin responsible of its creation so, this field is opposite but in the same direction of $\overrightarrow{B}$. In order to generate this radial flux density, the current density has to be in the axial direction.

Knowing the expression of the current density in the vacuum barrier the dissipated power by Joule effect can be easily evaluated. The Fig. 3.18 shows the variation of the power losses in a vacuum barrier of inox 360LN16 ($\mu_0 = 1.25663706{\cdot}10^{-6}\ m{\cdot}kg{\cdot}s^{-2}{\cdot}A^{-2}$;$\sigma = 1315789\ \Omega^{-1} \cdot m^{-1}$) in function of the power supply frequency. The used barrier dimensions are $r_{cyl}\ =\ 34.5\ mm$, $l_{cyl} = 75\ mm$ and a thickness of $0.25\ mm$. It can be seen that the losses at the maximum speed of the WS, which corresponds to $f = 130\ Hz$, are about $170\ W$. These power losses, introduce an additional resistive torque of $0.24\ Nm$. This value is negligible in comparison with the nominal and maximal torques of the motor, namely $7.92\ Nm$ and $23.76\ Nm$. Thus, it is recommended to use the inox 360LN16 to build the vacuum barrier with the dimensions given above and a thickness to set as little as possible.

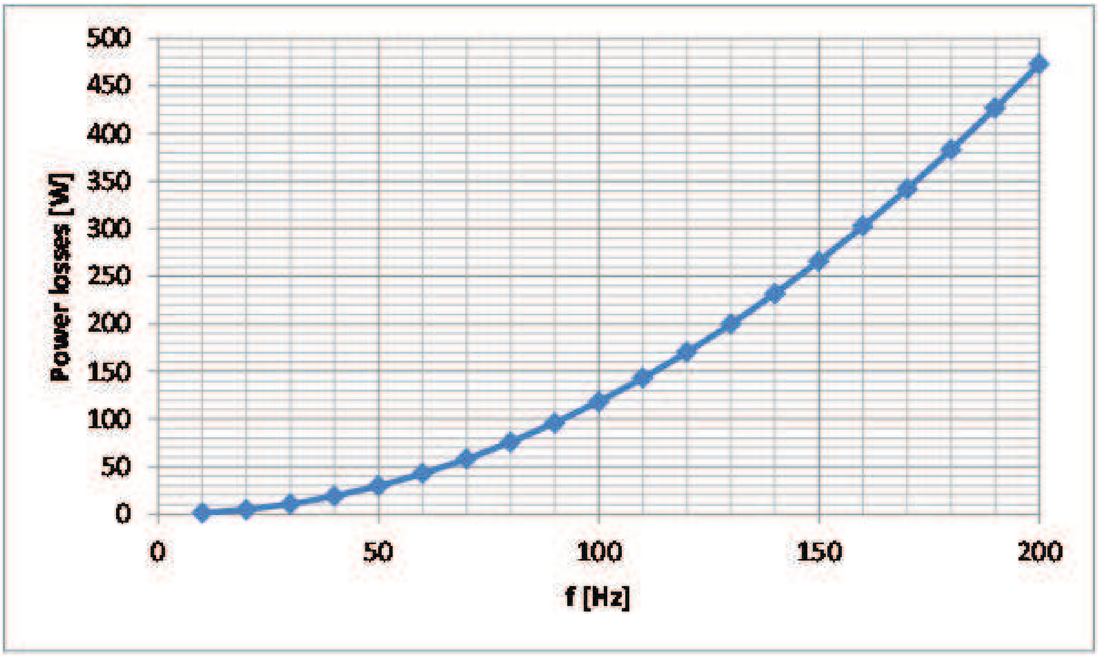

Figure 3.18: Variation of power losses in the vacuum barrier in function of power supply frequency.

3.8 Simulation validating study

In order to do a first test of validity of the chosen motor with regard to the wire scanner specification, a simulation study has been achieved starting from the manufacturer characteristics. The obtained results allowed to confirm that the motor reaches required performances. After the dynamic modelling of the motor with its vacuum barrier, a servo control has been carried out under Matlab/Simulink software. As the aim is to see the rated values of the position, speed, acceleration, deceleration, current and voltage of the PMSM, the linear amplifier and angular sensor have been modeled through simple gains.

3.8.1 Dynamic model of the motor with the vacuum barrier

Assuming that the 3-phase stator windings of the PMSM are balanced, the voltage equations of the 3-phase stator windings can be expressed as:

$$u_1(t) = L\frac{d}{dt}i_1(t) + R.i_1(t) + u_{i1}(t) \tag{3.19}$$

$$u_2(t) = L\frac{d}{dt}i_2(t) + R.i_2(t) + u_{i2}(t) \tag{3.20}$$

$$u_3(t) = L\frac{d}{dt}i_3(t) + R.i_3(t) + u_{i3}(t) \tag{3.21}$$

where u_1, u_2, u_3 and i_1, i_2, i_3 are respectively the 3-phase voltages and currents of the stator windings, R and L are their resistance and inductance, u_{i1}, u_{i2}, u_{i3} are the back-EMFs.

After Laplace transformation, the currents are given by following equations:

$$i_1(s) = \frac{1/R}{L/Rs + 1}(u_1(s) - u_{i1}(s)) \tag{3.22}$$

$$i_2(s) = \frac{1/R}{L/Rs + 1}(u_2(s) - u_{i2}(s)) \tag{3.23}$$

$$i_3(s) = \frac{1/R}{L/Rs + 1}(u_3(s) - u_{i3}(s)) \tag{3.24}$$

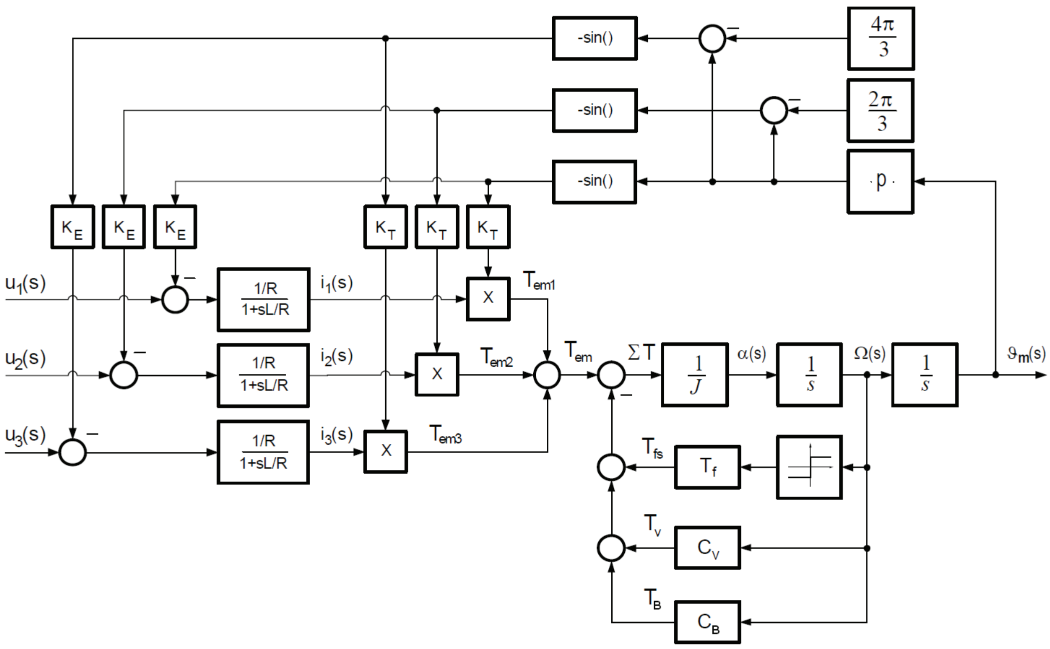

Figure 3.19: Model diagram of the motor including vacuum barrier effect.

The electronmagnetic troque is given by

$$T_{em}(\theta_m, t) = -K_T \left(sin\left(p\theta_m\right) i_1(t) + sin\left(p\theta_m - \frac{2\pi}{3}\right) i_2(t) + sin\left(p\theta_m - \frac{4\pi}{3}\right) i_3(t) \right) \tag{3.25}$$

where K_T is the torque constant and θ_m is the mechanical position of the rotor.

The output torque is given by

$$\sum T = T_{em} - T_{fs} - T_v - T_B \tag{3.26}$$

where T_{fs} is dry friction torque, T_v viscous friction torque and T_B resistive torque due to the Eddy current in the vacuum barrier.

Dry friction torque is given by

$$T_{fs} = sgn(v)T_s \tag{3.27}$$

where T_s is the dry friction torque value.

Viscous friction torque is given by

$$T_v = C_v\Omega \tag{3.28}$$

where C_v is the viscous friction coefficient.

The vacuum barrier impact is modeled by an additional load torque proportional to speed given by

$$T_B = C_B\Omega = 4 \times 10^{-3}\Omega \tag{3.29}$$

where C_B is the vacuum barrier effect coefficient.

Equations of the movement are given by

$$\alpha(t) = \frac{\sum T}{J} = \frac{T_{em} - T_{fs} - T_v - T_B}{J} \tag{3.30}$$

$$\Omega(t) = \int \alpha(t)dt + \Omega(0) \tag{3.31}$$

$$\theta_m(t) = \int \Omega(t)dt + \theta_m(t) \tag{3.32}$$

where $\alpha(t)$ is the angular acceleration, $\Omega(t)$ is the angular speed, $\theta_m(t)$ is the angular position and J the total inertia on the shaft.

By combining all these relations, we obtained the model diagram of the motor including vacuum barrier effect (Fig. 3.19).

3.8.2 Simulation results

PMSM parameters	Nominal values (unit)
Stator resistance R	0.245 (Ω)
Stator inductance L	1.365 (mH)
Voltage constant k_E	0.2598 ($V.rad^{-1}.s^{-1}$)
Torque constant k_T	0.45 ($N.m.A^{-1}$)
Pole pairs p	4
Total inertia J	$5.8.10^{-4}$ ($kg.m^2$)

Table 3.4: PMSM and amplifier parameters

Assuming sinusoidal voltage waveforms in function of the electric angle and by using two specific functions for the initial phase and magnitude of the sinus, the voltages waveforms of Fig. 3.20 have been used as the simulation input of the dynamic model explained above. Such waveforms were obtained with the help of the proposed vector control of the PMSM which is presented in details in Chapter 5 (26). By examining these waveforms, it can be noticed that the peak value of the voltage is about 80V which is widely less than what is supported by the motor and the DC-bus of its power supply, 300 V and 100 V respectively.

In Fig. 3.20, the corresponding 3-phase currents are shown. It can be noticed that the current peaks are located within the envelope ± 38 A, which is tolerated by the PMSM and the power supply supporting respectively ± 53 A and ± 80 A.

The Fig. 3.22 shows that the angular speed of the motor reaches its peak value of 210 $rad \cdot s^{-1}$ at the angular position of $\pi/3$ rad. A speed step to the same value is then provided on the interval $[\pi/3, 2\pi/3]$ and finally, deceleration interval $[2\pi/3, \pi]$ where it is seen a speed regular decrease until canceled at the angular position π rad. This speed/position target fulfills the specification of the wire scanner.

The resulting electromagnetic torque waveform presented on Fig. 3.23 shows that a maximum value of ± 14.8 Nm is reached and maintained during about 0.01 s. According

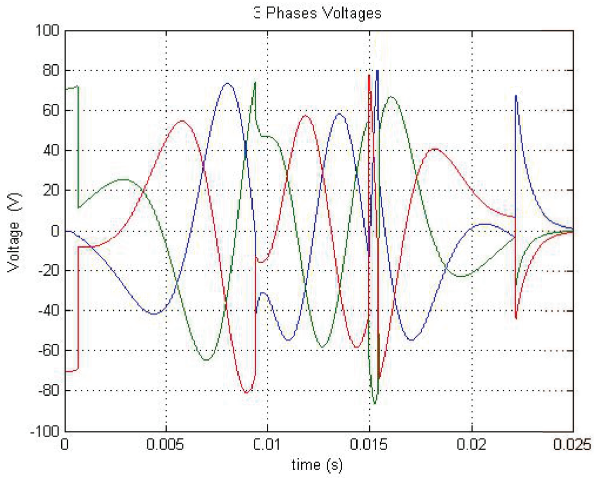

Figure 3.20: Simulated input 3-phase voltages supplying the PMSM.

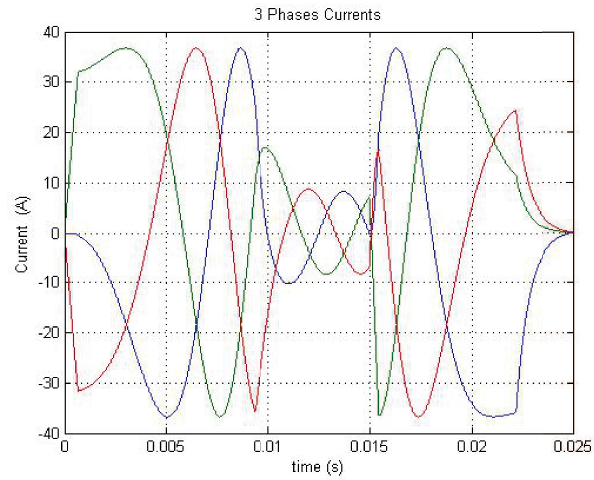

Figure 3.21: Absorbed 3-phase currents across the PMSM stator.

to the PMSM datasheet, this value is widely lower than what is supported by the motor, namely 23.76 Nm.

On the basis of the simulation results presented above, it can be concluded that the chosen PMSM as well as its power supply and the sized vacuum barrier are valid. Thus, the prototype of the fast wire scanner actuator can be built in order to test the functionalities of the WS experimentally. This can be done notably by developing a control algorithm more adequate than what is used in this section for sizing validation purpose.

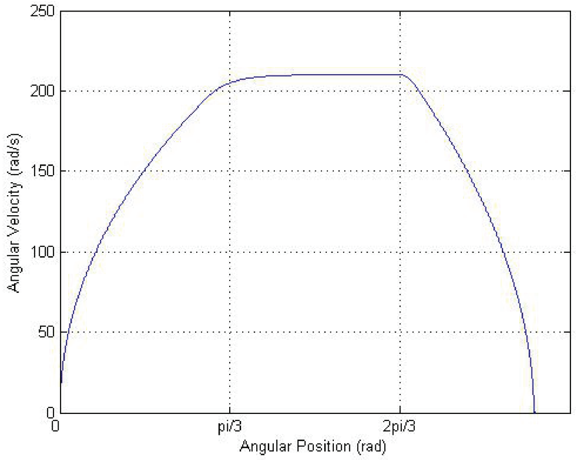

Figure 3.22: Simulated angular speed ($rad.s^{-1}$) versus angular position (rad).

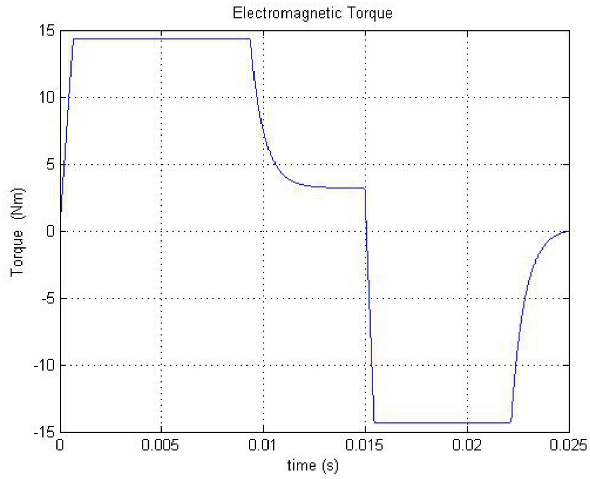

Figure 3.23: Simulated torque (Nm) versus time (sec).

3.9 Conclusion

The sizing process of the drive part of the WS actuator has been exposed in details. Both the mechanical and the environmental constraints of the WS have been combined to choose a specific technology of PMSM, called frameless Parker motors, in which the main parts of the machine were purchased separately. To fulfill the environment constraints of temperature and vacuum, the stator has been kept with its original characteristics while the rotor has been deeply modified before sizing the power supply device. The latter consists of a 3-phase inverter specifically designed for this application, using the linear amplifiers instead of the power switches classically used like IGBTs or MOSFETs. Indeed, the EMC constraints of the WS made impossible the use of power converters with PWM. Then a theoretical study on the Eddy current losses has been carried out to define some recommendations on the geometrical dimensions and the material of the vacuum barrier. Finally, on the basis of a dynamic model of the system PMSM-WS-vacuum barrier, a simulation program has been developed and executed to simulate a typical cycle of the WS device. The obtained results in terms of acceleration, deceleration, speed and position show that the sizing process has been made correctly.

4

Position measurement

This chapter is dedicated to the selection and the experimental test of the high accuracy angular position of the Wire Scanner actuator. The accuracy of this sensor has to be no less than 25 μrad r.m.s during the scanning part of the stroke. As for the motor, the position sensor has to resist a temperature of 200^oC, an ionizing radiation up to 20 kGy/years and must be UHV compatible (total outgassing not exceeding 10^{-9} $Pa \cdot m^3 \cdot s^{-1}$). The selection process has been performed through a comparative study of five position sensors. Following the same way as the motor selection in the previous chapter, these resolvers have been compared to each other according to five criteria (accuracy, vacuum compatibility, temperature tolerance, radiation tolerance and mechanical integration). Thus, the choice fell on the sensor which best meets these criteria, namely a solid rotor resolver (Rotasyn) and an optical fiber based rotary encoder which consists of a rotating disk, an optical fiber feedthroughs and a deported opto-electronics interface. In order to develop the optical fiber encoder, a flexible test setup was designed and tested. This encoder provides a resolution of 157 μRad with a track of 10 μm slits, and two position references using only one channel. An accuracy of ± 25 μRad is reached by angular calibration. Finally, the sensor offers EMI immunity, UHV compatibility and withstands radiation and temperatures up to 200^oC.

4.1 Acccuracy, resolution, and repeatability definition review

In this chapter, a definition of terms of accuracy, resolution and repeatability terms is needed and is given hereunder (27).

- Accuracy (Fig. 4.1) is the closeness of the agreement between the result of a measurement and the true value of the measurand.
- Repeatability (Fig. 4.1) is the closeness of the agreement between the results of successive measurements of the same measurand carried out under the same conditions (same measurement procedure, same measuring instrument). It can be seen as a repetition of the results over a short period of time.
- Resolution is the smallest increment of the measurand which can be discerned by the measurement device.

4.2 Specification

The angular position determination is needed with quite different specification for two purposes:

- The absolute position readout needed for the motor control, which implies an online measurement throughout the full stroke of about π *rad*.
- The position measurement related to the overall precision of the wire scanner system, as it is required to obtain an accurate trajectory of the wire when it crosses the particle beam.

The requirements for each of these functions are introduced hereafter.

4.2.1 Measurement for motor control

The absolute angular position for the motor control must be measured with an accuracy better than 6 *mrad* r.m.s. (20 *arcminutes r.m.s.*) (28).

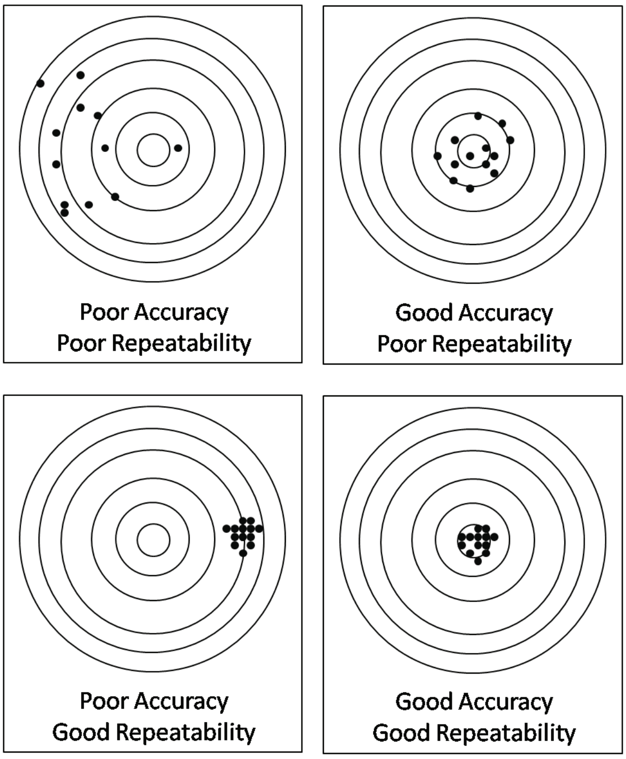

Figure 4.1: Accuracy versus repeatability.

4.2.2 Measurement for determination of the wire trajectory

The wire position determination requires an angle measurement every 500 μrad, corresponding to sampling frequency of 286 kHz, with an accuracy of 25 μrad r.m.s during the scanning part of the stroke. If the angular transducer could be calibrated, only a repeatability of 25 μrad is needed. The signal processing may be performed offline if the accurate timing of the data recording can be implemented. The parameters of the movement are as follows:

- Peak angular velocity up to 200 $rad.s^{-1}$
- Peak acceleration up to 40 000 $rad.s^{-2}$

4.2.3 Material and vacuum compatibility

The surface of the transducer exposed to vacuum shall have, after bake-out, a total outgassing not exceeding 10^{-9} $Pa.m^3.s^{-1}$. Outgassing of hydrocarbons shall not be measurable using the state of the art residual gas mass spectrometers. The most suitable materials are stainless steel, copper, aluminum and ceramics. Polyimide may be acceptable as a conductor insulator if its use does not compromise the total outgassing specification. The leak rate across any barriers between atmosphere and vacuum shall not exceeded 2.10^{-11} $Pa.m^3.s^{-1}$.

4.2.4 Temperature constraints

The transducer operates at room temperature; however, every exposure of the vacuum chamber to atmosphere require a subsequent vacuum conditioning comprising a thermal cycling at high temperature. All parts of the transducer installed in the vacuum chamber or in contact with it shall withstand thermal cycles at 200^oC during 24 hours. Up to 30 thermal cycles are foreseen over the equipment lifetime. The transducer is not expected to operate during the high temperature cycles.

4.2.5 Radiation constraints

All components should be installed nearby the point where the measurement is taken and must be resistant to a dose of 20 kGy (roughly 1kGy/year) cumulated ionizing radiation. Non radiation tolerant electronics must be installed in shielded galleries away from the particle beam, which implies cables up to 250 m long.

4.2.6 Assembly and integration requirement

The diameter of the sensor should not exceed 200 mm and 40 mm thickness . The total inertia of rotating parts shall be lower than $0.6x10^{-4}$ $kg.m^2$. The assembly procedure must follow the best applicable practices to ultra-high vacuum systems, in order to prevent leaks, virtual leaks and outgassing. The sensor construction must allow the chemical cleaning of all surfaces exposed to vacuum by immersion in a degreasing bath with ultrasonic agitation. If the sensor is analogue, the impact of the cables length(up to 250 m) shall be taken into account in the assessment of the overall accuracy.

4.3 Market survey

Commercially-available, non-contact, angular transducers are almost exclusively either optical encoders or resolvers.

The optical encoder (Fig. 4.2, a) consists of a beam of light, in front of a photodetector, which is periodically interrupted by a coded opaque/transparent pattern on a rotating intermediate disk mounted on a rotary shaft. There are two basic types of optical encoders: incremental and absolute, which both provide a digital signal allowing the determination of the shaft position. In some cases, they can provide very accurate measurement, which could easily match with the wire scanner specification; however, they have some characteristics that make them inappropriate, as the built-in optoelectronics and semiconductors are incompatible with radiation and bake-out temperature.

The resolver consists of a wound rotor and stator as shown in Fig. 4.2, b. The windings on the rotor generate an AC magnetic field with a sinusoidal distribution. This field induces voltages in the two stator windings whose amplitudes depend on the rotational angle of the rotor. To provide sine and cosine signals, the two secondaries are wound in space quadrature (90 physical degrees apart) in the stator. Sine and cosine signals are treated by a resover-to-digital converter (RDC) to extract the absolute shaft position. With a high resistance to temperature, to EMI noise and to radiation effects, they are more robust than the optical encoders. However, the wound rotor and stator make traditional resolver not vacuum compatible.

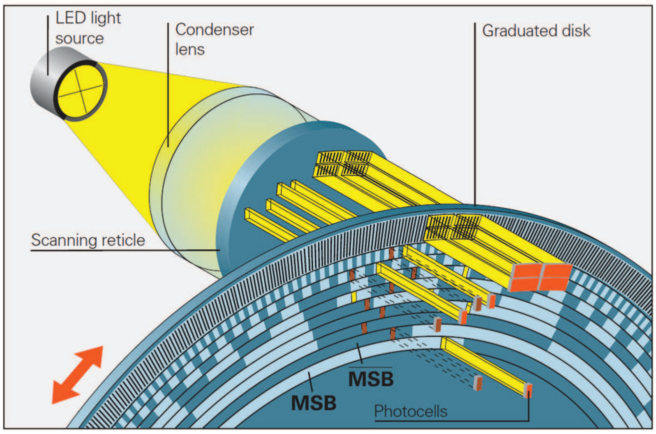

(a)

(b)

Figure 4.2: (a) HEIDENHAIN Absolute optical encoder (b) MOOG Resolver.

Some manufacturers propose UHV compatible angular sensors as Renishaw RGH25F UHV, RGH20F UHV (Fig. 4.3), even if they can provide very high accuracy and low outgassing rate, they cannot withstand high bake-out temperatures and they are not radiation tolerant.

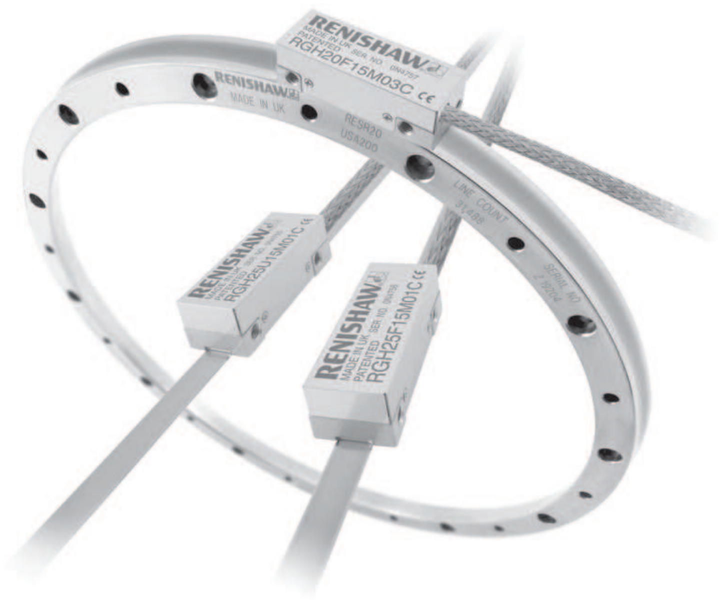

Figure 4.3: Renishaw UHV encoders are compatible with vacuum pressures as low as 10^{-11} *TORR*.

In the begining, numerous angular position sensor have been studied from different companies and countries. Unfortunatly, no commercially-available angular transducer is fulfilling the WS specification. As a result, we can say we did not find completely satisfying technologies in the current market. That is to sayame obvious that our problem cannot be solved by common solutions. Naturally, we began to look for more complexe technologies which would allow modifications to meet the specification. Thus, all technologies that are introduced bellow have the option to be modified on our demand by the companies even, if they pattented by them. All the modification possibilities have been discussed with these companies.

As mentioned before, the basic of the self products cannot be used directly. So we only introduce the possibilities given by the modified version of the products. We now introduce all the sensors we preselected and give a description of their advantages and drawbacks based on the criteria required by the WS. These criteria are

- Accuracy,

- Vacuum compatibility,
- Temperature tolerance,
- Radiation tolerance,
- Mechanical integration.

4.3.1 Rotasyn Solid Rotor Resolver

The Rotasyn (Fig. 4.4), unlike the traditional brushless resolver, has both primary and secondary windings in the stator and thus no rotary transformer is required. The transferred energy remains magnetic from the primary coil through the air gap to the sinusoidally shaped poles of the solid rotor. The rotor works as a magnetic valve completing the flux path. The total flux through the gap is constant, the rotor determines the angular position within the stator bore where the coupling occurs, and thus the relative amplitudes of the output signals.

The primary coil is wound circumferentially between the two stators. The two secondary windings are wound in the stator slots in space quadrature (shifted by 90 physical degrees) similar to a traditional resolver. The induced voltage amplitudes correspond to the sine and cosine of the rotor angle as in a traditional resolver (29).

This design gives the Rotasyn unique advantages over traditional brushless resolvers: since the solid rotor has no windings, it is easy to make it vacuum compatible and resistive to radiation and temperature. As for the motor, the stator of the Rotasyn can be placed outside the vacuum chamber and the air-vacuum barrier is obtained by means of a low magnetic permeability thin wall located in the air-gap.

Admotec RO Series Rotasyn variable reluctance frameless resolvers provide high performances in measurement and feedback applications where traditional resolvers fail to do so. The Rotasyn has fewer parts and a solid rotor without windings, making it much simplier than traditional brushless resolvers. Since the solid rotor has no coils and the stator has only half the number of windings of a traditional brushless resolver, reliability is significantly increased. The solid rotor allows operations with the rotor immersed in hydraulic oil or other liquids. The Rotasyn resolver is mechanically and electrically compatible with traditional brushless resolvers and can replace them as original equipment or in existing applications. If the standard products do not meet

Figure 4.4: A selection of several Rotasyn, solid rotor resolvers from Admotech.

the requiements, custom versions can be designed.

Accuracy: It provides an absolute position measurement with an accuracy of ± 60 *arc minutes* ($17.45mRad$) and a largely higher reproductibility which allows calibration.

Vacuum compatibility: The used materials for the rotor are fully compatible with the vacuum specification.

Temperature tolerance: The rotor can resist more than $230^{o}C$ and the stator can be put off during the back-out phases.

Radiation tolerance: The coil wire insulations are resistive to few MGy, fulfilling largely the specification.

Mechanical integration: To install the Rotasyn, the mechanical system must be modified. Admotec proposes different elements to make the integration (membrane, frameless resolver) easier.

4.3.2 Farrand Inductosyn Rotary Transducer

Inductosyn rotary position transducer is a printed circuit version form of an electrical resolver. It uses inductive coupling between the moving patterns. It consists of two non-contacting substrate elements, a rotor and a stator. Precision circuit patterns are etched in copper bonded to the surface of Inductosyn disks. The printed circuit pattern comprises hairpin radial turns which repeat on the flat surface of a disk. The application of an harmonic excitation signal on the rotor windings causes two induced voltages in 2-phase windings by inductive coupling. The stator windings are fixed at 90^o angles to each other on the stator and produce the sine and cosine signal. With any Resolver-to-Digital-Converter it is posible to extract the angular position from the induced signals.

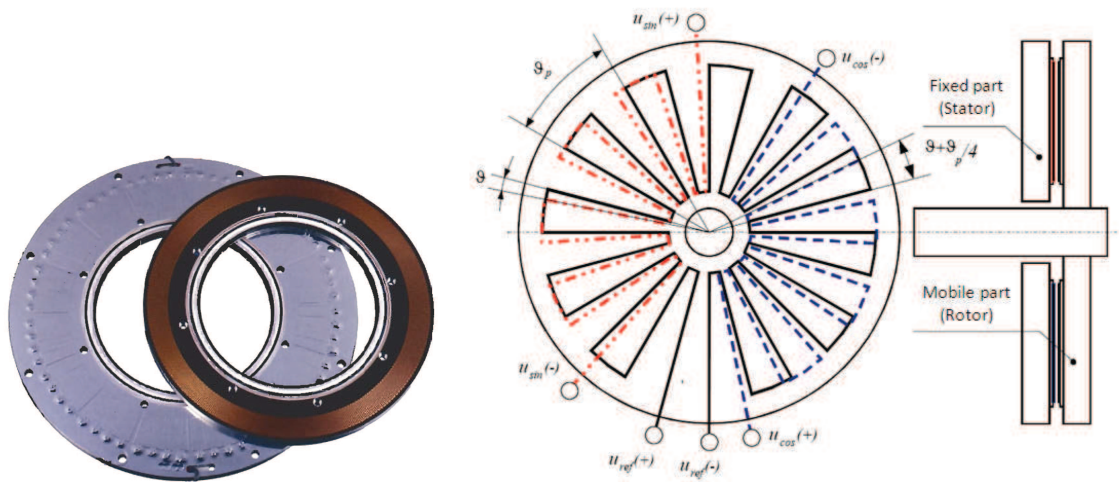

(a) (b)

Figure 4.5: (a) Farrand Inductosyn Rotary Transducer picture. (b) Farrand Inductosyn Rotary Transducer working principle.

Accuracy: Inductosyn position transducers satisfy very high demanding position measurement requirements. Standard units have accuracy of ± 1 *arc second* (4.85 μrad)

and the repeatability is at least 10 times better than the rated accuracy in most cases.

Vacuum compatibility: The printed circuit transducer patterns can be produced on almost any substrate material. This allows to select good material matching with ultra-low outgassing.

Temperature tolerance: Material can be selected to resist periodic high temperature bake-out constraints

Radiation tolerance: Material can be selected to resist ionizing radiation.

Mechanical integration: As the rotor must be excited, Inductosyn rotary position transducers need a slip ring.

4.3.3 Netzer Electric Encoder

Capacitive, absolute, angular sensors convert rotating angle into an output signal based on capacitive interaction between a rotor and a stator. The basic concept comprises two simple electrodes with capacitive coupling. The capacitance is a function of the distance d between the electrodes of a structure, the surface area A of the electrodes, and the permittivity ε of the dielectric between the electrodes:

$$R = \frac{\varepsilon A}{d} \tag{4.1}$$

In the first configuration (Fig. 4.6), the sensor operates with the variation in the effective area between plates of the capacitor. The transducer output is linear with respect to displacement.

In the second configuration (Fig. 4.7), the variation of capacitance is obtained by moving dielectric material between the two parallel plates capacitor, varying the effective dielectric constant, ε. In this case, the output of the transducer is also linear with the plate displacement.

The rotary *Electric Encoder*^{TM}, supplied by Netzer company, is implemented using either of the two topologies: $3 - plate$ or $2 - plate$, both include a space/time

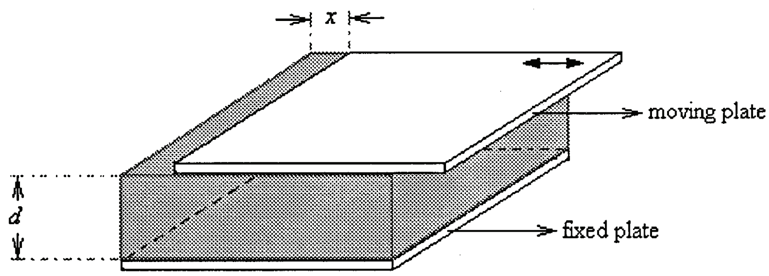

Figure 4.6: Variation of the effective area between plates of the capacitor.

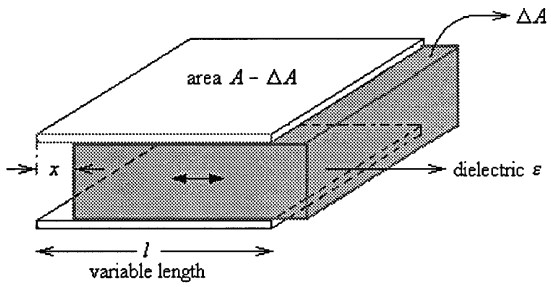

Figure 4.7: Variation of capacitance obtain by moving dielectric material between the two parallel plates.

modulated electric field inside a shielded space. The total field is integrated and converted into a signal current which is processed by an onboard electronics to provide DC output signals proportional to the sine and cosine of the rotation angle. Fig. 4.8a shows the $3 - plate$ topology, where the rotation angle of the dielectric rotor influences the field between stationary transmitter and receiver plates. Fig. 4.8b shows the $2 - plate$ topology, where the field is confined between a stationary transmitter/receiver plate and a conductively patterned rotor.

Accuracy: It provides an absolute position measurement accuracy in the range of several arc minutes. However, it is possible to reach a higher accuracy by calibating the sensor.

Vacuum compatibility: The printed circuit transducer patterns can be produced on almost any substrate material. This allows to select a material matching the ultra-low outgassing requirements.

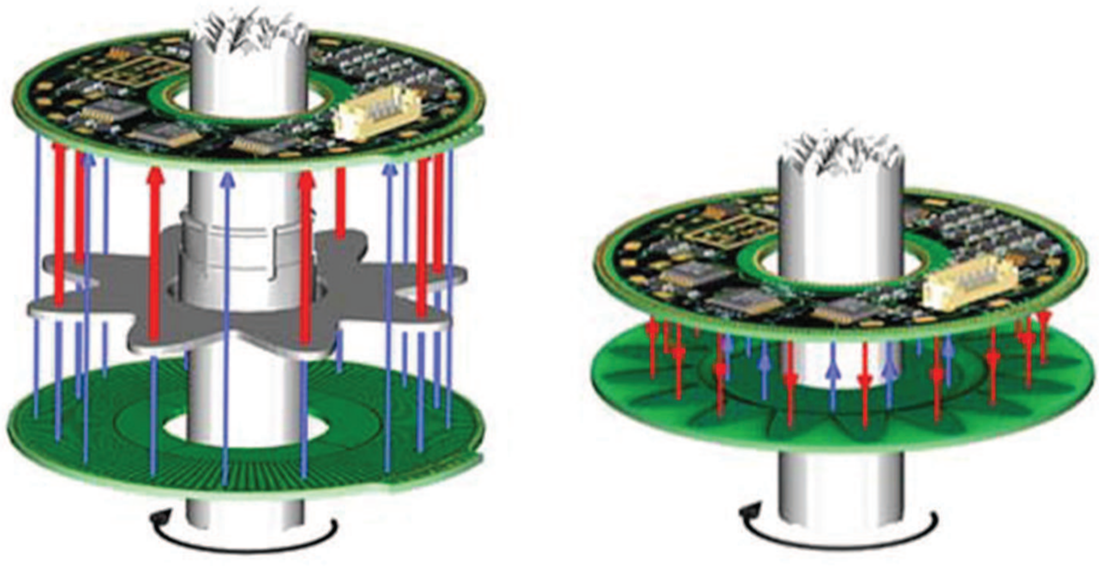

(a) (b)

Figure 4.8: *Electric Encoder^{TM}* (a) 3-plate topology (b) 2-plate topology

Temperature tolerance: Material can be selected to resist periodic high temperature bake-out constraints.

Radiation tolerance: As there are electronic components on the stator plate, these components must be radiation tolerant.

Mechanical integration: The position must be sensed through the vacuum chamber.

4.3.4 Farrand Electrosyn Rotary Transducer

The Farrand Electrosyn rotary transducer (Fig. 4.9) is an analog position sensor which is based on capacitive coupling between its fixed and moving elements to measure rotary displacement with high accuracy, resolution and repeatability.

It comprises two direct mounted elements: the rotor and the stator. The rotor pattern is excited with a high frequency AC signal. The rotor pattern is an arrangement of printed circuit traces which, when excited, is capacitively coupled to the two stator patterns. Relative motion between the rotor and stator makes vary the amount of coupling between the rotor and stator patterns. The patterns are designed so that the outputs of the stator patterns are sine and cosine modulations of carrier waves. Since the format of these output signals is essentially the same for Inductosyn position transducers and wire wound resolvers, any resolver-to-digital converter (RDC) can be adapted to be used with Farrand Electrosyn transducers.

The Farrand Electrosyn transducer elements are typically flat plates carrying an array of conductive traces on one surface. The supporting plate is usually non metallic, although almost any material can be used. The conductive pattern can be almost any conductive material. This allows to select an appropriate material matching with ultra-low outgassing, ionizing radiation resistance and periodic high temperature bake-out compatibility. Farrand Electrosyn transducers are capable of providing absolute position information over the range of one electrical cycle (30).

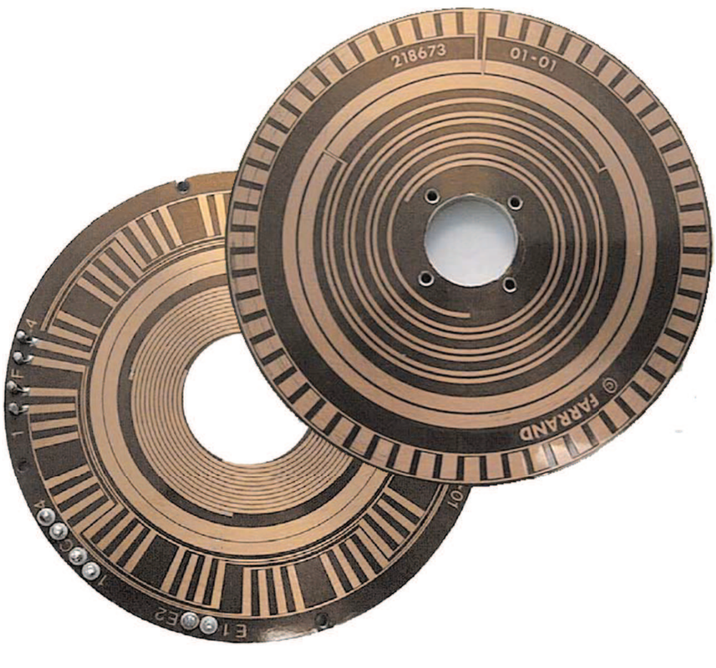

Figure 4.9: Farrand Electrosyn Rotary Transducer picture.

Moreover, a configuration of the Farrand Electrosyn transducers allows continuous rotational motion without the need for a slip ring assembly. This is accomplished by incorporating capacitive coupling rings into the rotor and stator patterns. The excitation signal is connected to the stator rings and couples across the air or vacuum gap to the rotor rings.

However, a disadvantage of Farrand Electrosyn rotary position transducers is the requirement of an amplifier as close as possible, because of the low signal voltage generated.

Accuracy: Electrosyn position transducers satisfy very high demanding position measurement requirements. Standard units have accuracy of ± 1 *arc second* (4.85 μrad) and a repeatability is at least 10 times better than the rated accuracy in most cases.

Vacuum compatibility: The printed circuit transducer patterns can be produced on almost any substrate material. This allows to select materials matching with ultra-low outgassing rate requiement.

Temperature tolerance: Material can be selected to be compatible to periodic high temperature bake-out constraints.

Radiation tolerance: Material can be selected to resist the ionizing radiation. Radiation tolerant preamplifiers are needed in the tunnel.

Mechanical integration: Configuration of the Farrand Electrosyn transducers allows continuous rotational motion without the need for a slip ring assembly.

4.3.5 Micronor Fiber Optical Rotary Encoder

Micronor company has developed, patented and commercialized all-optical, totally passive Fiber Optical Rotary Encoder (FORE) series. FORE system consists of a passive encoder (Fig. 4.10, b), an active remote encoder interface (REI) module (Fig. 4.10, c), and a simple 62.5/125 multimode fiber link that connects the two other (31).

Two light signals are combined onto one fiber and the transmission is bidirectional. Both the light source signal transmitted to the encoder and the return signals pass over the same single fiber.

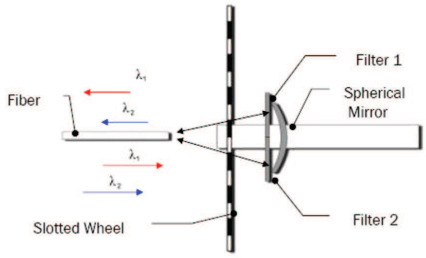

(a)

(b)

(c)

Figure 4.10: a) Schematic of FORE b) 3D drawing of the FORE c) Picture of the FORE interface

To generate the conventional A/B signal of an incremental encoder, the REI control unit generates two light signals with different frequencies and transmits them to the decoder in the same fibre.

The advantages of this system are given by non-integral electronics within the encoder housing and the all-optical parts require just a single optical fiber connection. It is relatively easy to make this passive encoder vacuum compatible and radiation and bake-out temperature tolerant. The higher commercially-available sensor measures angular position from 0^o to 360^o with only 8192 count resolution (resolution of ± 158.2 *arc second* (767 μrad) which is far from our specification.

Accuracy: Standard product provides low resolution and accuracy. However, by increasing the diameter of the disk, it is possible to increase the number of count resolution.

Vacuum compatibility: The optical disk and its patterns can be produced on almost any material. This allows to select good material matching with ultra-low outgassing.

Temperature tolerance: Material can be selected to be compatible with periodic high temperature bake-out constraints

Radiation tolerance: Material can be selected to resist the ionizing radiation

Mechanical integration: Configuration of the Fiber Optical Rotary Encoder allows continuous rotational motion without the need for a slip ring assembly.

4.3.6 Summary

To simplify the comprehension of the choice, a diagram has been drawn, which sums up all the match possibilities of each preselected sensors (Fig. 4.11). The diagrams has a pentagon form whose every apex are development easiness degree.

A mark between 1 an 4 has been given and corresponds to :

- **Mark 1:** Highly complex modification needed
- **Mark 2:** Complex modification needed
- **Mark 3:** Relatively easy modification needed
- **Mark 4:** No modification needed

From Fig. 4.11, it is possible to evaluate qualitatively which sensor is the most appropriate for the WS application regarding the comparison criteria. Thus, the most appropriate sensor is the Fiber Optical Rotary Encoder.

4.4 The proposed solution for the position measurement

4.4.1 Description

The proposed solution is a comercially-available solid rotor resolver (Rotasyn) and an optical fiber based on a rotary encoder which consists of a rotating disk, an optical fiber feedthroughs and a deported optoelectronics interface. The disk, mounted on the shaft, has patterns of reflective and transparent sectors printed on it by photolithography process(Fig. 4.12).

When the disk rotates, these patterns refelect back intermittently the laser beam to the same fiber. The optoelectronics interface, located up to 250 m far away, processes the modulated light to determine the accurate relative position of the wire. In order to

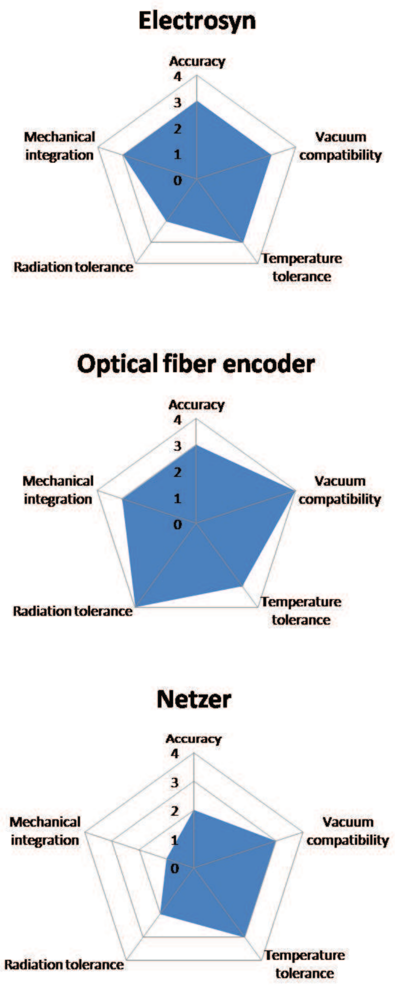

Figure 4.11: Multi-criteria comparison.

validate this optical fiber encoder, a test bench has been produced, where the optical fibers can be set in different relative positions by means of 2 sets of 3 axis linear stages.

The different tests and results are presented and discussed in (4).

4.4.2 Optical fiber encoder test set-up

In order to develop the optical fiber encoder, a flexible test set-up (Fig. 4.13) was designed allowing to answer several points such as :

- type of optical fiber to be used;

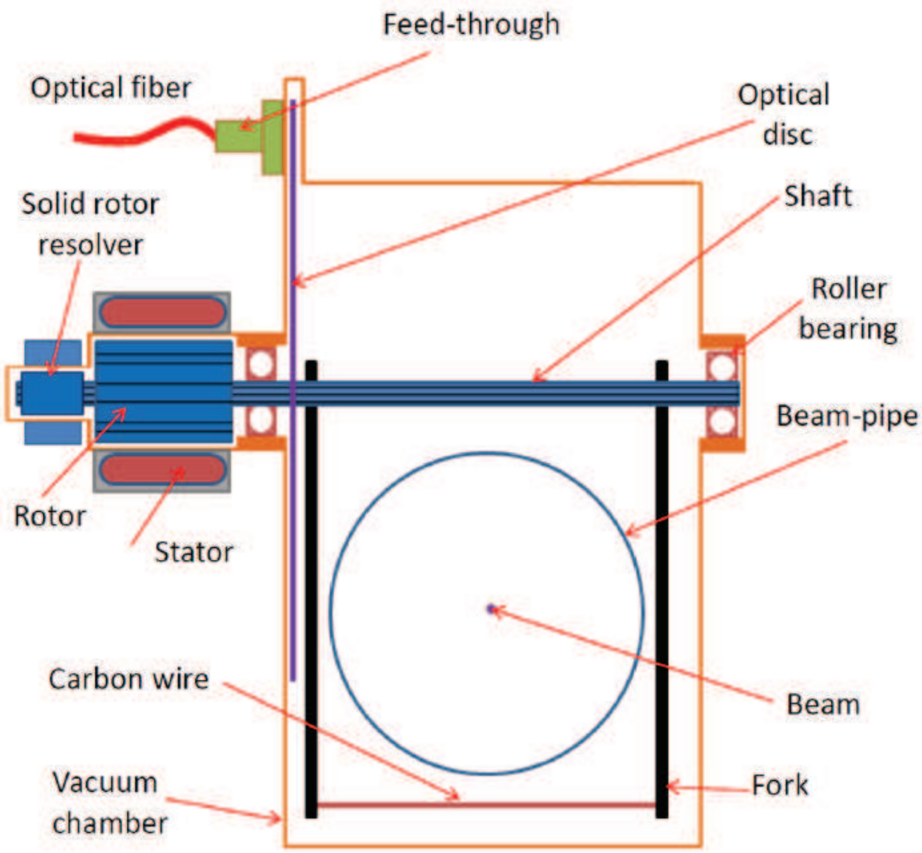

Figure 4.12: Final configuration for the angular position measurement.

- comparsoni optical simulation with the values;
- determination of the parameter variation range;
- test reliability of set-up.

Optical fiber encoder test set-up consists of

- a disk with patterns of opaque and transparent sectors printed on it by photolithography process;
- an optical fiber and feedthrough;
- a deported optoelectronics interface;

- 2 sets of 3 axis linear stages;
- a high accuracy encoder (the same for the drive set-up).

In this part, we describe each of the elements of the optical fiber encoder. Thus, we give an overview of the first results allowing to conclude positively on the feasibility of the final optical fiber encoder.

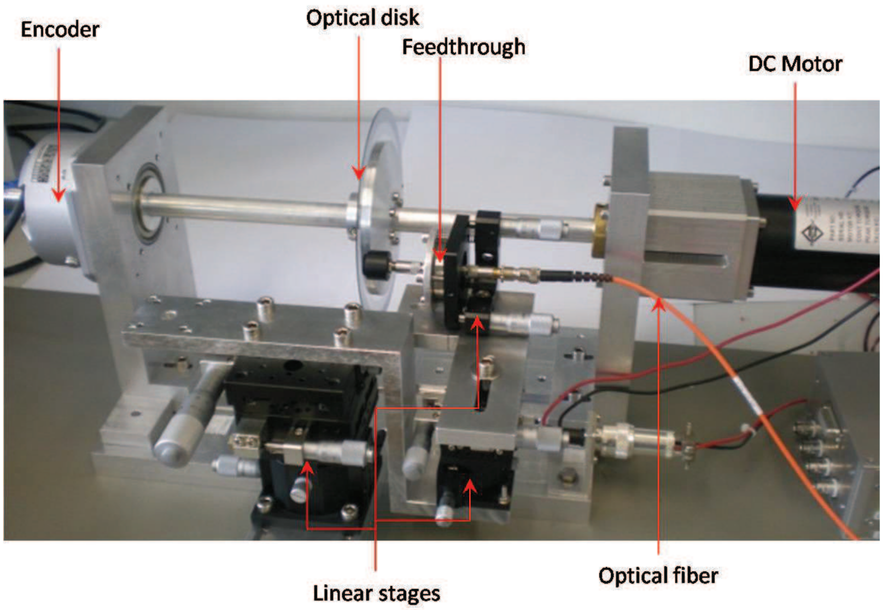

Figure 4.13: Optical fiber encoder test set-up.

4.4.2.1 Optical disk

The optical disk (Fig. 4.14) is made up of 1.5 mm thickness and 140 mm diameter glass substrate on which patterns of shiny chromium are printed by photolithography process. The material of the disk is not selected according to the environmental constraints. The aim of this test set-up is to validate the requirements accuracy of the system.

The patterns consist of 4 tracks with graduations of 50 μm, 70 μm, 100 μm and 150 μm allowing to make test for different configurations.

4.4.2.2 Fiber optic vacuum feedthroughs

Fiber optic vacuum feedthroughs are used to make connections between a vacuum chamber and the outside world. A short section of fiber is mounted on a port through

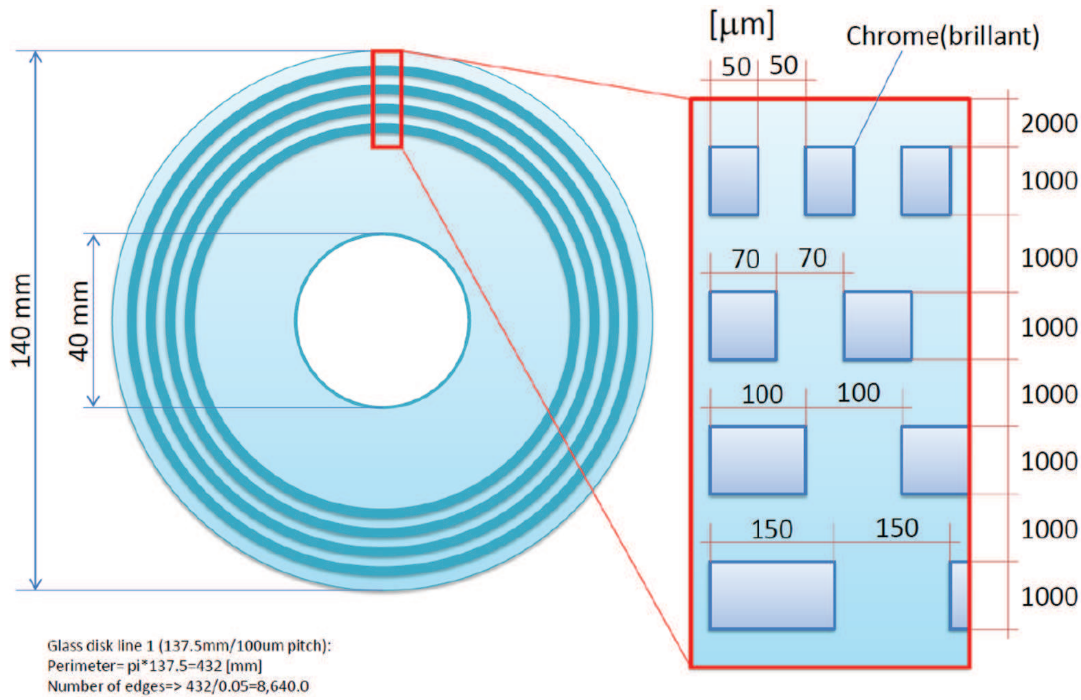

Figure 4.14: Optical disk.

the wall of the chamber and is sealed. The fiber optic cables can be attached to either side of feedthrough. Usually, feedthroughs are designed for high temperature and after some modifications they are ionizing radiation tolerant.

For the test set-up, we selected the Vaqtec 1-FO-0300 Fiber Optic Feedthrough (62.5 micron, Graded-Index, Multimode), mounted on a CF16 Flange with Male SMA 905 connectors on each end (Fig. 4.15). On the test set-up, two fiber optic vacuum feedthroughs mounted on flanges are placed on each side of the disk to allow various studies.

4.4.2.3 Final experimental results

This fiber encoder provides a resolution of 157 μRad with a track of 10μm slits, and two position references using only one channel. An accuracy of ± 25 μRad is reached by angular calibration with a commercial encoder Heidenhain RON225. With this calibration, eccentricity errors, and partly grating errors can be minimized (4.16).

The final system is UHV compatible with EMI immunity, works with temperatures up to 200^oC, and is radiation tolerant due the special fibre used. Studies are on-

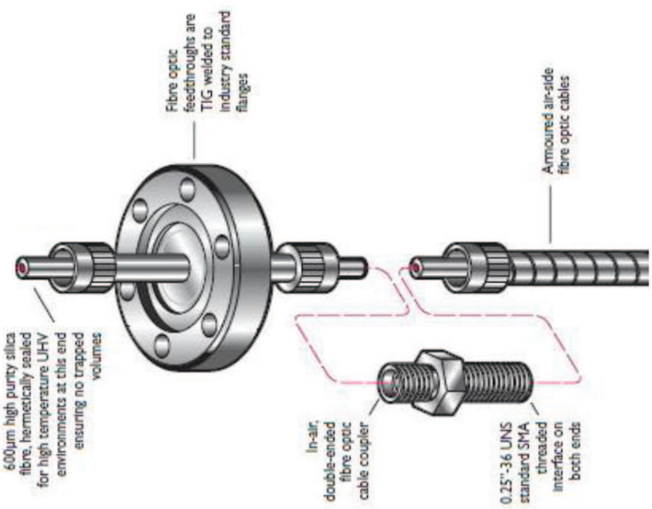

Figure 4.15: Fiber optic vacuum feedthrough.

going to verify the use of a 5 μm track to reach better mechanical resolutions (around 70 μRad), and the incorporation of other calibration methods on the scanner working axis to perform a more reliable calibration procedure (4).

Parameters	Values
Materials	$SS, Glass - Ceramic,\ FusedSilica$
Gender	$Male/Male$
Max. Operating Temp.	250^oC
Min. Operating Temp.	-269^oC
Max. Vacuum Level	$1.10^{-10}\ Torr$
Contact Material	62.5 $micron$
Operating Wavelength Optimized	850 $nm\ and$ 1300 nm
Contact Material	62.5 $micron$
Numerical Aperature	$0.27\ \pm 0.02$
Fiber Profile	$Graded - Index,\ Multimode$

Table 4.1: Fiber optic vacuum feedthroughs parameters

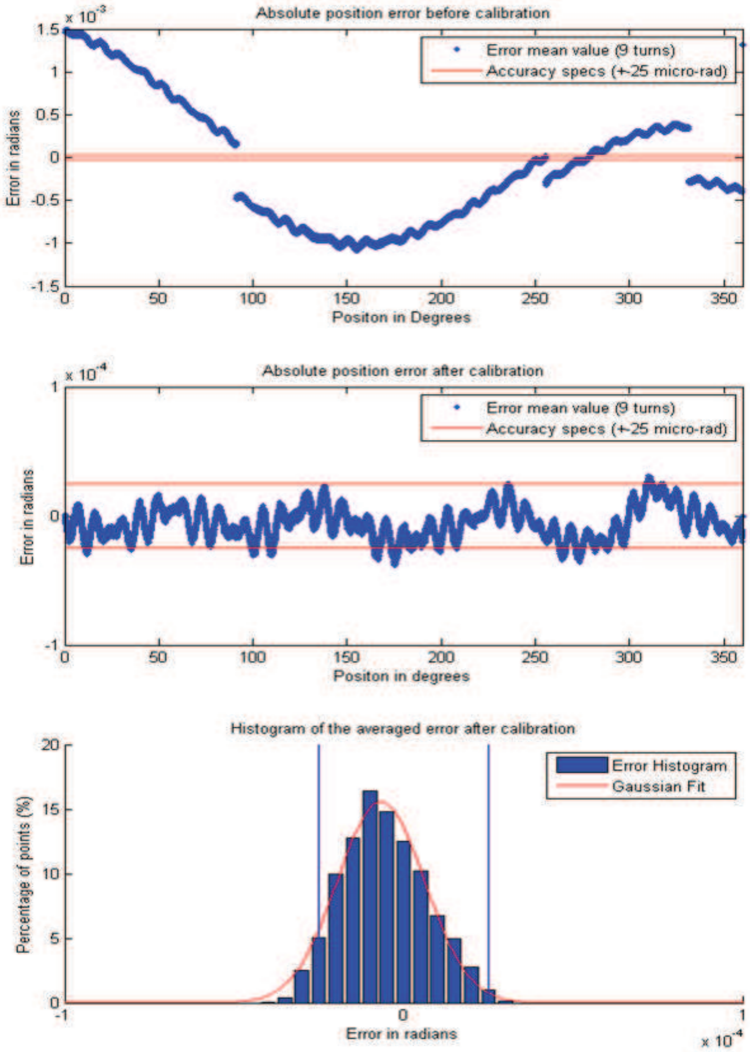

Figure 4.16: Error before calibration (top), calibration applied (center) and error histogram (bottom). Calibration made with Heidenhein RON225 angular position sensor (4).

5

Control

In the previous chapters, the design aspects including the specification, the selection and the sizing of the different components of the wire scanner device were mainly developed. The motor, its power supply, the vacuum barrier and the high accuracy angular sensor are now well identified. To make possible the functioning of the real validating prototype, a control strategy is required. In this chapter, the proposed control algorithm of the Wire Scanner actuator is discussed. This algorithm consists of three cascade control loops (position, speed and current) based on the PMSM vector control and the well-known dq dynamic modeling. The effects of the power supply and the vacuum barrier are also taken into account. After exposing this control based model and the control global diagram and after explaining its main loops, a theoretical study on the different regulators is presented to show how these devices are designed in the framework of this thesis work. The transfer functions are used to define the parameters of IP controllers for the currents, speed and position control. For a more realistic control of the WS system, a vibration study on the fork-wire system is carried out in particular to optimize the speed and position profiles with respect to the wire vibrations. This chapter finishes with a presentation of some results of simulations to check the validity of the proposed algorithm of control.

5.1 Introduction

From the functional aspect point of view, the wire scanners control system can be described as in the following diagram:

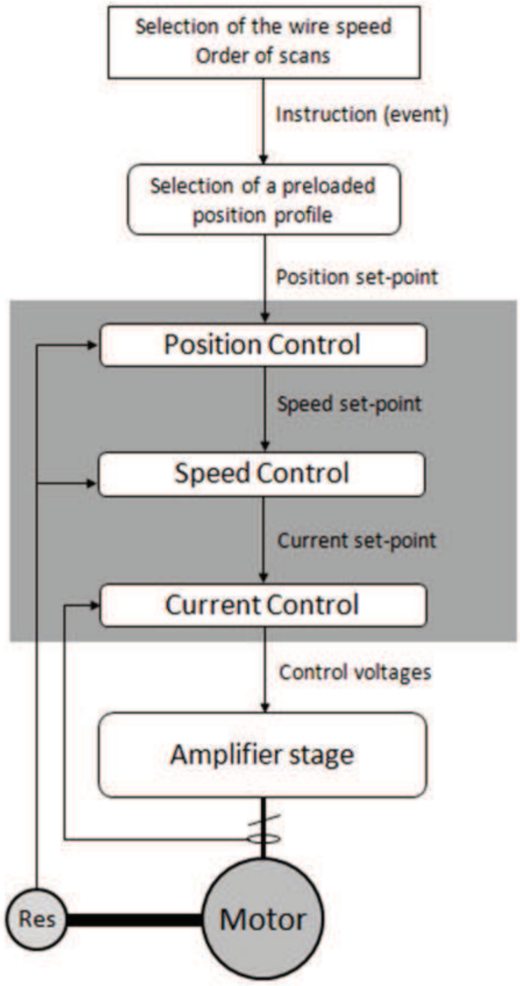

Figure 5.1: Wire scanners control system diagram.

- CERN machine operators can select the wire scan speed and can give the instruction to start a scan by pressing a START button;
- The motion profile generator allows to select the right motion profile and to generate it when the operator asks for it. It consists of pre-calculated and preloaded position profiles corresponding to different wire scan speeds;

- The position-speed-torque controller receives at each cycle the reference position from the motion profile generator. It also receives the position, speed and current measured by a resolver for the speed and position and by three Hall-effect transducers for the current. By comparing the reference value and the measured value for each cycle, it determines the right value of current to be provided to the motor;

- The power stage is based on 3-phase linear power supply, containing 3 power operational amplifiers used in non-inverting configuration. It is driven with 3 analog voltages provided by 3 digital-to-analog converters (DACs);

- The current sensors allow to measure the current circulating in the 3-phase of the motor by converting these currents into 3 analog voltages that can be treated by analog-to-digital converters in order to get digital values of the currents;

The aim of this section is to design the control part of the wire scanner. First, we present models for the PMSM and the linear power supply. Secondly, these models allow the controllers design and the adjustment of their parameters. Third, we study the best configuration for the motion profile. Finally, simulations validate the design.

5.2 System modeling

5.2.1 Motor modeling

In order to limit the model for the controls some assumptions have been made:

- induced voltages are pure sinus (no harmonics);

- the stator windings show a 3-phase distribution (120^o phase shift between them);

- the motor is fully linear (no iron saturation, no iron losses, infinite iron permeability);

- the 3-phase windings are star-connected.

On the basis of these assumptions, the stator d,q equations in the rotor reference frame of the PMSM are

$$L_d \frac{di_{sd}}{dt} = u_{sd} - R_s i_{sd} + \omega_e L_q i_{sq} \tag{5.1}$$

$$L_q \frac{di_{sq}}{dt} = u_{sq} - R_s i_{sq} - \omega_e \psi_f - \omega_e L_q i_{sd} \tag{5.2}$$

where L_d and L_q are d and q axis inductances (H) , R_s stator resistance (Ω), i_{sd} and i_{sq} d and q axis stator currents ($Amps$), u_{sd} and u_{sq} d and q axis stator voltage (V), ω_e electrical speed ($Rad.s^{-1}$), ψ_f mutual flux due to magnet (Wb).

The electric torque of the motor is given by

$$T_m = \frac{3}{2} p(\psi_f i_{sq} + (L_d - L_q) i_{sd} i_{sq}) \tag{5.3}$$

The mechanical equation of the motor is given by

$$J \frac{d\Omega_m}{dt} = T_m - T_l \tag{5.4}$$

where J is the total moment of inertia ($kg.m^2$), Ω_m the mechanical angular velocity ($Rad.s^{-1}$), T_m is the electric torque (Nm), T_l is the load torque (Nm).

$$T_m = \frac{3}{2} p \psi_f i_{sq} \tag{5.5}$$

5.2.2 Power supply modeling

- Output offset voltages are completely compensated;
- The amplifiers operate in the range of power supply (No output voltage saturation);
- The effects of temperature are neglected ;

As discussed, the 3-phase linear power supply is based on 3-power operational amplifiers used in non-inverting configuration (25). Starting from the parameters given by the manufacturer, a simplifed model of the amplifier has been elaborated taking into account the 3 principal limitations, namely:

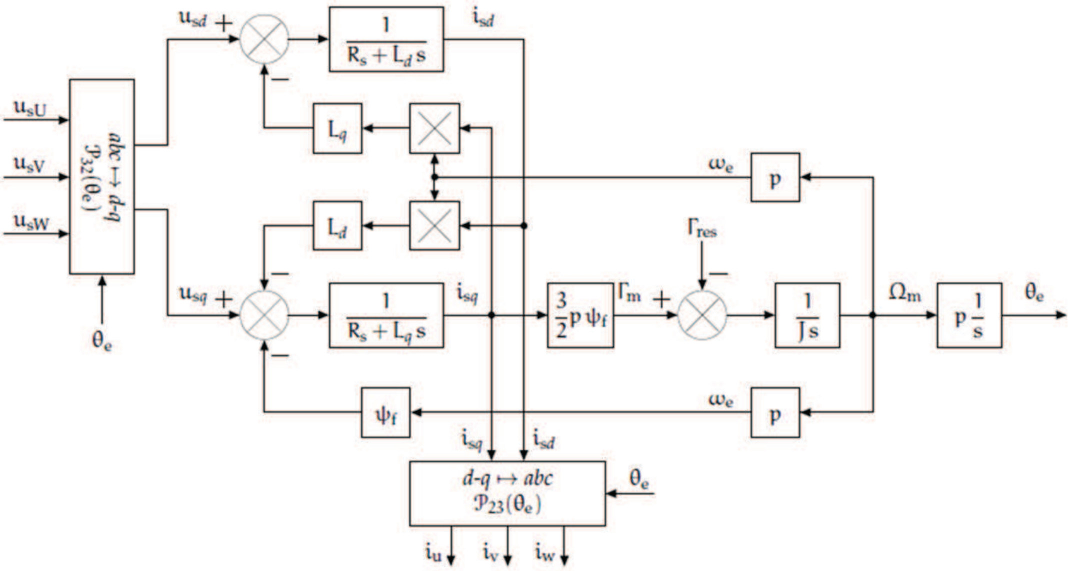

Figure 5.2: dq-model of the PMSM

- The saturation of the output voltage which is limited by the output impedance and the saturation voltage of the output transistor (32). This phenomen is called voltage swing and is defined as a linear function of the output current as follow:

$$U_{swing} = a.I_{out} + b \tag{5.6}$$

- The slew rate (SR) is a limitation on the rate of change in the output voltage of an operational amplifier and can be modeled by a rate limiter.

- The amplifier, used in non-inverting configuration, acts as a closed loop including an open loop first order which can be modeled by a low pass filter (A0, f0, respectively, the open loop gain and cut frequency) and a feedback gain G.

Slew rate limitation

The slew rate of the amplifier is defined as the maximum rate of change of the output voltage and is usually expressed in units of $V/\mu s$.

$$SR = max(\mid \frac{dv_{out}(t)}{dt} \mid) \tag{5.7}$$

where $v_{out}(t)$ is the output produced by the amplifier as a function of time t.

Limitations in slew rate capability can give rise to non linear effects in amplifiers. For a sinusoidal waveform which cannot be subject to slew rate limitation, the slew rate capability at all points in an amplifier must satisfy the following condition:

$$SR \geq 2.\pi.f.v_{pk} \tag{5.8}$$

where f is the operating frequency, and V_{pk} is the peak amplitude of the waveform. If the input is driven above the slew rate limit, the output exhibits a non-linear distortion as shown in the example Fig. 5.3.

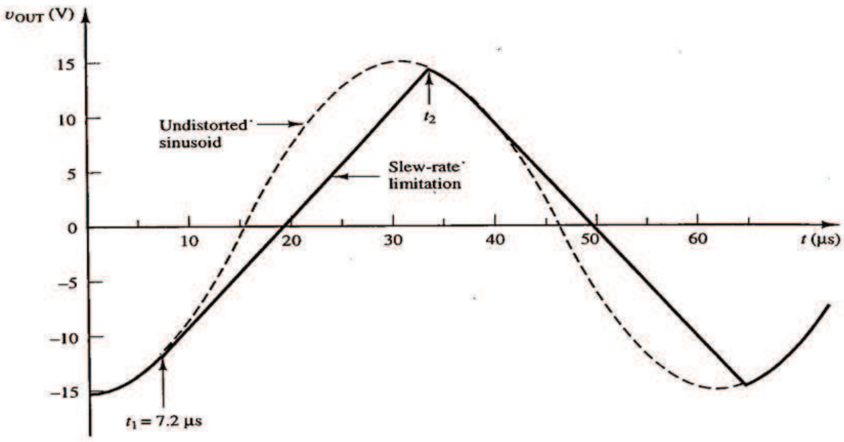

Figure 5.3: Representation of a slew-rate phenomenon.

The effect of the slow rate can be easily modeled by a simple rate limiter block under Matlab/Simulink (Fig. 5.4).

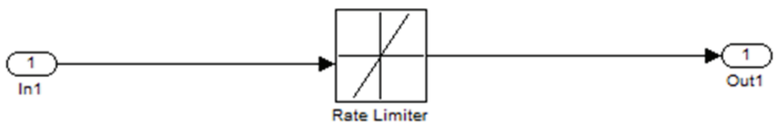

Figure 5.4: Matlab/Simulink rate limiter block which allows to model the slew rate effect.

Frequency response

The gain of operational amplifiers is high and constant for DC and has a very low frequency before decreasing from its cutoff frequency f_{ao}. This decrease is modeled by a model of order 1 which is described according to the pulsation

$$A(j\omega) = \frac{A_0}{1 + j\omega/\omega_{a0}} \tag{5.9}$$

or to the frequency

$$A(j\omega) = \frac{A_0}{1 + jf/f_{a0}} \tag{5.10}$$

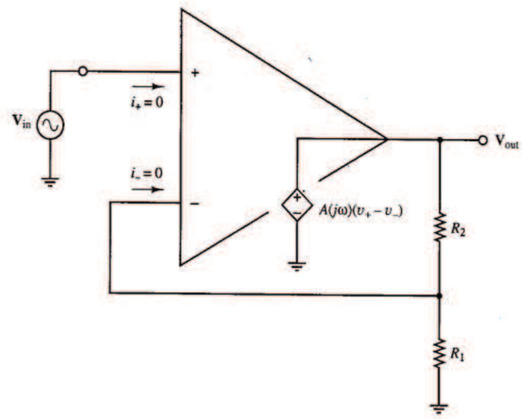

Figure 5.5: Operational amplifier in non-inverting configuration.

The Bode diagram of the frequency response is shown in Fig. 5.6. It shows the gain decreases from $A_0 = 1000000$ and $f_{a0} = 10Hz$ to reach unity-gain at the unity-gain frequency $f_T = 1\ MHz$. This decrease of a decade of gain per decade of frequency is equivalent to a slope of $20dB/decade$. This shows that, for an amplifier whose frequency response is of order 1, the product is a constant gain frequency and in particular, it is

$$A_0.f_{a0} = 1.f_T \tag{5.11}$$

As the gain is not constant, we need to consider it in the evaluation of the amplifier gain.

$$A_U(jf) = \frac{U_2(jf)}{U_1(jf)} = \frac{R_1 + R_2}{R_1} \frac{1}{1 + \frac{1}{A(jf)} \frac{R_1 + R_2}{R_1}} \tag{5.12}$$

Taking into account the gain $A(jf)$ of the amplifier

$$A(jf) = \frac{A_0}{1 + jf/f_{a0}} \tag{5.13}$$

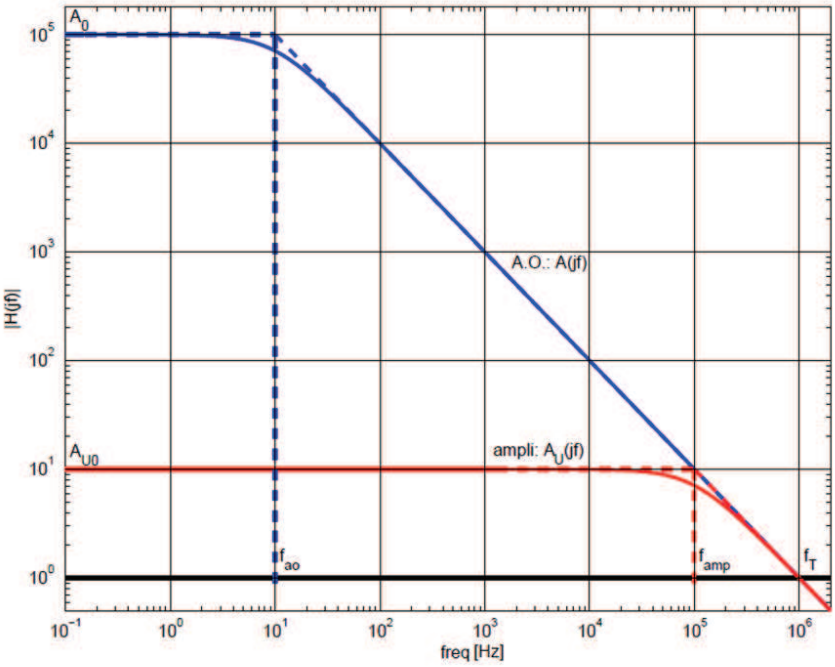

Figure 5.6: Example of operational amplifier gain in open and closed loop.

the gain of the non-inverting configuration amplifier can be written as

$$A_U(jf) = \frac{U_2(jf)}{U_1(jf)} = \frac{R_1 + R_2}{R_1} \frac{1}{1 + \frac{1+jf/f_{a0}}{A_0} \frac{R_1+R_2}{R_1}} \tag{5.14}$$

The development of the denominator gives the following equation:

$$1 + \frac{1 + jf/f_{a0}}{A_0} \frac{R_1 + R_2}{R_1} = 1 + \frac{1}{A_0} \frac{R_1 + R_2}{R_1} + \frac{jf}{A_0.f_{a0}} + \frac{R_1 + R_2}{R_1} \tag{5.15}$$

$$\simeq 1 + \frac{jf}{A_0.f_{a0}} + \frac{R_1 + R_2}{R_1} \tag{5.16}$$

By neglecting the term $\frac{1}{A_0} \frac{R_1+R_2}{R_1}$ compared to 1 (as A_0 is very high), the denominator is reduced to a simple first order which shows the characteristic frequency f_{amp} of the non-inverting configuration amplifier

$$1 + \frac{jf}{A_0.f_{a0}} + \frac{R_1 + R_2}{R_1} = 1 + \frac{jf}{f_{amp}} \tag{5.17}$$

with

$$f_{amp} = A_0.f_{a0}\frac{R_1}{R_1 + R_2} = f_T.\frac{R_1}{R_1 + R_2} \tag{5.18}$$

This characteristic frequency f_{amp} represents the bandwidth of the non-inverting configuration amplifier frequency and can be written as

$$A_U(jf) = \frac{R_1 + R_2}{R_1}\frac{1}{1 + \frac{jf}{f_{amp}}} \quad avec \quad f_{amp} = f_T\frac{R_1}{R_1 + R_2} \tag{5.19}$$

This frequency response of the non-inverting configuration amplifier is shown in Fig. 5.6.

We can deduce that the higher the amplifier gain is the lesser the bandwidth is.

5.3 Controller design

Fig. 5.7 shows an position/speed/current cascaded loops control diagram which allows mechanical position control of the PMSM. The reference position θ_{m_ref} is precalculated and preloaded in an external digital board (not represented on the Fig. 5.7). The measured mechanical position is subtracted from the reference mechanical position and the obtained error is fed into a proportional type controller which generates the speed reference ω_{m_ref}. When a position command is given, the mechanical speed is increased and maintained as long as needed in order to bring the rotor to the commanded position.

The speed error is obtained by subtracting the measured mechanical speed ω_{m_meas} from the reference speed ω_{m_ref}. The PI speed controller outputs the torque command T_{m_ref}. The machine produces electromagnetic torque as much as it is necessary to maintain its reference speed.

The instantaneous currents through the stator windings of the PMSM are measured by means of current transducers. The measured currents are transformed to the 2-phase coordinated system fixed on the rotor by means of mathematical calculations using the *abc to dq* transformation.

The torque command T_{m_ref} generates the $q-axis$ reference currents. In this case, the $d-axis$ reference current is set to 0 A since the controlled machine is surface-mounted-PMSM and the constant torque angle control property is used ($I_d = 0$ control property) (33). The current errors generated by subtracting the values of the measured current from the reference currents are input of the PI current controllers which output the $dq - axis$ reference voltages.

The $dq - axis$ reference voltages are transformed to abc voltage reference values which are fed by the 3-phase amplifier through 3 digital-to-analog converters (DAC) (not represented on Fig. 5.7).

Decoupling of the $d - axis$ is performed by adding to the $d - axis$ reference voltage, the coupling term

$$L_d.\omega_e.i_d \tag{5.20}$$

Decoupling of the $q - axis$ is performed by subtracting from the $q - axis$ reference voltage the coupling term

$$L_q.\omega_e.i_q \tag{5.21}$$

This decoupling allows to have d and q $axis$ completely independent to each other. It also simplifies the equation representing the machine and makes the synthesis of the controllers' easier so that the control is more precise (33).

The resolver-to-digital converter (RDC) outputs the mechanical rotor position and speed of the machine.

The advantages of cascaded loops control presented are

- Faster transient response
- High controllability of torque
- Limitation of the current for security aspects of motor and power supply

Control diagram presented in Fig. 5.7 contains 4 PI controllers: two for dq currents regulation, one for speed regulation and one P controller for the position regulation. The aim of controllers design is to select appropriate parameters to obtain proper and stable drive operations. For this, some requirements have been fixed:

- The overshoot must be lower than 5% for the current controllers;
- The rise time for the current controller must be lower than 10 sampling periods (10xTs = 1 ms);

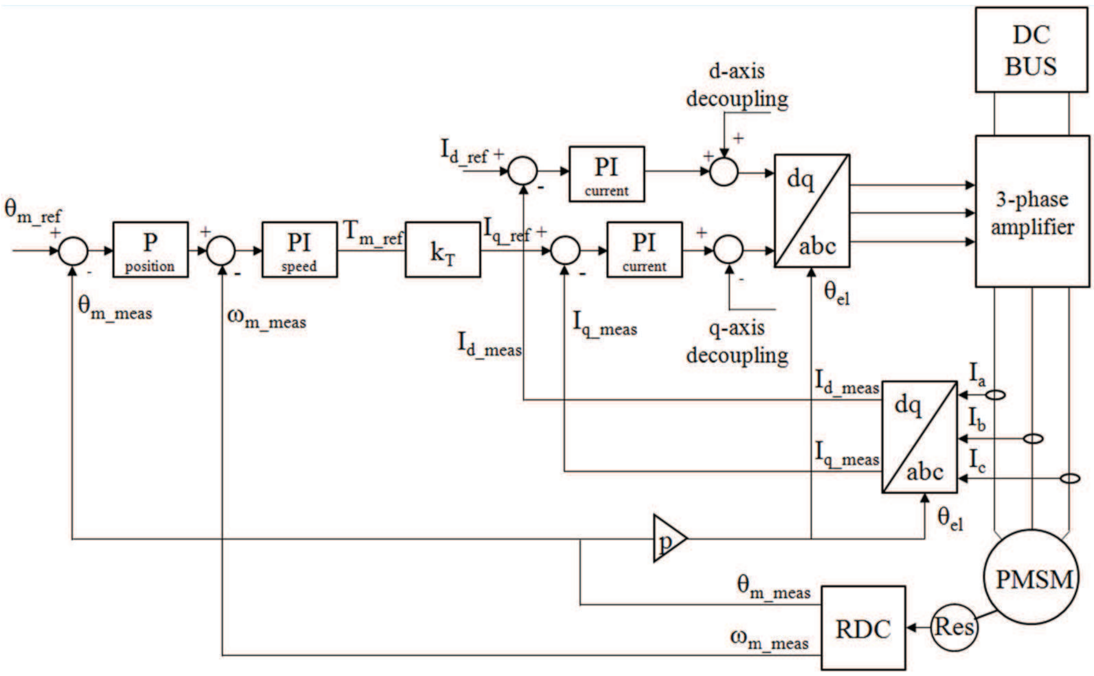

Figure 5.7: Position/speed/current cascaded control loops.

- The overshoot should be lower than 10% for the speed controllers;
- The rise time for the speed controller should be lower than 100 sampling periods (100Ts = 10ms);
- The bandwidth of the speed controller should be at least 10 times lower than the bandwidth of the current controller;

Starting from these requirements, current, speed and position controller parameters have been adjusted with the Matlab/Sisotool package

5.3.1 Current controller design

Before doing the controller design, it is necessary to determine the objet to be controlled (it is named 'plant'). From motor equation we know that

$$L_d.s.I_{sd}(s) = U_{sd}(s) - R_s.I_{sd}(s) + \underline{\omega_e.L_q.I_{sq}(s)}; \tag{5.22}$$

$$L_q.s.I_{sq}(s) = U_{sq}(s) - R_s.I_{sq}(s) - \omega_e.\psi_f - \underline{\omega_e.L_d.I_{sd}(s)}; \tag{5.23}$$

with respectively R_s is the resistance of the stator windings, L_d and L_q are direct and quadrature inductances, I_{sd} and I_{sq} are the direct and quadrature current, U_{sd} and U_{sq} are the direct and quadrature voltage, ω_e is the electrical speed and ψ_f is the flux induced by the permanent magnets in the stator windings.

The underlined terms are the cross coupling between d and q loops which can be cancelled by adding or substracting decoupling terms. This operation simplifies considerably the equation and after few mathematical manipulations, the transfer function of the plant can be formulated by the following equations

$$P_d(s) = \frac{I_{sd}}{U_{sd}} = \frac{1}{R_s + s.L_d}; \tag{5.24}$$

$$P_q(s) = \frac{I_{sq}}{U_{sq} - \omega_e.\psi_f} = \frac{1}{R_s + s.L_q}; \tag{5.25}$$

The term $\omega_e.\psi_f$ is considered as a disturbance and is neglected in further analysis; Supposing that $L_d \approx L_q$ because the machine is surface-mounted PMSM, it can considered that the transfer function of d and q axis is identical.

Thus, the simplified transfer function of the plant can be formulated as

$$P_{dq}(s) = \frac{U_{sdq}(s)}{I_{sdq}(s)} = \frac{1}{L_{dq}s + R_s}; \tag{5.26}$$

I_d and I_q currents are controlled by Proportional and Integral (PI) controller whose the transfer function is given by

$$C(s) = K_p \frac{1 + s.\tau_i}{s.\tau_i} \tag{5.27}$$

In order to represent better the real system, certain delays have been considered:

- control algorithm delays corresponding to the time needed for necessary calculations (time constant: T_s):

$$ALG(s) = \frac{1}{T_s s + 1} = \frac{1}{0.0001s + 1}; \tag{5.28}$$

- zero-order-hold (ZOH) delays given by holding element keeping the same value during sample period (time contant: $0.5T_s$):

$$ZOH(s) = \frac{1}{T_s s + 1} = \frac{1}{0.00005s + 1}; \tag{5.29}$$

- sensor delay introduced by current sensor, which samples and holds read value (time contant: $0.5T_s$):

$$SEN(s) = \frac{1}{T_s s + 1} = \frac{1}{0.00005s + 1}; \tag{5.30}$$

- amplifiers delay introduced by bandwidth limitation of the amplifiers having a first order function with a time constant of T_a:

$$AMP(s) = \frac{1}{T_a s + 1} = \frac{10}{0.000001s + 1}. \tag{5.31}$$

The block diagram of the current close-loop including PI controller, delays and the plant to be controlled, is shown in Fig. 5.8.

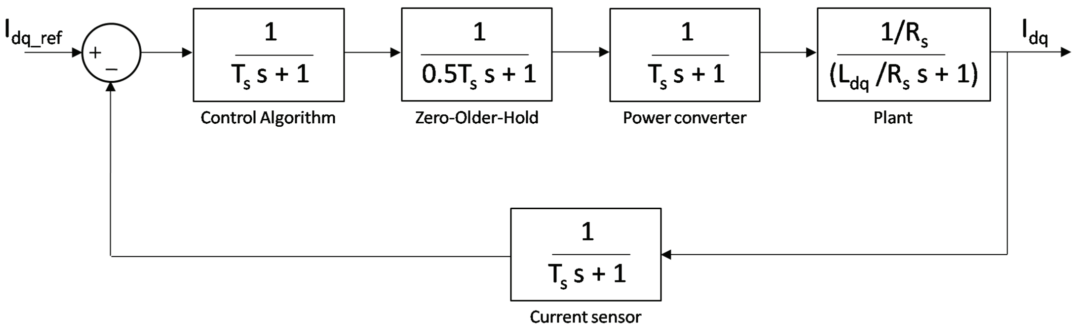

Figure 5.8: Block diagram of the i_{sdq} current close-loop including PI controller, delays and plant.

Starting from this loop, PI current controller parameters are adjusted using the Matlab/Sisotool package and are given as

$$C(s) = K_p \frac{1 + s.\tau_i}{s.\tau_i} = 112 \frac{1 + 0.001s}{0.001s} \tag{5.32}$$

As shown in the step response in Fig. 5.9, the rise time for the current controllers is $t_{rise} = 0.56\ ms$ while the overshoot is $OS = 1.86\%$. The designed current controller complies with the design requirements, for both the rise time and overshoot are within acceptable limits. The current settles in $t_{settling} = 0.879\ ms$ and the final value is 1.

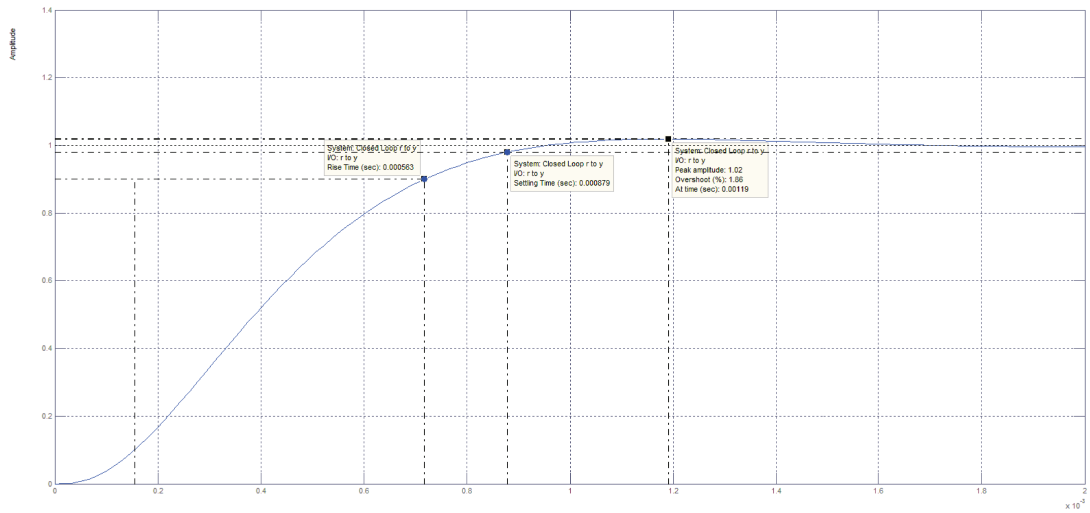

Figure 5.9: Step response of the system with designed controller. Typical characteristics are marked: rising time ($t_{r(10\%-90\%)}$) = 0.56 ms, settling time ($t_{s(2\%)}$) = 0.879 ms, and the maximum overshoot (M_p) = 1.86%

.

5.4 Motion profile design

High accuracy measurement of the wire position implies the use of a low-vibration motion profile. The high running speed and acceleration can cause strong excitations on the mechanical part of the system and more particularly on the wire. The challenge consists in achieving high acceleration and high speed motion with minimized vibrations. Usually, Wire Scanners use simple trapezoidal velocity models, in which the wire is accelerated until a constant velocity by means of a constant acceleration and until zero velocity by means of a constant deceleration.

This profile model allows to achieve fast motions; however, as in Fig. 5.10, at the time instant t_1, t_2, t_3 and t_4, the acceleration jumps from its constant value to zero or conversely. These jumps tend to cause overshoots, and excite vibrations (34).

In this section, we briefly review the specification for the motion profile. Then, in the second part, we provide an overview of different motion profiles which can be used for such a movement. In the third part, the wire vibration behaviour is simulated according to motion profiles previously presented. Finally, the results are discussed and the conclusions are presented.

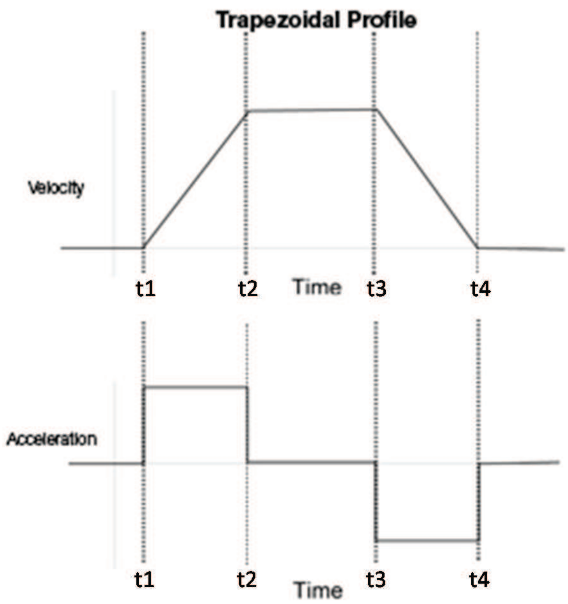

Figure 5.10: Trapezoidal velocity profile example.

5.4.1 Specification

The scan occurs on πrad including:

- acceleration phase $\in [0\ to\ \frac{\pi}{3} rad]$ unitl 210 $rad \cdot s^{-1}$
- constant speed phase$\in [\frac{\pi}{3}\ to\ \frac{2\pi}{3} rad]$ at 210 $rad \cdot s^{-1}$
- deceleration phase $\in [\frac{2\pi}{3}\ to\ \pi rad]$ unitl 0 $rad \cdot s^{-1}$

5.4.2 Type of motion profiles

The studied option can be summarized as follows:

- Trapezoidal velocity profile (Fig. 5.12, left)which produces rectangular acceleration windows. It has been calculated from acceleration and has been integrated two times. While the velocity profile is trapezoidal, the position profile can be described by second-order polynomials. The jerk obtained is in the form of impulses aligned with the edges of the acceleration windows.
- Second-order s-curve position profile (Fig. 5.12, right) which consists of 7 distinct phases of motion: three acceleration, one cursing and three deceleration phases.

For the polynomial models whose orders are higher than 2, the jerk exhibits finite values. So their velocity profiles are smooth during motions. In addition, their kinematic features are described by polynomials. Therefore, they are called polynomial s-curve models.

- Forth-order s-curve position profile (Fig. 5.13, left) which consists of 15 distinct phases of motion.
- Trigonometric position profile (Fig. 5.13, right) which consist of 3 distinct phases of motion: accelerating phase, constant velocity phase, and decelerating phase. It is calculated by integrating three times a sinusoidal jerk.

5.4.3 2D dynamic model of wire vibration

Even if all the elements of the system can vibrate from a mechanical point of view, the more critical is the wire since its flexibility is largely higher than the other elements. In order to have a qualitative overview of the wire vibration behaviour a simplified 2D dynamic model has been used (Fig. 5.11) (35). It consists of an arm which rotates around a fixed axis, in the end of the arm a mass m is fixed by two spring stiffness k. The equilibrium position of the mass point P is P_0. This simplified model is voluntary without any damping.

The differential equation of the motion can be written as follows : (35)

$$\ddot{x} = \ddot{\theta}h + \ddot{\theta}y + 2\dot{y}\dot{\theta} + \dot{\theta}^2 x \tag{5.33}$$

$$\ddot{y} = -\ddot{\theta}x - 2\dot{x}\dot{\theta} + \dot{\theta}^2 h + \dot{\theta}^2 y \tag{5.34}$$

Due to the acceleration a in the mass m resulting from the movement a reaction force F has to equilibrate the system since

$$\sum F = ma \tag{5.35}$$

Moreover, if we assume that the spring forces are proportional to spring length in their main directions, it can be stated:

$$F_1 = -kx \tag{5.36}$$

$$F_2 = -ky \tag{5.37}$$

Thus, the dynamic equation system for the movement of the mass P with respect to the fix reference AB written in the coordinate system 1,2 can be written as follows:

$$\ddot{x} = \ddot{\theta}h + \ddot{\theta}y + 2\dot{y}\dot{\theta} + \dot{\theta}^2 x - \frac{kx}{m} \tag{5.38}$$

$$\ddot{y} = -\ddot{\theta}x - 2\dot{x}\dot{\theta} + \dot{\theta}^2 h + \dot{\theta}^2 y - \frac{ky}{m} \tag{5.39}$$

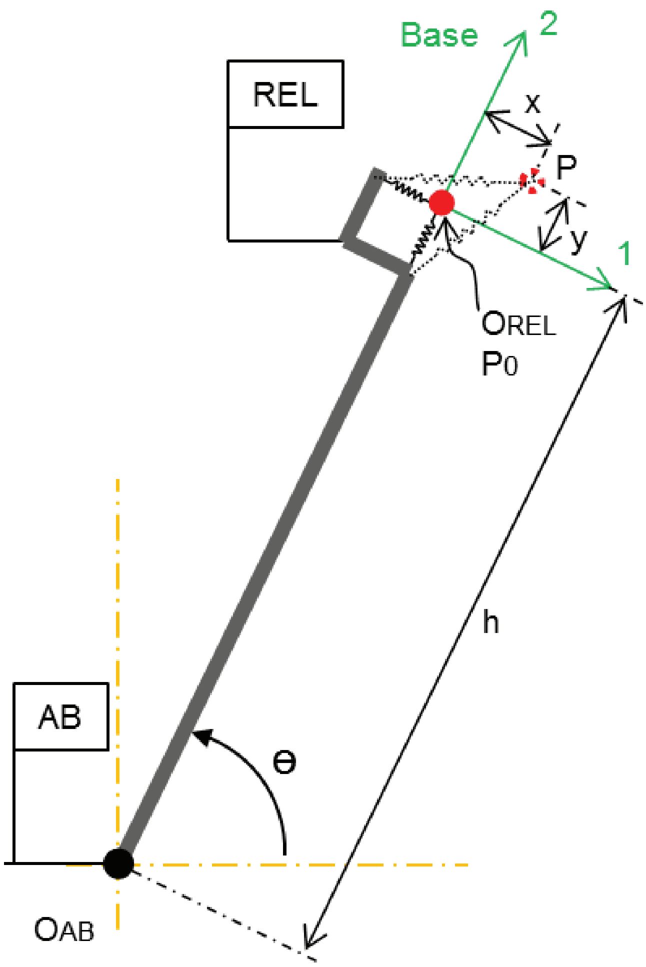

Figure 5.11: Simplified 2D dynamic model of the wire vibration behaviour.

5.4.4 Simulation study of the motion-induced vibration

The aim of this simulation is to see the wire vibration behaviour for different position profiles. For that, servo-loop which controls the rotation of the arm is assumed to be perfect.

Four motion profiles were evaluated for comparison. They were trapezoidal profile, 3rd order s-curve profile, 4th order s-curve profile and trigonometric profile. All these profiles have been designed by iteration to meet the above-mentioned specification.

It must be noted that the most critical aspect is the vibrations on the x axis because this axis is more orthogonal to the beam particles during the scan. And the vibrations on the same axis (y) that the beam particles can be considered as negligible due to the fact that the speed of particules is huge compared to the speed of the wire vibrations (Fig. 5.12 and Fig. 5.13)

The last two charts of each column in Fig. 5.12 and Fig. 5.13 show the amplitude of the mass displacement due to the forces produced by the movement of the arm. Displacement in x direction is mainly dominated by the tangential acceleration seen by the mass. Displacement in y direction is dominated by the normal acceleration which is mainly coupled with the angular speed seen by the mass. Above this main deformation, a ripple can be shown, which is related to the vibrations of the mass-spring system in its natural mode. Thus the amplitude of the ripple can be shown that decreases in the case where smother acceleration profile is used.

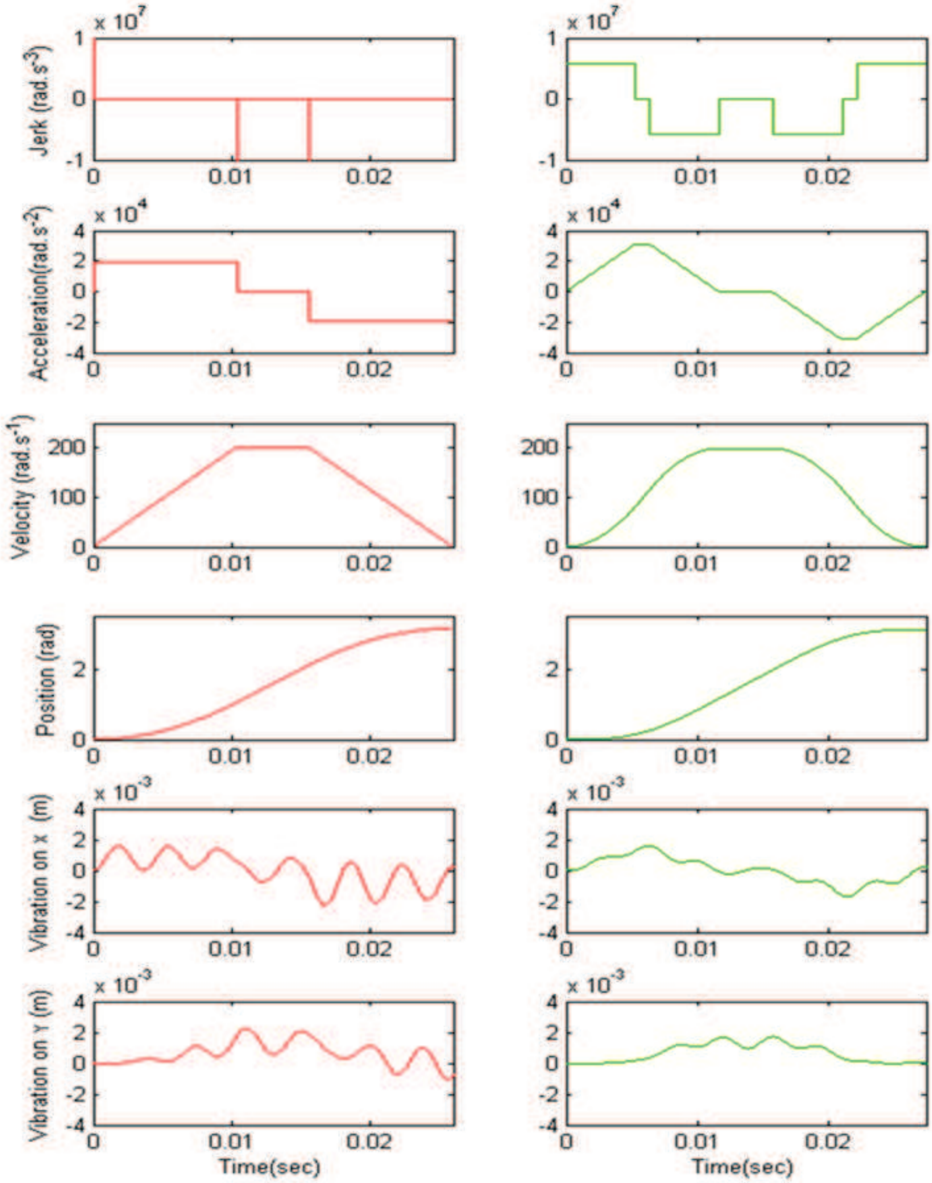

Figure 5.12: Plots of angular jerk, acceleration, speed and position profiles and resulting vibrations of the wire on x and y plans for trapezoidal profile (right) and 2^{nd} order s-curve profile (left).

5.5 Simulation

5.5.1 Description of the Simulink model

Once the model of the motor and the power converter is developed in 5.2, the configuration of control presented in 5.3 and the selected position profile discussed in 5.4, a Simulink model has been elaborated (Fig. 5.14).

Some assumptions limiting the complexity of the model have been made on each device of the developed simulation model. These hypothesis are similar to those explained in the section 5.2.

5.5.2 Simulation results

The purpose of these simulations is to verify that the actuator matches the specification in terms of acceleration, speed and position while being lower than the maximum voltage, current and power that power converter can provide.

In this section, we present the main simulation results obtained with the above-developed program. The used physical parameters are those computed from the datasheet of the manufacturer and presented in Chapter 3. These parameters have been used to compute the gains of different regulators. The aim of these simulations is to check the validity of the developed algorithm to control the PMSM that movers the WS. All the simulations were performed with the same defined position profile, so that the PMSM's rotor moves smoothly from 0 to π during 50 ms. In the same time interval, the angular speed of the rotor has to reach its maximum value in the first 15 ms, then has to stay at this value during about 10 ms before returning to zero in 15 ms. Three cases have been considered according to the maximum value of the speed reference: $\omega_{max} = 100 rad \cdot s^{-}$, $\omega_{max} = 150 rad \cdot s^{-}$ and $\omega_{max} = 200 rad \cdot s^{-}$. The obtained results for each of the 3 cases are exposed on Fig. 5.15, 5.16, 5.17 respectively. The curves in blue present the references, while the ones in green present the measured magnitudes. The mechanical and electrical magnitudes are presented respectively in the left and in the right sides of these figures.

5.5.3 Synthesis on the proposed control

Examining Fig. 5.15, 5.16, 5.17, we can say that all the measured magnitudes follow well their references despite some very small errors which are acceptable in this stage of the study. This result allows us to conclude that the proposed control beahviours fulfill the needed specification of the WS actuator in terms of angular and speed travels but also the acceleration/deceleration, currents and voltages limits. The next step is to implement and to test experimentally this control algorithm.

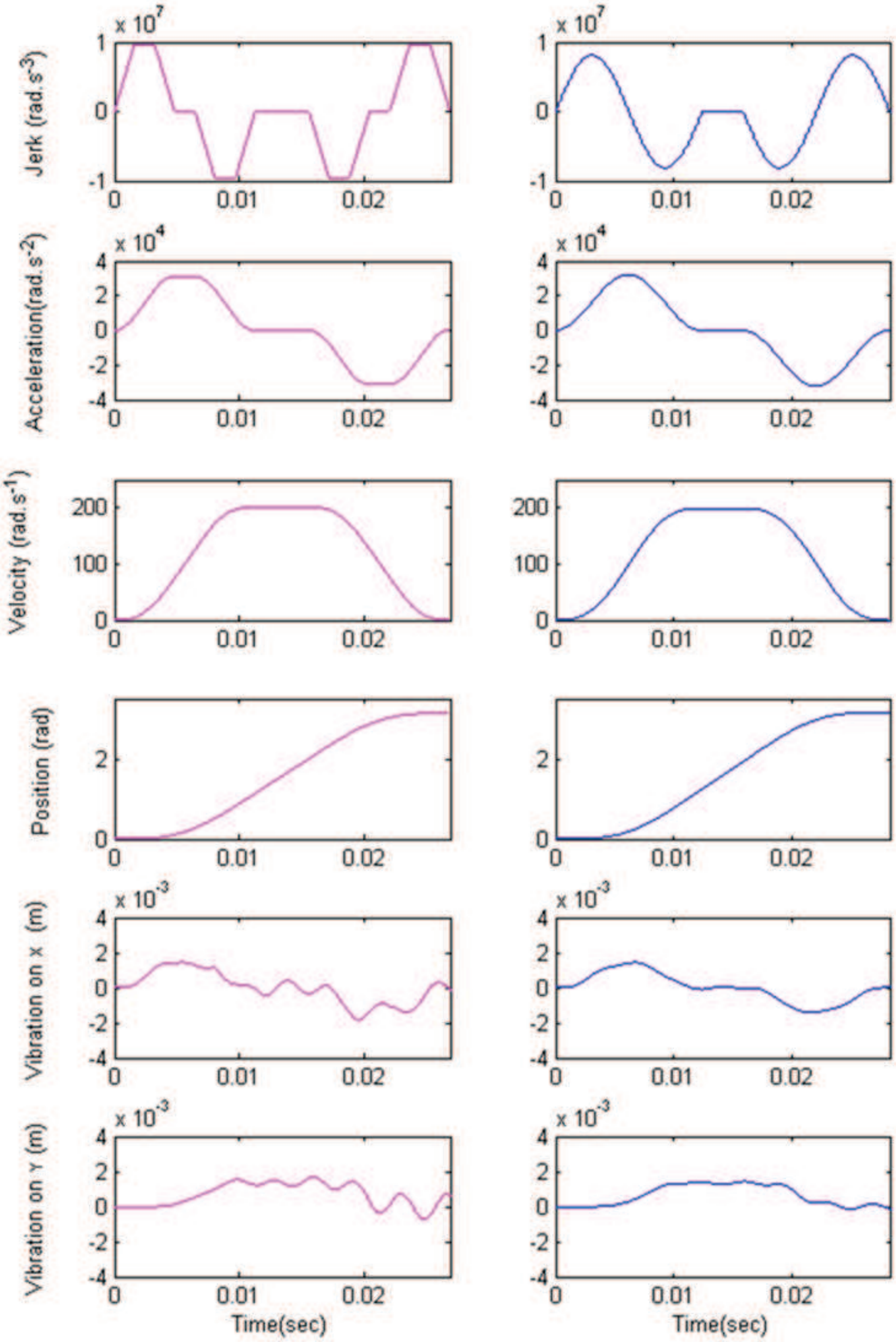

Figure 5.13: Plots of angular jerk, acceleration, speed and position profiles and resulting vibrations of the wire on x and y plans for 3^{rd} order s-curve profile(right) and trigonometric profile (left).

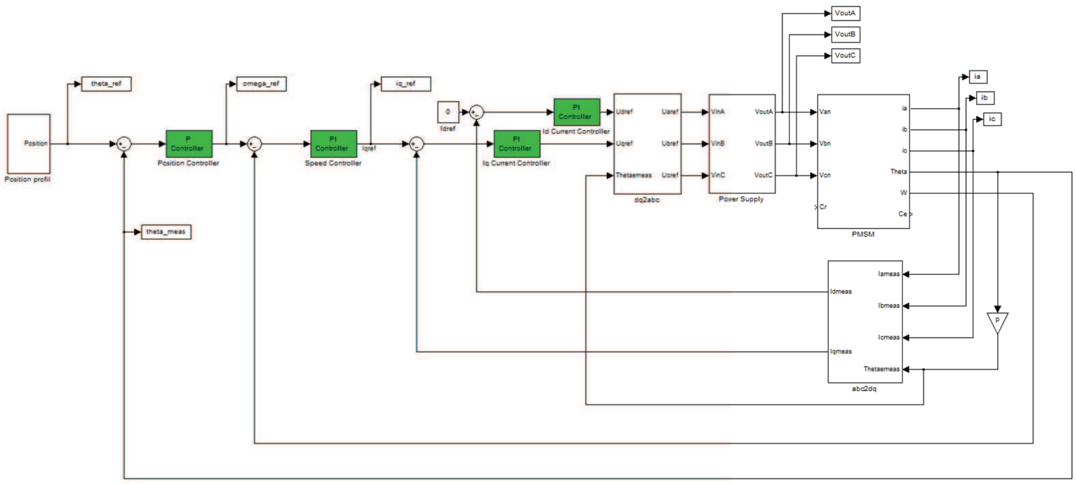

Figure 5.14: Simulink model of the actuator.

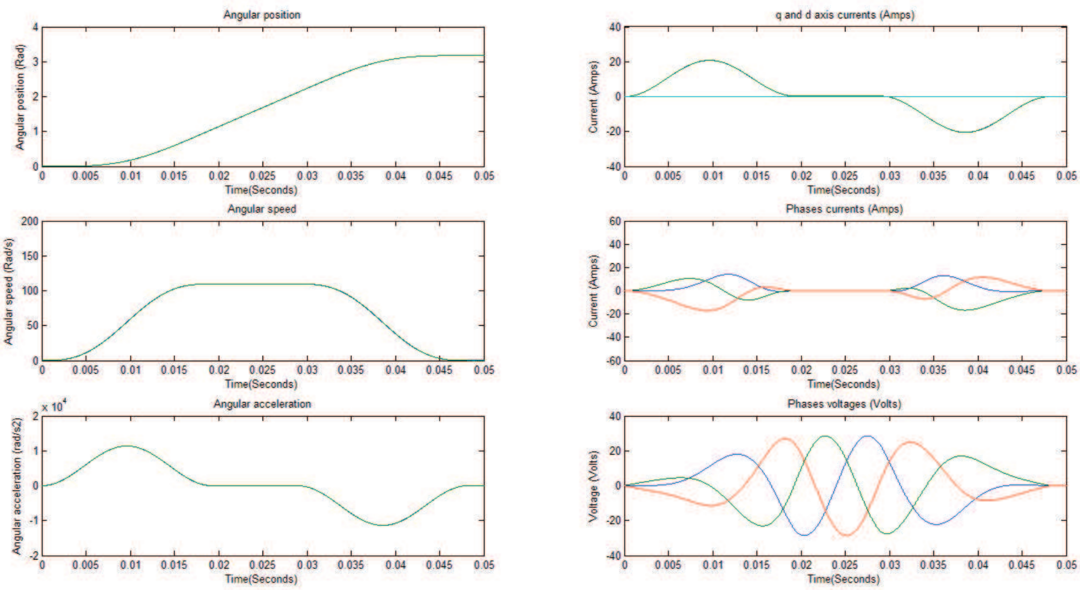

Figure 5.15: Simulation results for a maximum angular speed $\omega_{max} = 100\ rad \cdot s^{-1}$ including angular position, speed and acceleration profile and the quadratic and direct currents, phases currents and voltages.

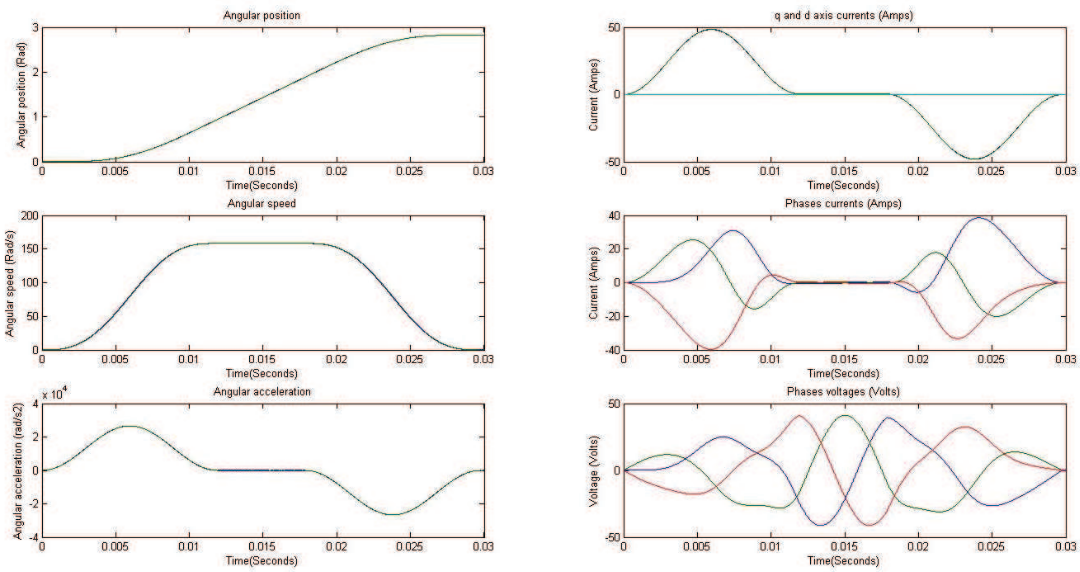

Figure 5.16: Simulation results for a maximum angular speed $\omega_{max} = 150\ rad \cdot s^{-1}$ including angular position, speed and acceleration profile and the quadratic and direct currents, phases currents and voltages.

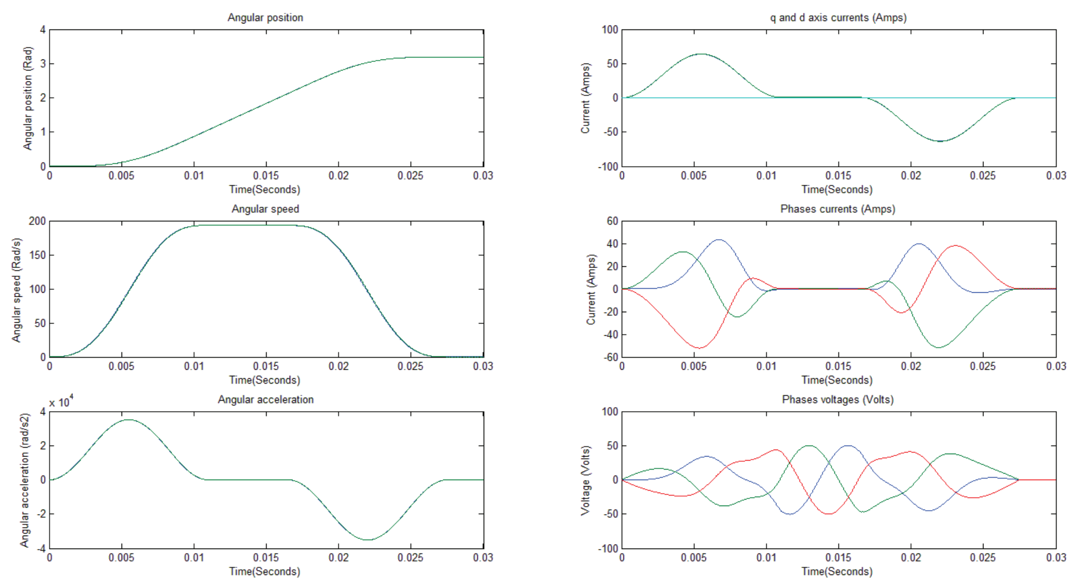

Figure 5.17: Simulation results for a maximum angular speed $\omega_{max} = 200\ rad \cdot s^{-1}$ including angular position, speed and acceleration profile and the quadratic and direct currents, phases currents and voltages.

6

Prototype

The last step of the design process of the WS actuator concerns the experimental realization of a prototype of this system. The aim is to validate the technological choices of the main components of the actuator which are the PMSM, the power supply and the proposed automatic control algorithm. This operation is done in a laboratory environment where the real environment of the system like the high temperature, vacuum and radiation are not considered. Then, this chapter focuses on the experimental test bench especially developed to check the validity of our choices previously exposed. First, all the elements of the setup are described through the presentation of their technical characteristics and the identification of their physical parameters used for modeling and control. The technical presentation consists in giving the practical approach adopted for the construction and installation of each one of these elements in the test bench while the identification concerns the computation of the physical parameters of the used models (resistor, inductor, back-EMF constant, rated and peak values of currents and voltages, total moment of inertia and load torques). Once all the models parameters identified, the control algorithm is simulated under Simulink software and implemented on the DSPACE device to see how the actuator behaves according to the expected functionalities. Then, the obtained experimental and simulation results are compared to each other in order to validate the design of the controller and the sizing of the actuator.

6.1 Introduction

During the elaboration of this thesis, an important part of time has been spent to design and construct an experimental test bench which allows to characterize and test the key components of the actuator and to develop and test the control strategy of the motor. The next sections expose the principal achievements done in this framework.

6.2 Test bench description

This test bench consists of 4 main parts as shown in Fig. 6.1 and Fig. 6.2:

- The drive test set-up contains the mechanical support and two electrical machines mounted on the same shaft: the PMSM (with vacuum barrier in its air-gap) and a DC motor which allows to load and drive the shaft. A position encoder, mounted on the rotating shaft, provides the high accuracy angular position. A resolver ensures the absolute angular position measurement for the PMSM drive.

- The power supply consists of a variable DC voltage source to feed the DC motor and a power converter designed and built specifically for the PMSM feeding. This power converter consists of a 3-phase linear inverter, a capacitor pack and a bipolar DC-bus produced from grid with 2 linear supplies. For control and study needs, a current and voltage measurement board has been built and integrated to the power converter.

- The resolver-to-digital converter (board) allows to convert analog signals provided by the resolver to a digital (16 bits) value of the angular position values.

- The control and supervision devices are ensured by the fast prototyping system (dSPACE 1103) associated to a PC.

All these component characteristics and the way in wich each of them contributes to the experimental test bench, are developed in the next section.

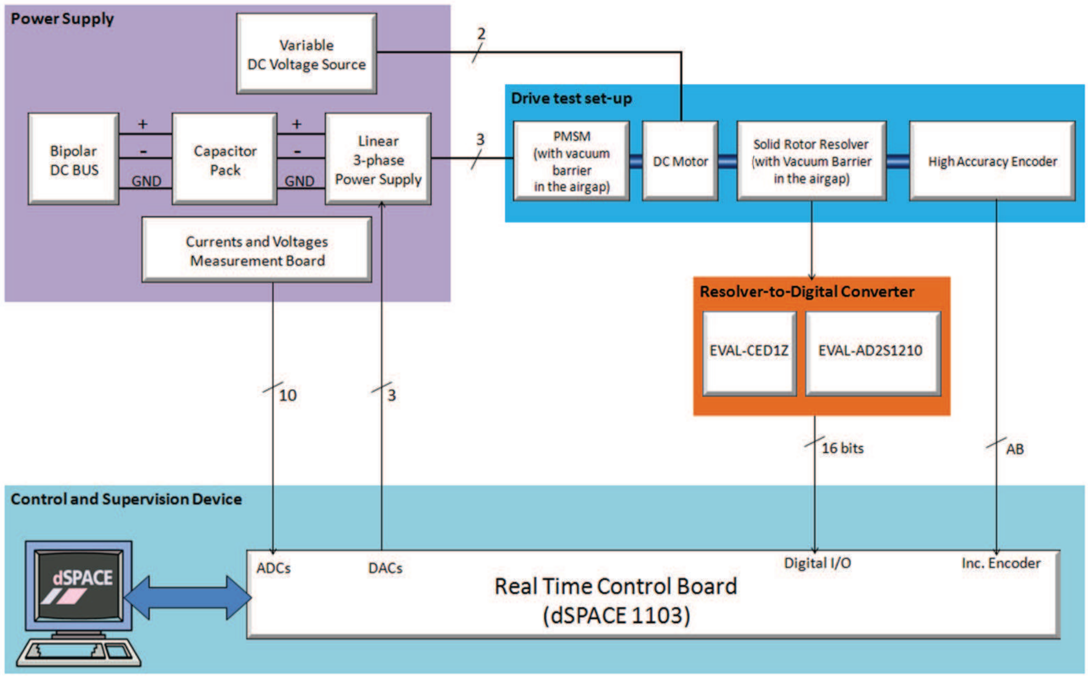

Figure 6.1: Experimental test bench schematic.

6.2.1 Drive test set-up

A frameless PMSM is mounted on a common shaft including a non-magnetic shielding cylinder in it air-gap, a DC motor, a high accuracy optical encoder and a solid resolver including a non-magnetic shielding cylinder in its air-gap (Fig. 6.3). The usage and the characteristics of each of these components are described below.

6.2.1.1 Friction torque measurement

The total friction torques of the drive test set-up is measured by rotating the shaft with the DC motor at different angular speeds and by measuring the current flowing in the DC motor. The current is directly proportional to the torque provided by the DC motor as

$$T_f = K_T.I_{dc} \tag{6.1}$$

where T_f is the friction torque, K_T is the torque constant and I_{dc} is the current flowing in the DC motor.

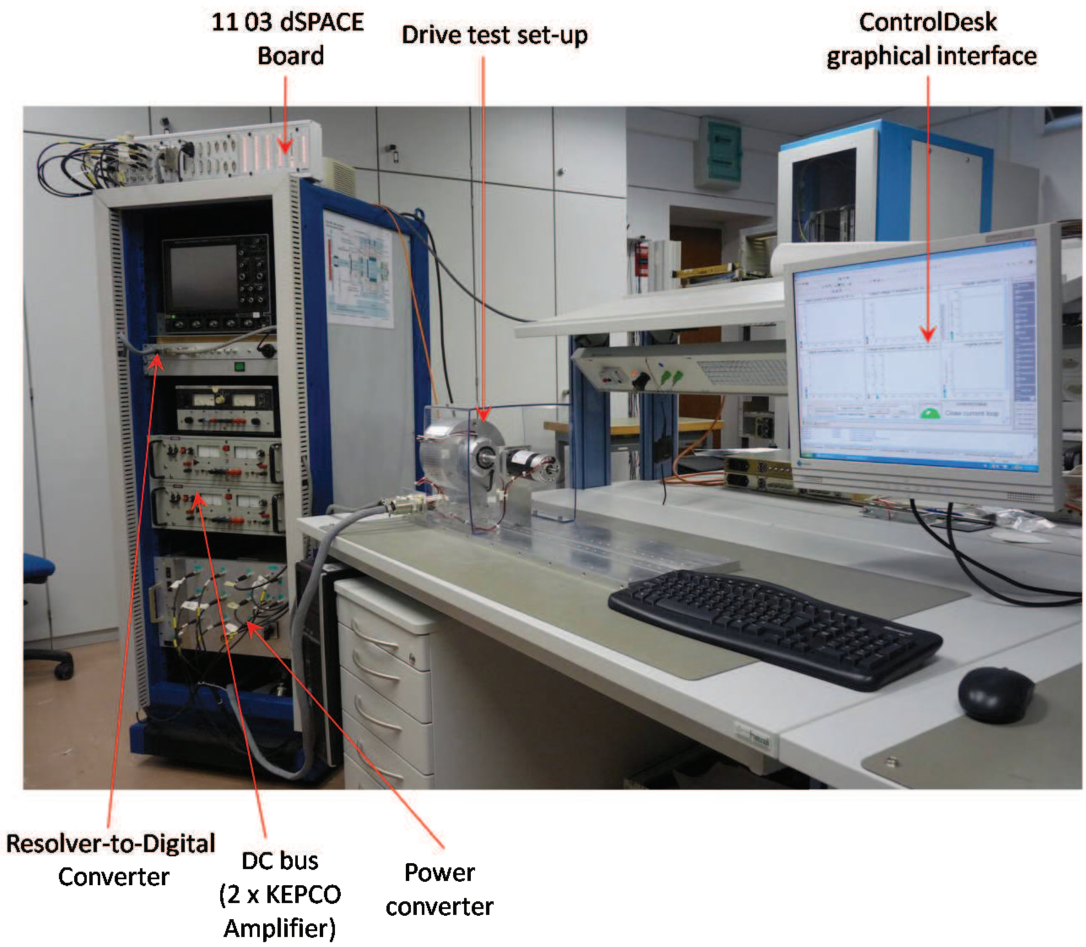

Figure 6.2: Experimental test bench picture.

The total friction torque is the sum of friction torque caused by the bearing of the DC motor, the encoder and the PMSM. Fig.6.4 summarizes the different experimental tests performed in order to evaluate the above-mentioned torques. The test allowing to determine the friction torque due to DC motor is shown in Configuration 5. Then, the same test has been done on the whole drive set-up (see Configuration 1) allowing to determine the total friction torque. By subtracting the friction torque of the Configuration 1 from the Configuration 5, the friction torque coming from the PMSM and the encoder has been calculated (6.4, Configuration 2). Then, in the Configuration 3, the same test has been done without the encoder (the angular position has been measured by an optical tachometer) and by subtracting the friction torque due to DC motor from

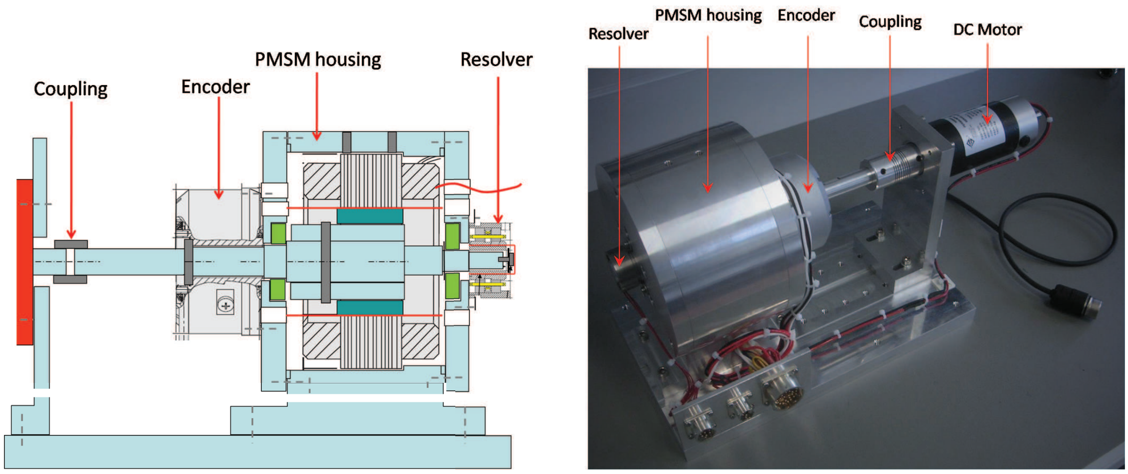

(a) (b)

Figure 6.3: (a) Drive test set-up mechanical design schematic (b) Drive test set-up picture.

the friction torque of the PMSM, bearings has been determinated (6.4, Configuration 4).

6.2.1.2 PMSM electromagnetic parameters

Parker K500150 frameless PMSM has been selected. These kinds of motors are supplied in two independent parts: a 3-phase stator (Fig. 6.5, a) and a rotor (Fig. 6.5, b) with permanent magnets mounted on the surface.

The stator is directly integrated into the foreseen aluminium alloy (AW 6082) housing. It is solidly fixed with 3 series of 2 screws equidistant of 120^o to each other allowing to adjust the stator position. Two covers for each side of the stator housing allow to fix horizontally the stator and to support the bearings. Series of holes have been foreseen for the motor cooling and to have a view on the rotor.

The rotor core is made of standard magnetic steel which can be made vacuum compatible. Samarium cobalt alloy has been chosen as the adequate magnetic material for the rotor, instead of standard neodymium which is less resistive to high temperature (Neodymium Curie temperature is about 320^oC and 800^oC for Sm-Co. The standard glued fixation of the magnet on the rotor core has been replaced by a designed mechanical fixation in order to match the vacuum requirements. The air-gap thickness

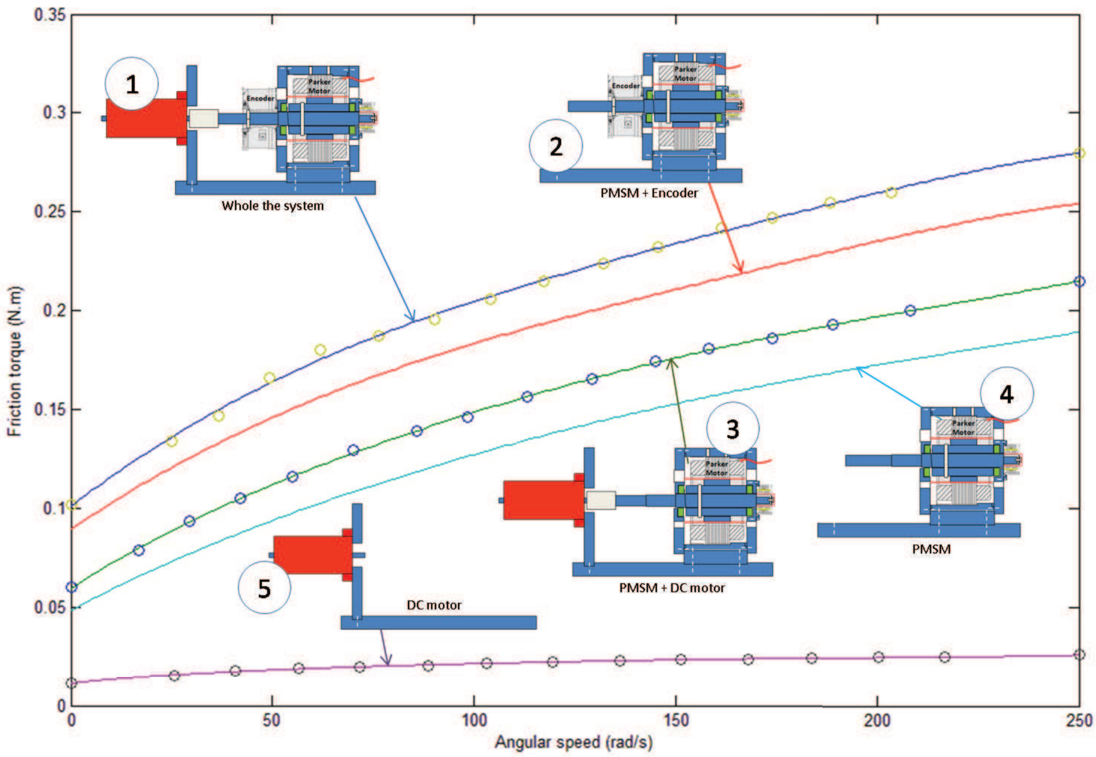

Figure 6.4: Friction torques of the drive test set-up for different configuration.

between the rotor and the stator is of 0.8 mm in which a 0.3 mm thickness vacuum barrier is introduced (Fig. 6.5, c).

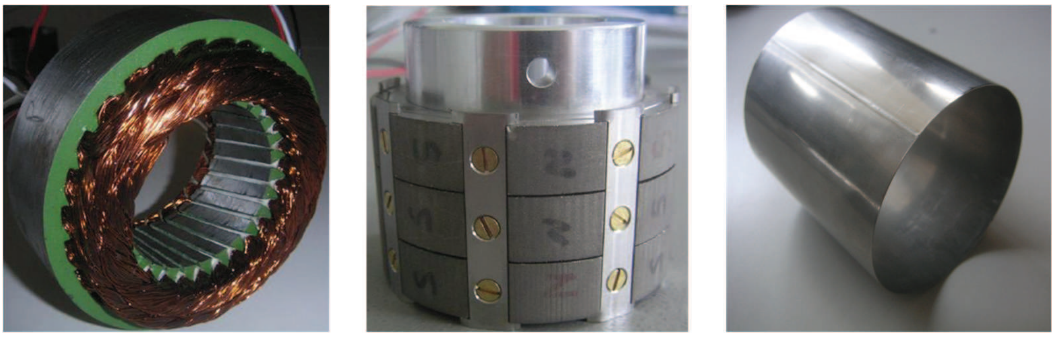

(a) (b) (c)

Figure 6.5: (a) 3-phase stator. (b) Rotor with permanent magnets mounted and fixed mechanically on the surface. (c) Vacuum barrier cylinder.

The very attractive forces of the magnets imply a special care during the mounting

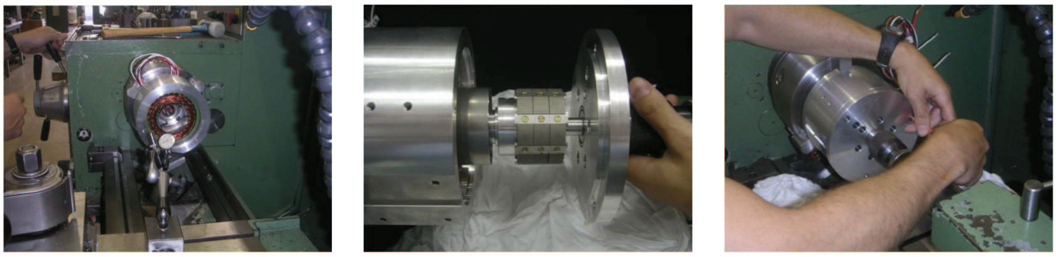

(1) (2) (3)

Figure 6.6: Safe introduction of the rotor in the stator procedure: (1) Insert the stator into the housing cavity. Secure the stator to the housing by screwing series of 6 screws. Assemble the first cover including bearings with the housing/stator assembly. Mount the cover/housing/stator assembly into the spindle. Control the concentricity of the assembly. (2) Mount the shaft, rotor and the second cover (including bearings) together. Then, mount this assembly into the tailstock of the lathe. Insert the vacuum barrier into the stator. Guide assembly into the final position within the armature assembly by turning slowly the rotary knob of the lathe. (3) Screw and close the housing.

of the rotor into the stator. A procedure has been elaborated based on a mechanical lathe allowing a safe mounting of the rotor (Fig. 6.6).

a) Resistances and inductances measurement

The phase resistances have been measured using a precision ohmmeter (Fig. 6.7, a). Naturally, the temperature of the winding should be taken into account. The line-line inductances have been measured at several rotor positions with a RLC meter (Fig. 6.7, b and Fig. 6.8). However, RLC meter uses a test frequency of 1 kHz and very low currents, and the indicated inductance may differ from the correct values which corresponds to a lower frequency and much higher currents. The reasons for this difference are the variable permeability of the core and the effect of induced current in it and other parts of the motor.

In a 3-phase motor with winding connected in star configuration, the measured line-line inductance is given by

$$L_{LL} = L_1 + L_2 - 2L_{12} = 2(L - M) \tag{6.2}$$

where $L_1 = L_2 = L$ is the phase self-inductance and $L_{12} = M$ is the mutual inductance between phases. The resistance $R_{12} = 2R$ is twice the phase resistance.

b) Back-EMF measurement

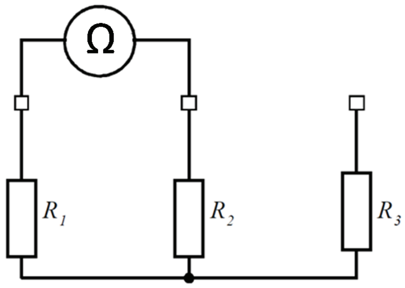

(a)

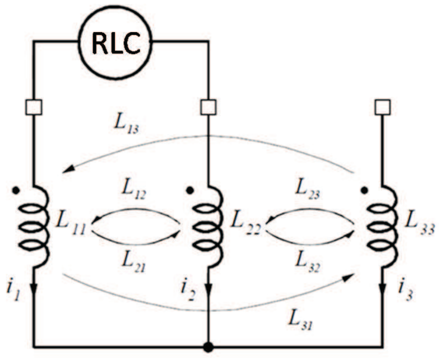

(b)

Figure 6.7: (a) Measurement of the phase resistances using an ohmmeter (b) Measurement of inductances using a RLCmeter.

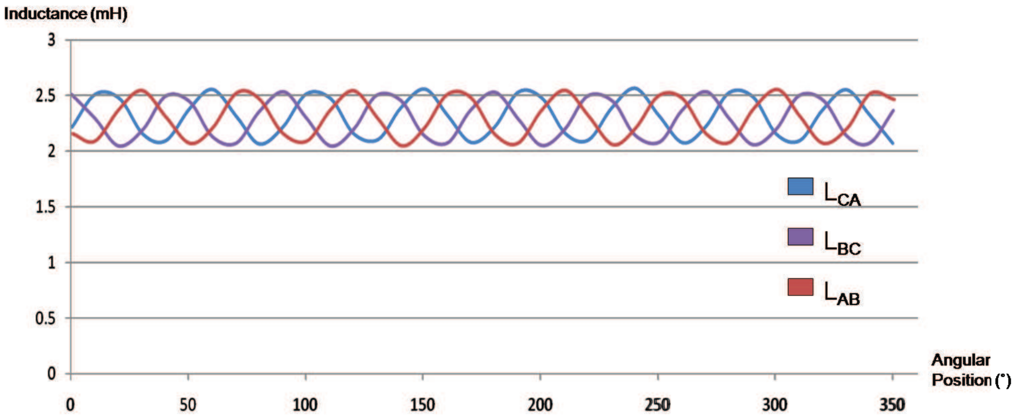

Figure 6.8: Measurement of the line-line inductances versus angular position of the rotor.

The procedure to measure the back-EMF voltages is possible by driving the PMSM as a generator at a given speed with the DC motor and measure the open-circuit EMF. With no current flowing, the voltage drops are zero and k_E can be measured directly. To keep the same unit as used in the datasheet, we measure k_E in units of "Volts per radian per second". Fig. 6.9 shows the back-EMF voltages measurement at different angular speeds of rotation.

The Table 6.1 gives a summary of measured parameters of the motor.

c) Torque due to vacuum barrier measurement

Examining Fig. 6.10, it can be concluded that the impact of the vacuum barrier can

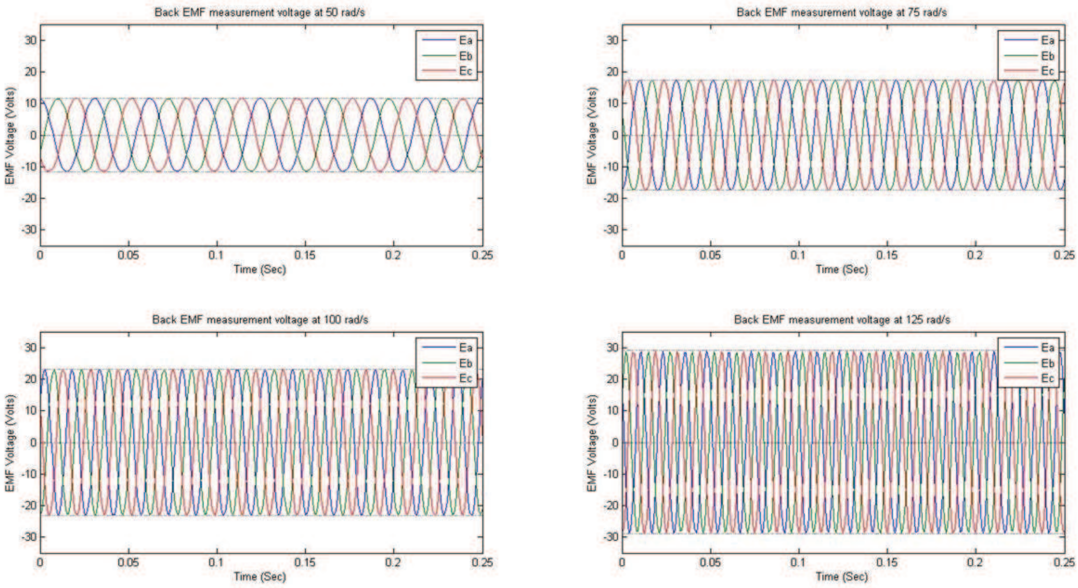

Figure 6.9: Back-EMF voltages measurement at different angular speed of rotation.

be modeled by an additional load torque strongly related to the rotational speed of the PMSM. Fig. 6.11 illustrates the vacuum resistant torque theoretically estimated from the computations of the Eddy current power losses performed in Chapter 3, is in . It can be noticed that the waveform of this curve is linear while the measured one is close to a quadratic shape. It also clearly appears that the magnitudes of the estimated resistant vacuum torque are higher than the measured ones for the whole wide speed variation of the WS, i.e. from 0 to 200 $rad \cdot s^{-1}$. For example, for the speed of 200 $rad \cdot s^{-1}$, the measured torque is about 0.18 Nm, while the estimated one is equal to 0.24 Nm. Moreover, in the real environment conditions where the temperature is higher, the conductivity of the 360LN16 stainless steel is lower, entailing a lower resistant torque. According to this result, the sizing of the vacuum barrier can be validated.

6.2.1.3 Encoder description

A HEIDENHAIN RON225 high accuracy incremental encoder (Fig. 6.12) has been mounted on the shaft of the test set-up. This angular position sensor allows to give a position reference for the calibration of the resolver and to characterize the optical fiber test set-up. It consists of a set of pairs of phototransistors and a collimated light source, used in conjunction with a glass encoder disc. The pattern of slits on the

Bemf(Volts/kRPM)	A-B	38.4
	B-C	38.4
	C-A	38.4
Resistance (Ohms)	A-B	0.472
	B-C	0.469
	C-A	0.469
Inductance (mH)	A-B	2.30
	B-C	2.29
	C-A	2.27

Table 6.1: Measured parameters

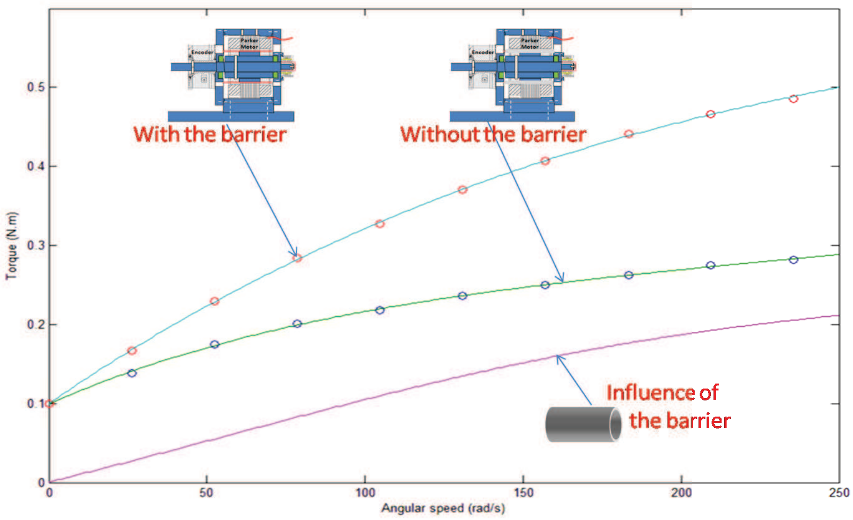

Figure 6.10: Torque measurement with and without the vacuum chamber according to the angular speed.

disc defines the frequency and waveform of the pulse train which are produced by the phototransistors. This pulse train contains two square signals in quadrature to each other. The encoder has been directly connected to the Incremental Encoder input of dSPACE board which allows to convert these signals into readable values . Table 6.2 sums up the RON225 incremental encoder parameters.

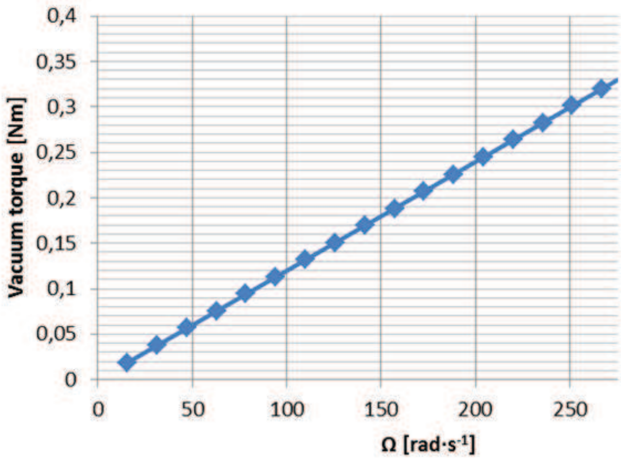

Figure 6.11: Theoretical estimation of vacuum resistant torque according to the angular speed.

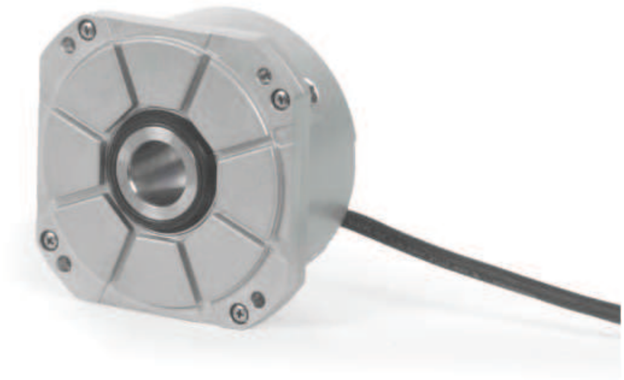

Figure 6.12: Picture of the RON225.

6.2.1.4 Solid rotor resolver description

The operating principle of the solid rotor resolver has been developed previously in the chapter. For the drive test set-up, we selected series RO3620 with a 36mm stator outer diameter and a 20mm inner diameter. The maximum temperature which it withstands reaches $230^o C$ because of its Kapton insulation.It is rated with an absolute accuracy of ±60 arc-minutes. The rotor is mounted on the shaft outside the motor housing (Fig. 6.13). The resolver stator is fixed on the side of the test bench concentric to the

Parameters	Values
Incremental signals	TTL x 2
Line count	9 000
Integrated interpolation	2-fold
Output signals/revolution	18000
Recommended measuring step for position measurement	0.005^o
System accuracy	5 arcseconds
Mechanical permitted speed	3000 min^{-1}
Moment of inertia of rotor	73.10^6 kgm^2

Table 6.2: RON 225 incremental angular encoder parameters

rotor. A membrane is fixed against the inside of the stator allowing to test its effect on the output signal and on the accuracy measurement.

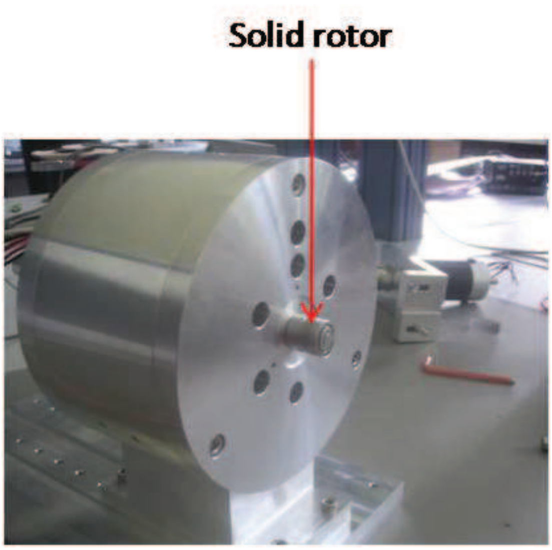

(a)

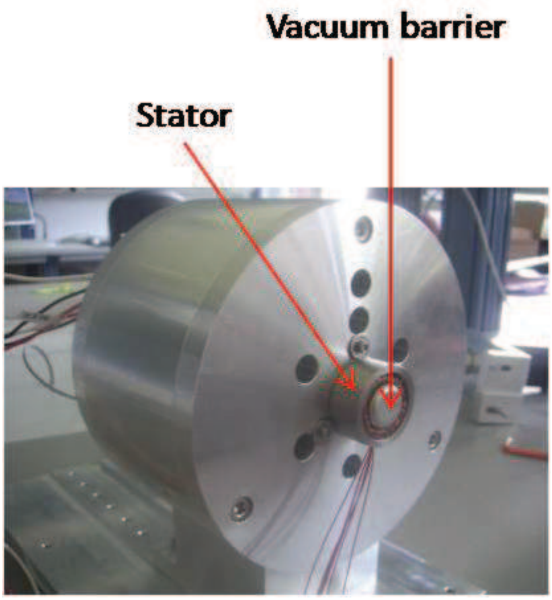

(b)

Figure 6.13: (a) Resolver fixed in the end of the shaft. The circular recess around the rotor guarantees the concentricity of the stator. (b) Stator fixed in the test-bench and the vacuum barrier.

The solid rotor resolver provides an absolute angular position measurement used for speed servo loops. However, the demand in terms of accuracy is higher than the rated accuracy of ± 60 *arcminutes* provided by the resolver. By comparing the position measurement of the resolver and the high accuracy encoder, we have confirmed that the inaccuracy is predominantly of systematic nature and can be compensated significantly to obtain an acceptable accuracy. The measurement was repeated several times and the statistical error has been recorded in the same table (Fig. 6.14, top). The maximum amplitude of the error is in concordance with the inaccuracy quoted by the manufacturer (± 60 *arcminutes*). The error compensation information has been stored in a lookup table which corrects the acquisition on-line. The procedure has improved the accuracy of the resolver from ± 60 *arcminutes* to ± 6 *arcminutes* which satisfies the specification for the motor control.

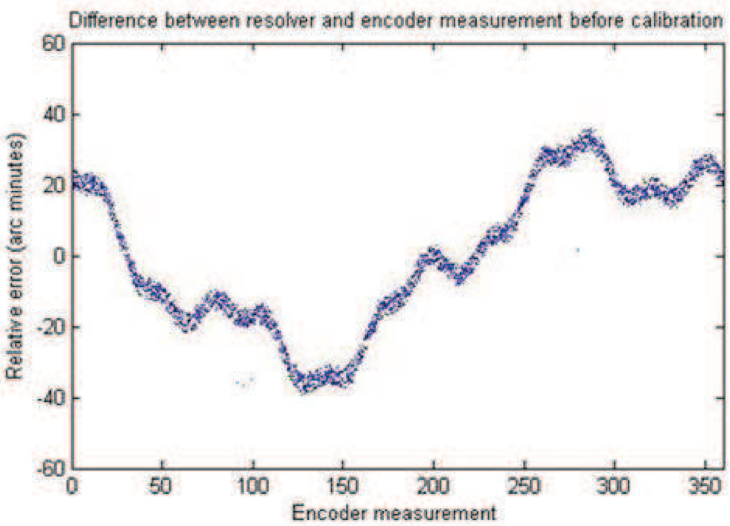

Figure 6.14: Difference between encoder and resolver measurement versus encoder measurement before calibration.

6.2.1.5 DC motor

The 1050LT NEMA 23 DC motor has been selected and is used to drive the PMSM in generator mode and to apply a load torque to the PMSM when it oporates in

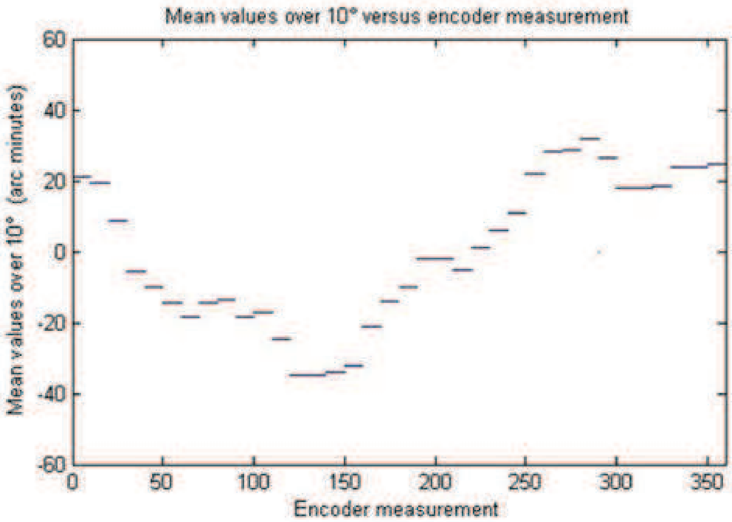

Figure 6.15: Difference between encoder and resolver measurement versus encoder measurement. An average is done every 10^o.

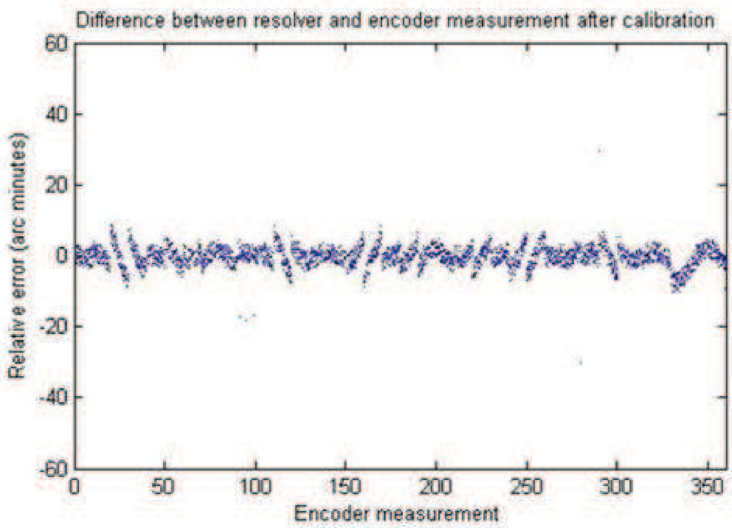

Figure 6.16: Difference between encoder and resolver measurement versus encoder measurement after calibration.

motor mode. This motor is supplied externally by a DC voltage source. The physical parameters of this motor are given in Table 6.3.

Parameters	Values
Stall Torque, Continuous	0.35 Nm
Peak Torque	2.52 Nm
Maximum Speed	6000 rpm
Continuous Stall Current	5.4 Amps
Torque Constant	0.07 Nm/Amp
BEMF Constant	6.9 V/krpm

Table 6.3: Brush, rotary DC servomotors parameters

Figure 6.17: Brush, Rotary DC Servomotors.

6.2.2 Power supply

To supply the PMSM, a linear 3-phase power supply providing a 3-phase voltage outputs driven through 3 BNC inputs has been designed and built (Fig. 6.19 and Fig. 6.18). The power supply consists of

- an Energy Storage Unit allowing to compensate the power peaks during the acceleration/deceleration phases,
- 3 linear power amplifiers allowing to provide the 3-phase currents of the PMSM,
- a measurement board of currents and voltages,
- a bipolar DC produced by 2 linear power supplies which are connected to the grid.

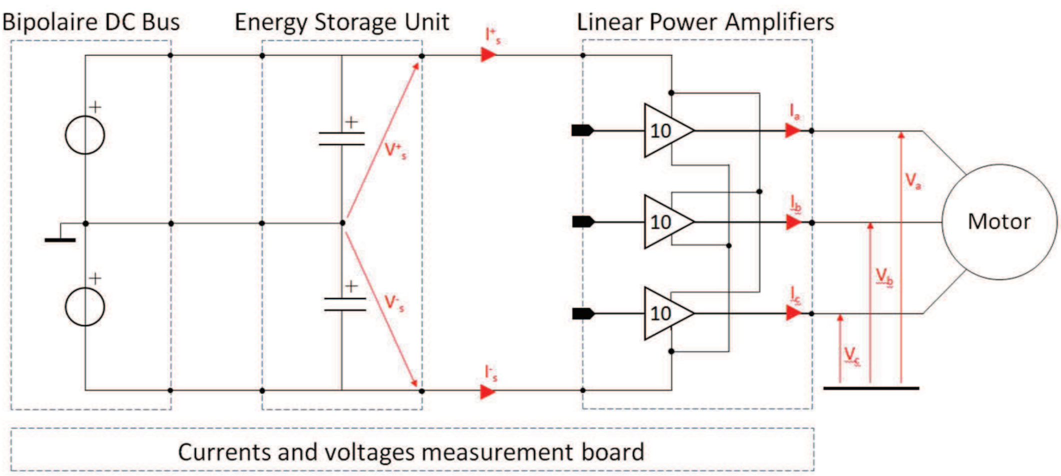

Figure 6.18: Simplified schematic of built power supply.

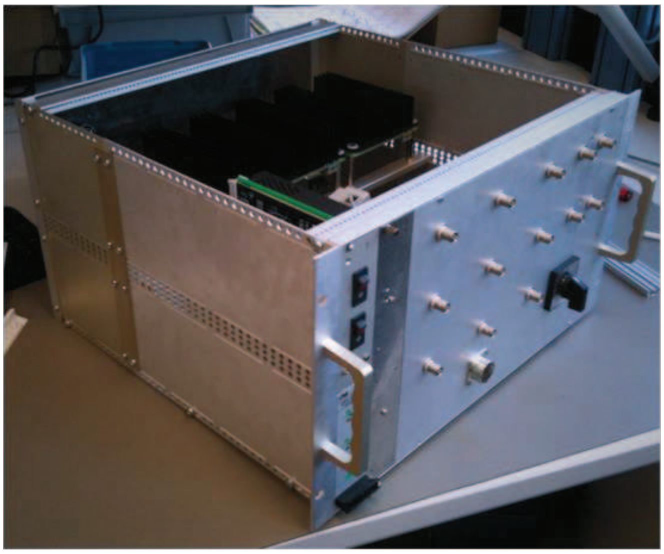

Figure 6.19: Built power supply picture.

6.2.2.1 Bipolar DC Bus

The bipolar DC bus allows to supply the power amplifiers with $\pm$ $100V$. It is based on two Kepco linear amplifiers driven by an external dc source.

6.2.2.2 Energy Storage Unit (ESU)

Energy storage unit (Fig. 6.20, a) allows to balance the difference of power between the peak current requested by the motor during the acceleration and deceleration phase and the current provided by the bipolar DC bus. The ESU is based on 2 aluminum electrolytic capacitors (2x22 mF). Two LEDs indicate when capacitors are charged (not represented on the simplified schematic). An interrupter allows to discharge energy stored in two high power resistors (100Ω, 100W).

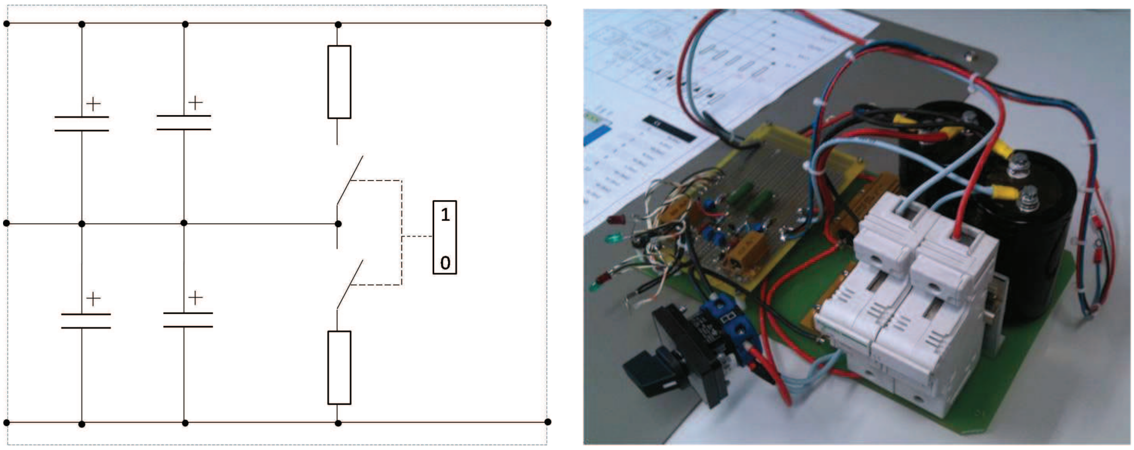

(a) (b)

Figure 6.20: (a) Simplified diagram of the ESU. (b) Picture of the ESU.

6.2.2.3 Linear power amplifiers

A linear 3-phase power supply is based on 3 APEX PA52 power amplifier mounted on their evaluation boards. The evaluation board provides a flexible platform for the evaluation of the component. Only the critical connections for the power supply of the amplifier are pre-wired. Feedback resistors have been calculated and mounted to obtain a non inverting configuration with a gain of 10.

a) Output stage protection

Sudden change in current flow in an inductive load will cause large voltage flyback spikes which can destroy the output stage of the amplifier. High speed (inferior than 100ns) recovery diodes should be used from the output of the op amps to the supply. Power supply must look like a true low impedance source. Otherwise, the flyback energy, will merely result in a voltage spike at the supply pin of the linear amplifiers.

b) Power supply overvoltage protection

The amplifier should be not stressed beyond its maximum supply rating voltage. Over voltage conditions can be protected against by using zener diodes from the ampli-

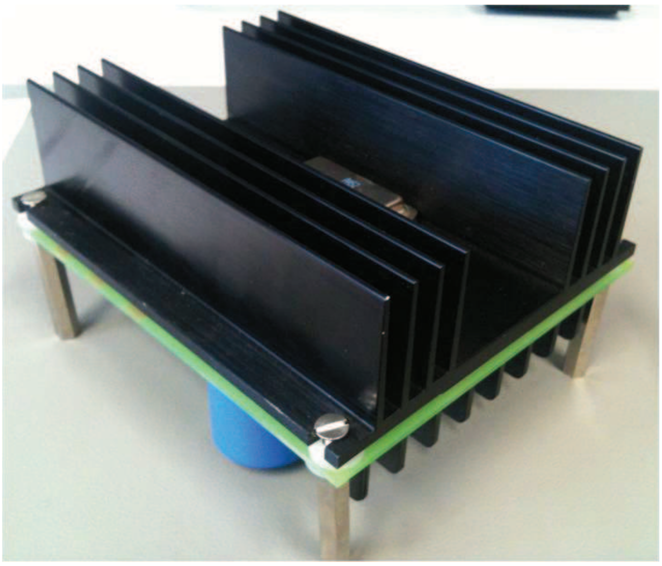

Figure 6.21: Linear amplifier mounted on its evaluation board.

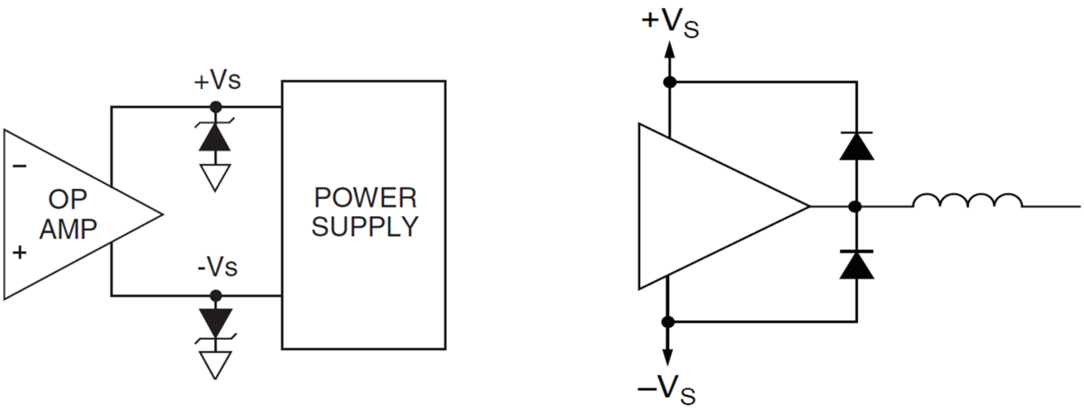

(a) (b)

Figure 6.22: (a) Output stage protection protecting against voltage flyback spikes (b) Power supply overvoltage protection.

fier supply pins to ground. The rating of these zener diodes is larger than the maximum supply voltage expected, but less than the breakdown voltage of the linear amplifiers.

c) Offset compensation

As the impedances of motor windings are very low, a direct connection of the amplifier will cause a large current even when its offset output voltage is very small.

A compensation of the offset is needed. It is possible to compensate these offsets by software applying the right values on the DAC. However, in order to provide more reliability to the system during the development phase, we prefer to use hardware circuits to compensate the offsets. The offset compensation circuit is shown in Fig. 6.23. It consists of a simple potentiometer and resistors connected to a +15 V dc source. Resistance values have been calculated to allow a large compensation range (-5V to +5V) while the gain is not modified (Fig. 6.24).

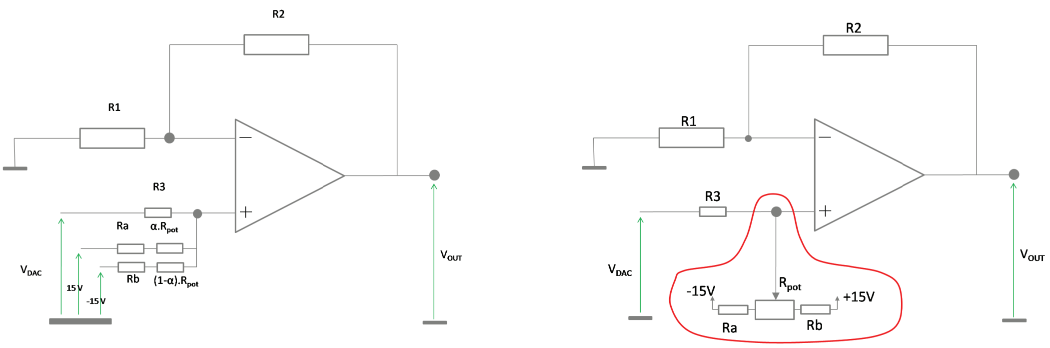

(a) (b)

Figure 6.23: (a) Offset compensation circuit (b) Equivalent offset compensation circuit.

$$V_{out}(V_{DAC}) = (1 + \frac{R_1}{R_1}).\frac{\frac{-15}{R_{pot}.(1-\alpha)+R_b} + \frac{15}{R_{pot}.\alpha+R_a} + \frac{V_{DAC}}{R_3}}{\frac{1}{R_{pot}.(1-\alpha)+R_b} + \frac{1}{R_{pot}.\alpha+R_a} + \frac{1}{R_3}} \tag{6.3}$$

$$Offset(\alpha) = (1 + \frac{R_1}{R_1}).\frac{\frac{-15}{R_{pot}.(1-\alpha)+R_b} + \frac{15}{R_{pot}.\alpha+R_a}}{\frac{1}{R_{pot}.(1-\alpha)+R_b} + \frac{1}{R_{pot}.\alpha+R_a} + \frac{1}{R_3}} \tag{6.4}$$

$$Gain(\alpha) = (1 + \frac{R_1}{R_1}).\frac{\frac{1}{R_3}}{\frac{1}{R_{pot}.(1-\alpha)+R_b} + \frac{1}{R_{pot}.\alpha+R_a} + \frac{1}{R_3}} \tag{6.5}$$

6.2.2.4 Currents and voltages measurement board

For the measurement of motor supply current, we used Hall effect sensors. The output signals of each current sensors are sampled and acquired by the parallel ADCs of the dSPACE board. The voltage measurements are done by the Hall effect sensors LV 50-P. The output signals are also sampled and acquired by the ADCs of the dSPACE

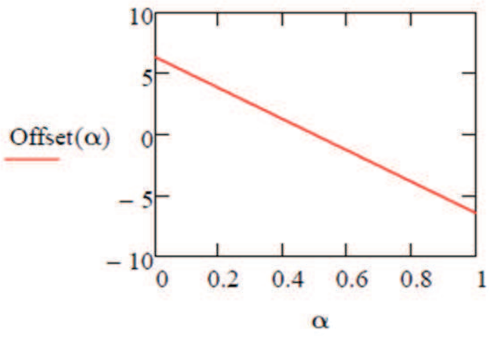

(a)

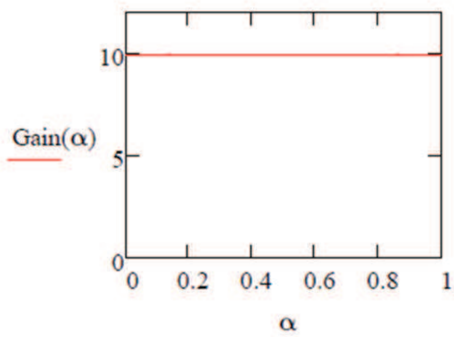

(b)

Figure 6.24: (a) Offset compensation voltage according to the potentiometer position. (b) Influence of the offset compensation to the power amplifier gains according to the potentiometer position.

board. Fig. 6.25 shows the picture of the designed and built currents and voltages measurement board.

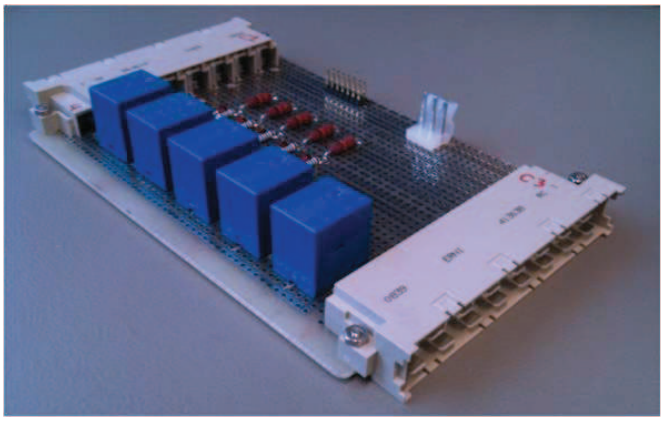

Figure 6.25: Currents and voltage measurement board picture.

6.2.3 Resolver-to-Digital Converter (RDC)

6.2.4 Control and supervision device

The drive test set-up is controlled by a rapid prototyping system which is a computer system that allows to develop software for embeded calculator or control elements of mechatronics systems. The control of the system has been implemented using the dSPACE fast prototyping tool. The advantage of the dSPACE tool is to use Matlab/Simulink support to design the system and use RTI (Real Time Interface) tool to export the application on a control system based on real-time microprocessor (PowerPC) and DSP (Fig. 6.26, a). This board is connected to the PCI slot of a personal computer and a remote box (Fig. 6.26, b) which allows to access to the inputs and outputs. Supervision, diagnostics and parameter modification are using the software ControlDesk that creates a graphical user interface (GUI) on a PC for the user. Fig. 6.28 shows an example of the developed control desk interfaces.

The rapid prototyping tool used in our application is the DS1103 PPC Controller Board. Its internal architecture is shown in Fig. 6.27 while its main features are:

- Processor PowerPC (PPC) cadenced at 750 GHz
  - 96 Mo Communication SDRAM;
  - ADC, 20 channels, 16-bit;
  - DAC, 8 channels, 16-bit;
  - Incremental Encoder, 7 channels;
  - Digital I/O, 32 channels;
  - Serial Interface RS232/RS422;
  - CAN Interface;
- Slave TMS320F204 DSP
  - PWM, 1 x 3-Phase, 4 x 1-Phase;
  - 4 Capture Inputs;
  - Analog Input, 16 channels, 10-bit;
  - Serial Communication Interface;
  - Digital I/O, 18-bit;

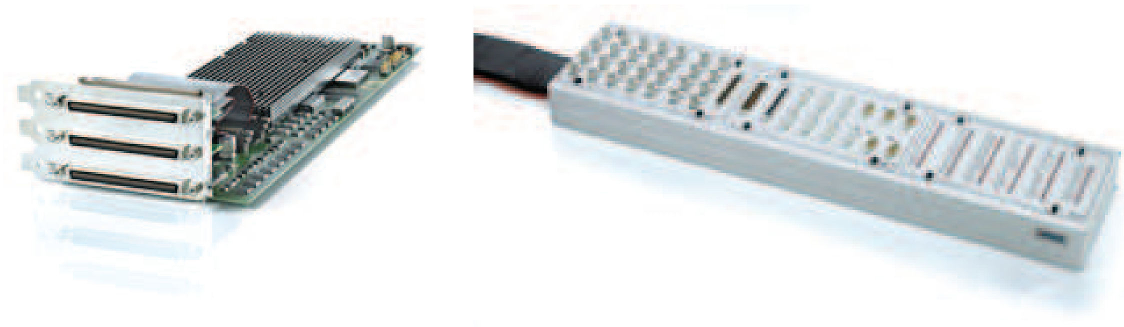

(a) (b)

Figure 6.26: a) DS1103 PPC Controller Board picture. b) CP1103 Connector and LED panel.

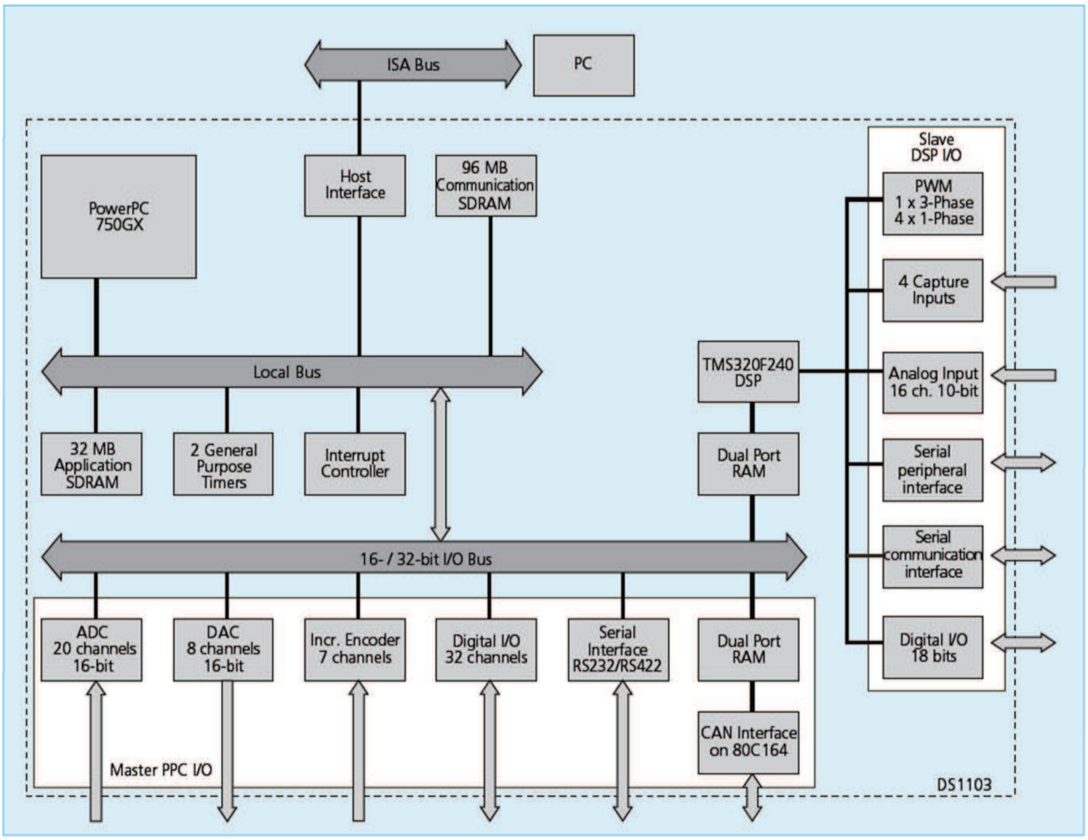

Figure 6.27: dSPACE 1103 board architecture.

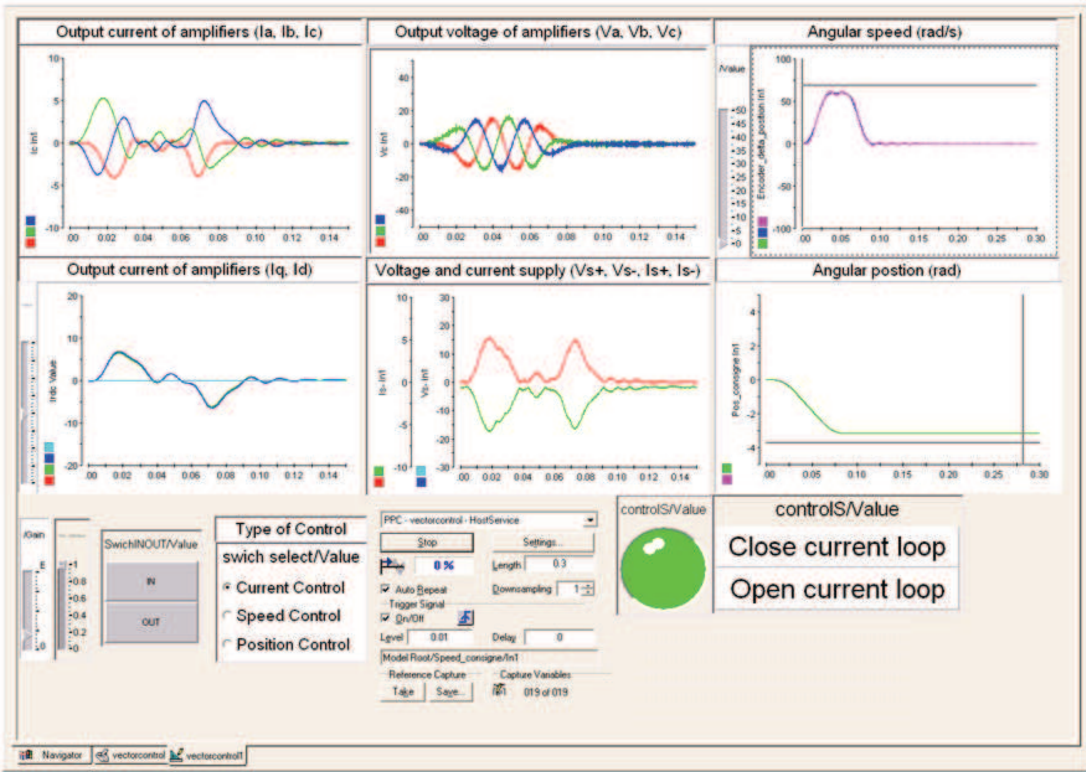

Figure 6.28: Example of the developed control desk interfaces.

6.3 Validation exprimental tests

In this section, we present the main experimental results obtained with the help of the real time interface system dSPACE. The used program is the one for the simulations of chapter 5 in which the physical parameters are those measured experimentally in the present chapter. The aim is to compare the experimental measurements to the simulation results in order to raise enough information to validate our design by its two aspects: the Wire Scanner drive (including principally of the PMSM the control algorithm) and the power supply consisting principally of the 3-phase linear inverter. For these tests, we have voluntarily limited the maximum speed of the PMSM to 150 $rad \cdot s^{-1}$ in order to avoid the destruction risk of the linear amplifiers which are very fragile and expensive.

6.3.1 Validation of the Wire Scanner drive

The identified parameters have been used to compute the gains of different regulators. These gains have been used as starting values in the dSPACE program and have been adjusted so that the system response is the best as possible. Thus, the obtained values are:

- i_d current PI regulator: $K_p = 2$, $T_i = 0.01$.
- i_q current PI regulator: $K_p = 2$, $T_i = 0.01$.
- Speed PI regulator: $K_p = 0.5$, $T_i = 0.1$.
- Position P regulator: $K_p = 5000$

Two cases have been considered according to the maximum value of the speed reference: $\omega_{max} = 150\ rad.s^{-1}$ and $\omega_{max} = 100\ rad.s^{-1}$.

6.3.1.1 First test case

For these tests a position profile is defined so that the PMSM's rotor moves from 0 to π in about 40 ms. In the same time interval, the angular speed of the rotor has to reach maximum value $\omega_{max} = 150\ rad.s^{-1}$ in the first 15 ms, then to stay at this value during about 10 ms before returning to zero in 15 ms. Fig. 6.29 and 6.30 show respectively the angular position and speed of the PMSM. The curves in blue present the references while the ones in green present the measured magnitudes. The simulation and experimental plots are presented respectively in the left and in the right sides of these figures. Examining these figures, we can say that in both simulation and experimental results, the measured magnitudes follow well their references despite some small errors that remain acceptable for our application. Comparing the experimental and simulation results to each other, we notice that the angular positions are almost the same. However, some oscillations are observed on the experimental speed in the middle and at the end of the speed travel. This difference may be interpreted by the fact that the oscillations of the cyclic inductance have not been taken into account in our simulations. That said, it may be relatively easy to include these effects by adopting $Ld \neq Lq$ in the $d-q$ model of the PMSM.

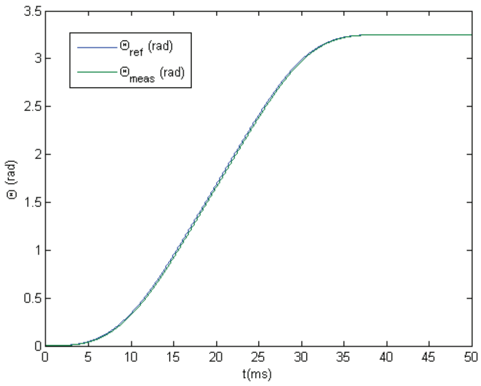

(a)

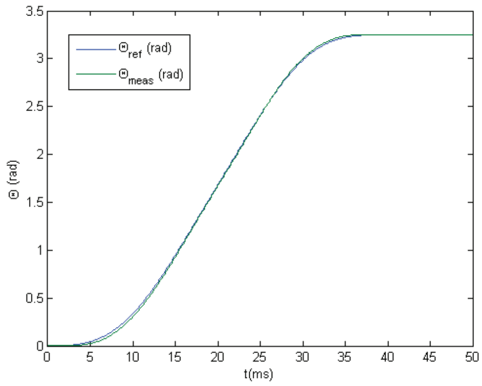

(b)

Figure 6.29: (a) Angular position for 150 $rad.s^{-1}$ scan (simulation) (b) Angular position for 150 $rad.s^{-1}$ scan (experimental).

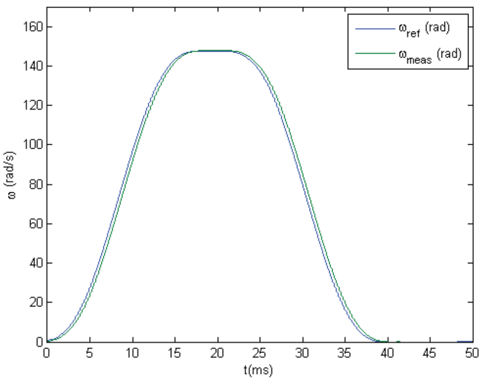

(a)

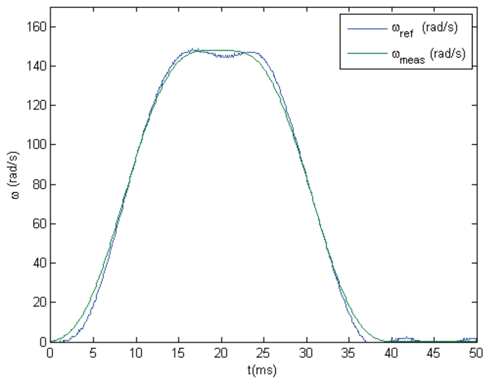

(b)

Figure 6.30: (a) Angular speed for 150 $rad.s^{-1}$ scan (simulation) (b) Angular speed for 150 $rad.s^{-1}$ scan (experimental).

The Fig. 6.31 shows the simulation and experimental waveforms of the PMSM direct and quadratic currents, i.e. i_d and i_q respectively. The direct current reference, set to 0 during all the functioning time, is quite well followed by the measured direct current on which we observe a light overshoot in the middle of functioning time interval. These remarks are valid for both the simulation and the experimental results. The measured quadratic current (picture of the electromagnetic torque) follows well the reference one meaning some errors and oscillations observed notably on the experimental results.

These oscillations are certainly due in part to the existing harmonics at the cyclic inductance of the machine which were not taken into account in our simulations.

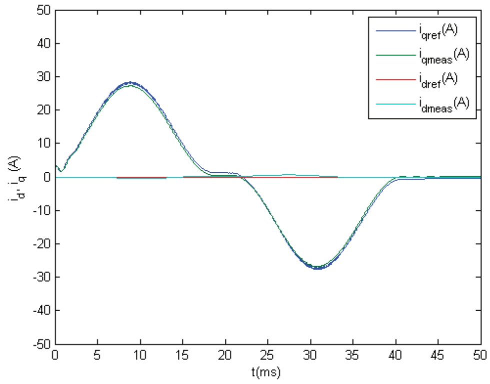

(a)

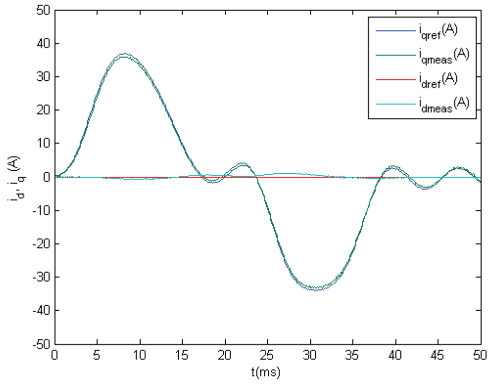

(b)

Figure 6.31: (a) i_q and i_d for 150 $rad.s^{-1}$ scan (simulation) (b) i_q and i_d for 150 $rad.s^{-1}$ scan (experimental).

Fig. 6.32 and 6.33 show the measured simulation and experimental waveforms of the PMSM 3-phase currents and voltages respectively. The simulation and the experimental results are close to each other in their global shape and their peak values. However, we notice more oscillations in the experimental measurements which are probably due in part to the existing harmonics at the cyclic inductance of the machine.

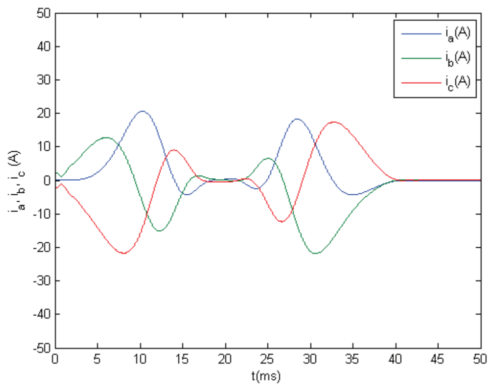

(a)

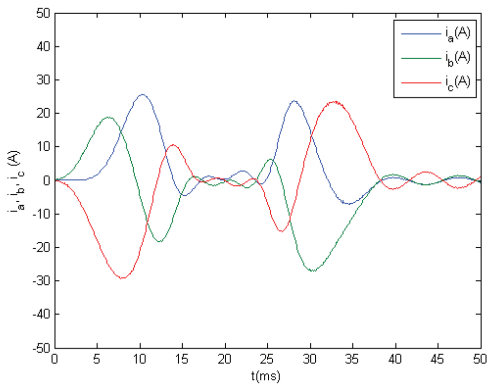

(b)

Figure 6.32: (a) Phase currents for 150 $rad.s^{-1}$ scan (simulation) (b) Phase currents for 150 $rad.s^{-1}$ scan (experimental).

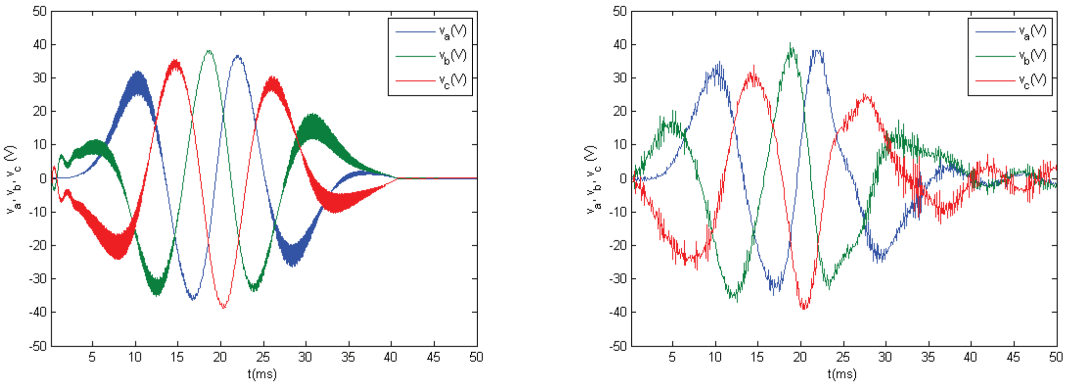

(a) (b)

Figure 6.33: (a) Phase voltages for 150 $rad.s^{-1}$ scan (simulation) (b) Phase voltages for 150 $rad.s^{-1}$ scan (experimental).

6.3.1.2 Second test case

In order to evaluate the impact of the maximum angular speed on the regulation algorithm, the same test treated above has been repeated by limiting the maximum speed at $\omega_{max} = 100\ rad \cdot s^{-1}$. The obtained results are given from Fig. 6.34 to Fig. 6.38. Comparing these results with the previous ones, it can be stated the following remarks:

- The measured magnitudes still follow their references with the same way than the previous test case.

- The errors and the oscillations observed are smaller than those of the previous test case.

6.3.1.3 Synthesis on the wire sanner drive

When looking the global shapes of all the magnitudes observed above (position, speed, currents and voltages), we can conclude that the proposed control seems to operate well regarding the stability aspect. However, the existing errors and oscillations which are more important when the speed of the WS increases, remain to be improved in particular by taking into account the inductor harmonics in the PMSM modeling and control.

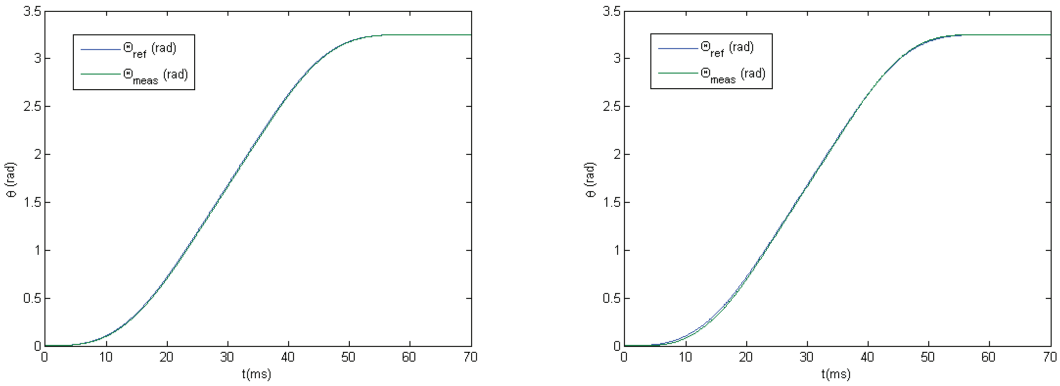

(a) (b)

Figure 6.34: (a) Angular position for 100 $rad.s^{-1}$ scan (simulation) (b) Angular position for 100 $rad.s^{-1}$ scan (experimental).

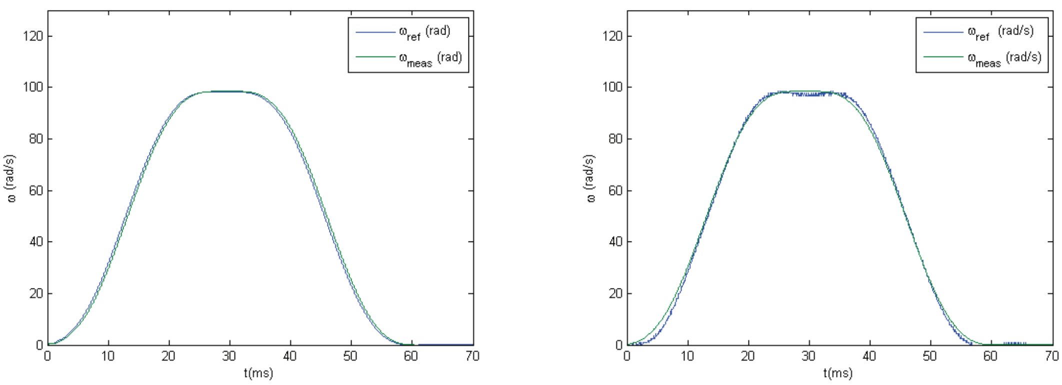

(a) (b)

Figure 6.35: (a) Angular speed for 100 $rad.s^{-1}$ scan (simulation) (b) Angular speed for 100 $rad.s^{-1}$ scan (experimental).

6.3.2 Validation of the linear 3-phase inverter

To assess operation areas of the linear amplifiers (bipolar transistors) we have represented all their operating points corresponding to the tests previously in the plan current-voltage. Fig. 6.39 and 6.40 show the operating area of each linear amplifier respectively in the first and the second test cases.

Comparing these figures to the safe operating area (SOA) provided by the datasheet of manufacturer (25), we conclude that the linear amplifiers reach their limit zone in

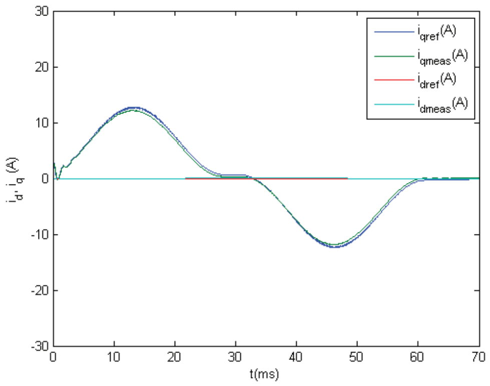

(a) (b)

Figure 6.36: (a) i_q and i_d for 100 $rad.s^{-1}$ scan (simulation) (b) i_q and i_d for 100 $rad.s^{-1}$ scan (experimental).

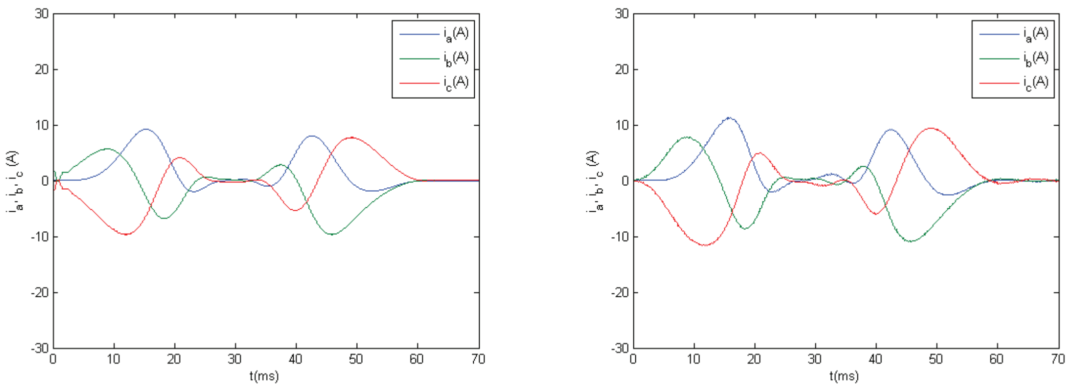

(a) (b)

Figure 6.37: (a) Phase currents for 100 $rad.s^{-1}$ scan (simulation) (b) Phase currents for 100 $rad.s^{-1}$ scan (experimental).

the first case of tests. Otherwise, to fulfil the WS requirements in terms of acceleration and maximum speed the use of two linear amplifiers in parallel for each phases are necessary.

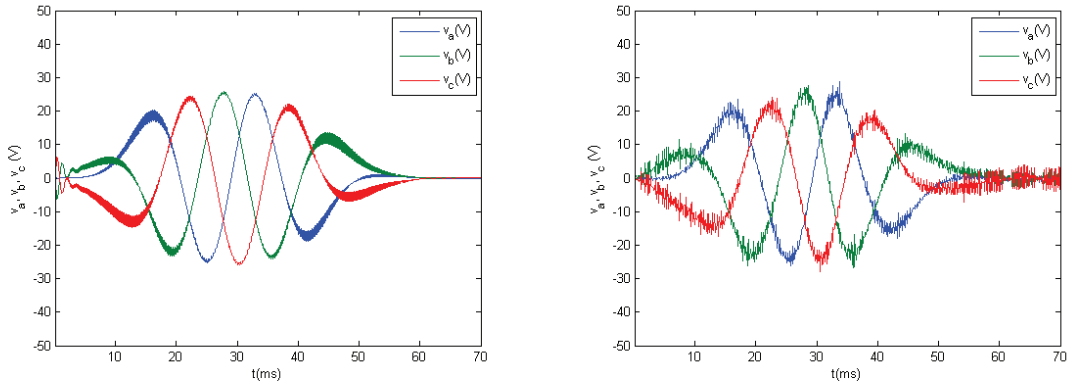

(a) (b)

Figure 6.38: (a) Phase voltages for 100 $rad.s^{-1}$ scan (simulation) (b) Phase voltages for 100 $rad.s^{-1}$ scan (experimental).

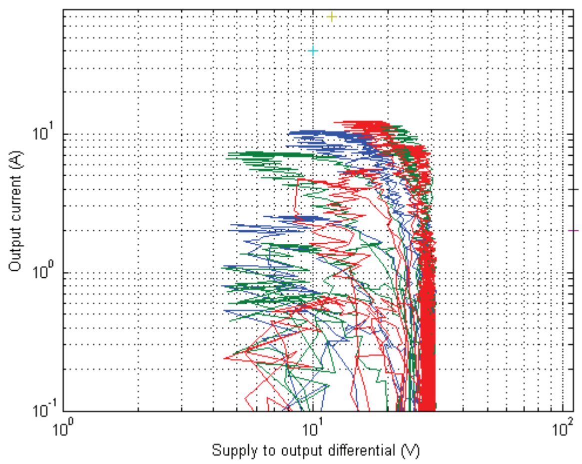

Figure 6.39: Operating area of each linear amplifiers in the first test case $\omega_{max} = 100\ rad \cdot s^{-1}$.

6.4 Synthesis on actuator design

On the basis of the experimental and simulation results obtained through several tests performed on a one scale prototype, we see that no blocking problem has been raised from these laboratory tests. The dimensions chosen for the principal components of the actuator, namely the PMSM, its power supply and position sensors, seem to have been well computed. At this stage of the project, the proposed control strategy gives

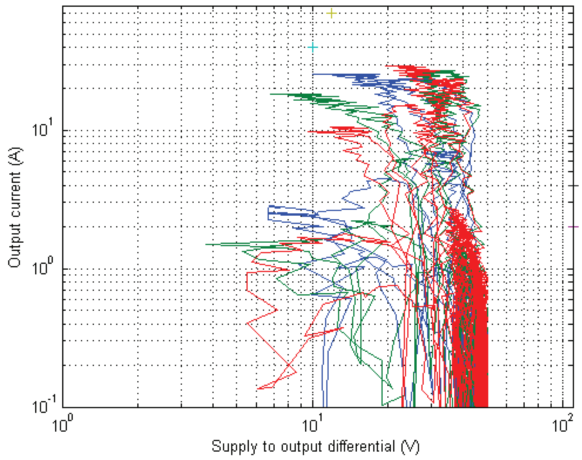

Figure 6.40: Operating area of each linear amplifiers in the first test case $\omega_{max} = 150\, rad \cdot s^{-1}$.

acceptable performances which can be improved by including the real already measured characteristics of the PMSM in the control based model. For these reasons, it is planned to make a first production model for tests in the SPS accelerator. This will be installed in the forthcoming 'Long Shutdown 1' of all CERN accelerators in 2013-14 (Fig. 6.41). Through this present work, it remains only the step of implementation of the WS, which is already forecasted for the upcoming year. Then, the plan is to produce a series of scanners for installation in the second Long Shutdown, scheduled for 2018-19.

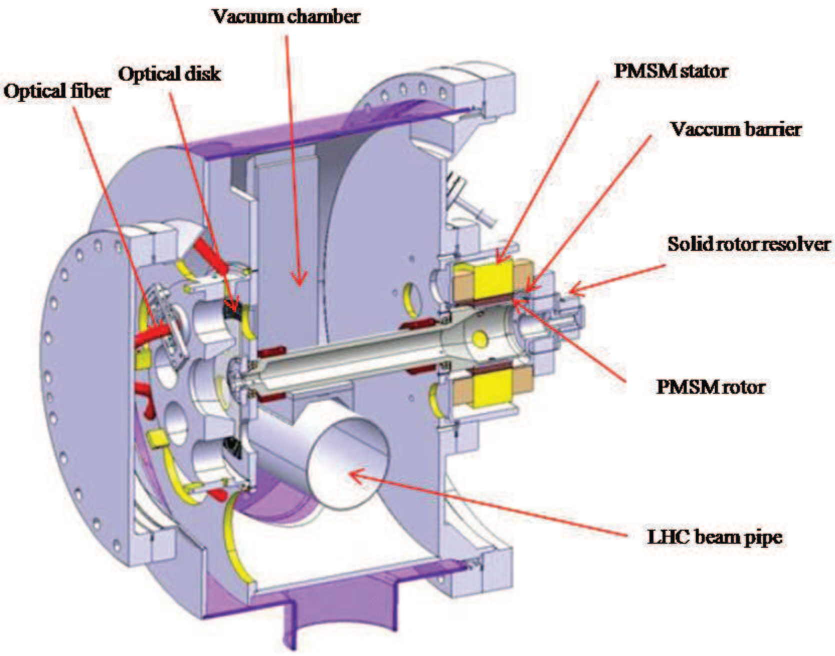

Figure 6.41: 3-D model section through the scanner.

7

Conclusion

This thesis presents and summarizes part of the work carried out within fast and high accuracy wire scanner (WS) project at CERN. The scope of the project was to design the WS actuator including a permanent magnet synchronous motor (PMSM), two angular sensors, a 3-phase power converter part (based on 3 linear amplifiers) and the control system.

The targets of this thesis can be briefly summarized as follows:

- To size and to modify a PMSM motor, by taking into account the requirements in terms of dynamics and environmental constraints.
- To design and to size a 3-phase linear power supply based on 3 power amplifiers.
- To find a solution to integrate a high accuracy angular sensor which is in compliance with environmental constraints inside the vacuum chamber.
- To elaborate a control algorithm to control the motor
- To validate the whole design by the design and the construction of a prototype.

The first step of our research work was to define the motor requirements in terms of drive and load. The mechanical and environmental constraints and their possible impact on the motor have been presented. Then, four kinds of motors have been studied through a multi-criteria comparison. According to this study, the PMSM has been defined to be the most suitable motor for the WS application. Material and configuration to use have been discussed before concluding that a solid steel core rotor can be proposed on which SmCo5 magnets are mounted on the surface. A PMSM has been chosen through an 8 steps of selection process and the rotor has been modified to fulfill the requirements. Finally, an analytic model of the PMSM including the vacuum barrier in its air-gap has been constructed allowing the validation simulation study. Once the motor selected, a solution for the 3-phase linear power supply has been proposed, inspired by the previous WS power supply design. It is based on a 3-phase linear power supply, containing 3 power operational amplifiers used in non-inverting configuration.

The angular position determination is needed with quite different specifications for two purposes: first, the absolute position readout needed for the motor control, which implies an online measurement throughout the full stroke of about $\pi \ rad$; secondly, the position measurement related to the overall precision of the wire scanner system, as it is required to obtain an accurate trajectory of the wire when it crosses the particle beam. Thus, a great part of this PhD contribution has focused on the problematic of the high accuracy position measurement. After extracting the requirements in terms of accuracy, sampling frequency, and environmental and integration constraints from general specification, a market survey has been conducted to find the appropriate technology of sensor which complies with the WS requirements. A design has been proposed based on an optical fiber encoder and a solid rotor resolver. A test setup has been built and the optical fiber encoder design was the subject of a master's study carried out by a student at CERN for one year.

The second most important development of this work was the PMSM control regarding the specification. In this framework, control based models of the motor and its power supply have been presented and a cascaded current, speed and position loops have been designed. To optimize the wire vibration behaviours, four motion profiles have been compared to each other by using a wire vibration model. In order to validate the design of the actuator and its control, a prototype has been designed, built and tested. The obtained experimental results were in a good agreement with the simulation ones, at means that the proposed solution is valid.

Two thesis are underway within the same project; one concentrates on the vibrations influence on the measurement accuracy and the other focuses on the optical fiber encoder accuracy improvement.

In the near future, it is planned to make a first production model for test in the SPS accelerator. This will be installed in the forthcoming 'Long Shutdown 1' of all CERN accelerators in 2013-14. Through the present thesis work, it remains only the step of implementation of the WS, which is already forecasted for the upcoming year. Then, the plan is to produce a serie of scanners for installation in the second Long Shutdown, scheduled for 2018-19.

8

Appendixes

8.1 Datasheet of Parker K500 150 Frameless PMSM

Frameless Kit Motors are the ideal solution for machine designs that require high performance in small spaces. Kit Motors allow for direct integration with a mechanical transmission device, eliminating parts that add size and complexity. A frameless kit consists of a stator, a rotor and various components required to provide the commutation signals necessary for control of the motor (23). The Fig. 8.1 shows some stators and rotors of the frameless Parker motors. Use of Frameless Kit Motors results in a smaller, more reliable motor package. These characteristics are very suitable for the Wire Scanner application.

Figure 8.1: Some Parker frameless servo motors.

The Fig. 8.2 shows the possible overall dimensions of the frameless stators.

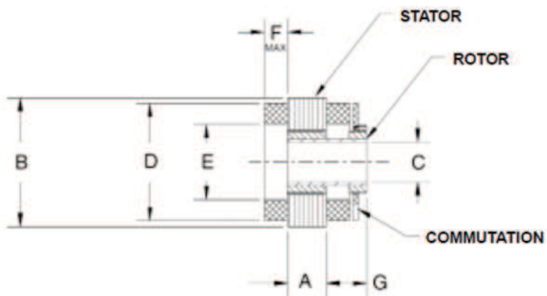

FRAME	B		C		D		E		F		G	
K500	127.05 / 126.95	5.002 / 4.998	68.20 / 68.14	2.685 / 2.675	115.32	4.54	70.6	2.75	20.5	0.81	26.67	1.05

Figure 8.2: Dimensions of the K500 frameless stators.

The Fig. 8.3 shows the Speed/Torque curve of the selected motor and its main parameters.

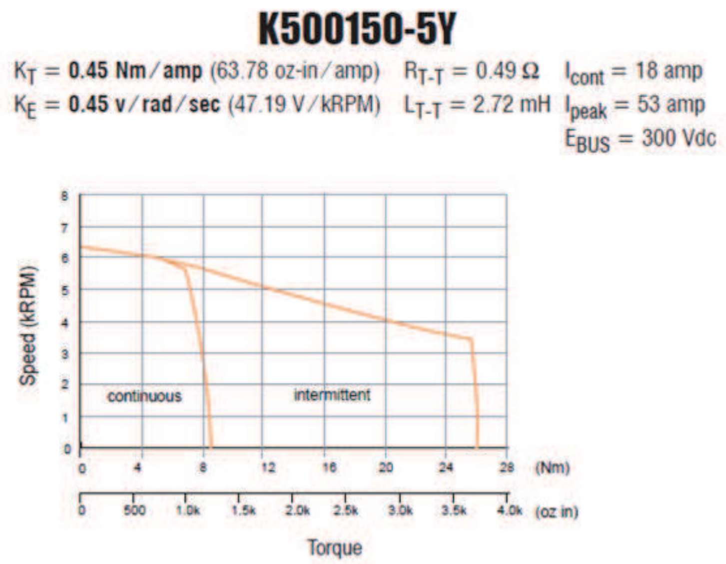

Figure 8.3: Speed/Torque Curve of the selected Parker motor.

8.2 Centrifuge force on the permanent magnets and mechanical fixation sizing

The permanent magnets are submitted to a centrifuge force (36):

$$F_{cm} = m_m \omega^2 R_m \tag{8.1}$$

With m_m is the permanent magnet weight, ω_m is the mechanical speed and R_m is the radius of the rotor with magnets.

Considering A_r as the contact-surface between the magnet and the rotor. The pressure produced by the centrifuge force on each magnet and to be supported by the mechanical fixation is given by :

$$P_m = \frac{F_{cm}}{A_r} = \frac{m_m \omega^2 R_m}{A_r} \tag{8.2}$$

Thus, taking into account the sizing data given in this chapter, the maximum pressure to be wined by the mechanical fixation is the following:

$$P_m = \frac{m_m \times 210^2 \times 0.034}{\frac{\pi \times 0.034^2}{8}} \tag{8.3}$$

The mass of each elementary permanent magnet is given by:

$$m_m = \lambda \times 1.771 \times 1.969 \times 0.38 = \lambda \times 0.85 \tag{8.4}$$

where $\lambda = 8.5\ g.cm^{-3}$ is SmCo density.

Thus,

$$m_m = 7.26\ g \tag{8.5}$$

$$P_m = 23976.31 Nm^{-2} \tag{8.6}$$

By taking a security coefficient of 2, the mechanical fixation has to oppose a pressure resistance two times greater than P_m i.e. $\sim 50\ 000\ Nm^{-2}$.

8.3 Eddy current in vacuum barrier and losses evaluation

8.3.1 Evaluation of the Eddy current in the vacuum barrier

The basis of this model consists in computing the eddy current within the vacuum barrier when it is under the radial rotating magnetic field coming from the stator windings (Fig. 8.4).

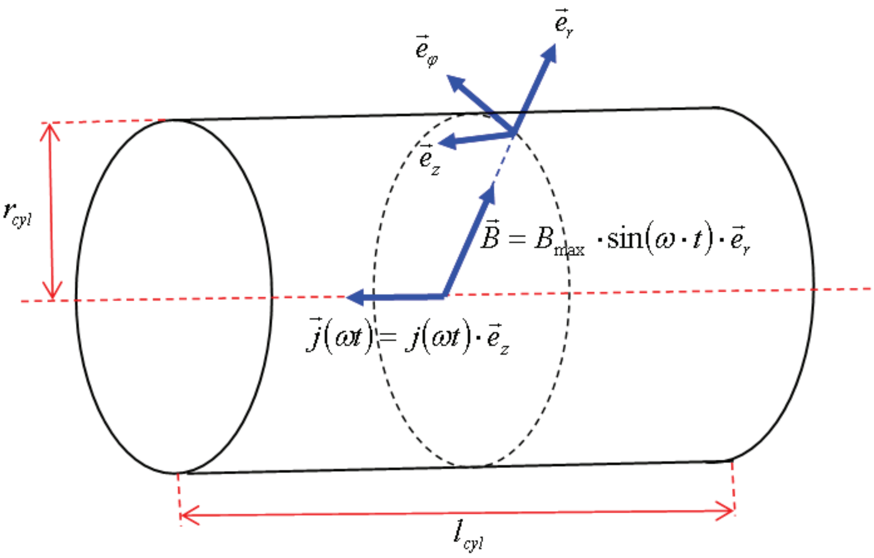

Figure 8.4: The vacuum barrier plunged in the radial flux density of the PMSM.

Indeed, the symmetric three phase stator currents of the PMSM generate the rotation flux density $\overrightarrow{B}$ on which the rotor is fastened to rotate at synchronous speed. Positioned between the stator and the rotor, the vacuum screen will be plunged in this flux density there through it in the radial direction.

$$\overrightarrow{B} = B_{max} \cdot sin(\omega \cdot t) \cdot \overrightarrow{e_r} \tag{8.7}$$

The latter being sinusoidal according to the resulting flux in the vacuum screen can be easily expressed by the following equation:

$$\Phi = \frac{2 \cdot \pi \cdot r_{cyl} \cdot l_{cyl}}{p} \cdot B_{max} \cdot sin(\omega \cdot t) = \Phi_{max} \cdot sin(\omega \cdot t) \tag{8.8}$$

Where, r_{cyl} and l_{cyl} are respectively the radius and the length of the vacuum barrier and p is the PMSM's pole number. The magnitude Φ_{max} is the maximum value of the magnetic flux in the air-gap region of the machine. According to the Faraday's law, one may write,

$$e = \oint_C \overrightarrow{E} \cdot \overrightarrow{dl} = -\frac{d\Phi}{dt} \tag{8.9}$$

And, according to Ohm's law, $\overrightarrow{j} = \sigma \cdot \overrightarrow{E}$ so, one may write:

$$e = \oint_C \frac{\overrightarrow{j}}{\sigma} \cdot \overrightarrow{dl} = -\frac{d\Phi}{dt} \tag{8.10}$$

To determine the circulation of $\overrightarrow{j}$ along the contour 'C', it is necessary to know the direction of the variable on which the current density depends. When assuming that there is no board's effects in the PMSM and in the cylinder, the flux density $\overrightarrow{B}$, the cause of $\overrightarrow{j}$, will be radial and invariant according to the 3D space coordinates (axial, azimuthal and radial coordinates: respectively, z, φ and z). Consequently, one can conclude that $\overrightarrow{j}$ will be independent on the 3D coordinates. On the basis of Lenz's law, specifying that the current density $\overrightarrow{j}$ induced by $\overrightarrow{B}$ will produce a magnetic flux density which opposes the origin responsible of its creation so, this field will be opposite but in the same direction of $\overrightarrow{B}$. In order to generate this radial flux density, the current density has to be in the axial direction and can be written as follows:

$$\overrightarrow{j}(j\omega) = j(j\omega) \cdot \overrightarrow{e_z} \tag{8.11}$$

Thus, we can compute $\overrightarrow{j}$ along 'C':

$$\overrightarrow{j} \cdot \overrightarrow{dl} = j(\omega t)dz \tag{8.12}$$

and,

$$e = \oint_C \frac{\overrightarrow{j}}{\sigma} \cdot \overrightarrow{dl} = \frac{2}{\sigma}\int_0^{l_{cyl}} \overrightarrow{j} \cdot \overrightarrow{dl} = \frac{2}{\sigma}\int_0^{l_{cyl}} j \cdot dz = \frac{2l_{cyl}}{\sigma} j \tag{8.13}$$

Otherwise,

$$-\frac{d\Phi}{dt} = -\frac{2 \cdot \pi \cdot r_{cyl} \cdot l_{cyl} \cdot B_{max} \cdot \omega}{p} \cdot cos(\omega t) = -\Phi_{max} \cdot \omega \cdot cos(\omega t) \tag{8.14}$$

Finally, the relation 8.10 may written as:

$$\frac{2l_{cyl}}{\sigma}j = -\frac{2 \cdot \pi \cdot r_{cyl} \cdot l_{cyl} \cdot B_{max} \cdot \omega}{p} \cdot cos(\omega t) = -\Phi_{max} \cdot \omega \cdot cos(\omega t) \tag{8.15}$$

We conclude that:

$$j = -\frac{\sigma \cdot \pi \cdot r_{cyl} \cdot B_{max} \cdot \omega}{p} \cdot cos(\omega t) = -j_{max} \cdot cos(\omega t) \tag{8.16}$$

We notice that the maximum value of the current density is proportional to the flux density frequency i.e. the frequency of the stator currents of the PMSM.

At the rated frequency

$$j_{max} = \frac{\sigma \cdot \pi \cdot r_{cyl} \cdot B_{max} \cdot \omega}{p} = \frac{\sigma}{2 \cdot l_{cyl}}\Phi_{max} \cdot \omega \tag{8.17}$$

8.3.2 Evaluation of the power losses in the vacuum barrier

The dissipated power by Joule effect in an elementary volume of the metallic cylinder in is given by:

$$\frac{dP(t)}{dv} = \vec{j} \cdot \vec{E} = \frac{j^2}{\sigma} = \sigma \left(\frac{\pi \cdot r_{cyl} \cdot B_{max} \cdot \omega \cdot cos(\omega t)}{p} \right)^2 = \sigma \left(\frac{\Phi_{max} \cdot \omega}{2 \cdot l_{cyl}} \cdot cos(\omega t) \right)^2 \tag{8.18}$$

$$P(t) = \pi \cdot (r_{cyl}^2 - (r_{cyl} - a)^2) \cdot l_{cyl} \cdot \sigma \left(\frac{\pi \cdot r_{cyl} \cdot B_{max} \cdot \omega \cdot cos(\omega t)}{p} \right)^2 = \frac{a \cdot \pi \cdot \sigma}{2 \cdot l_{cyl}} (\Phi_{max} \cdot \omega \cdot cos(\omega t))^2 \tag{8.19}$$

The mean value of $P(t)$ is :

$$P = \frac{\pi \cdot (r_{cyl}^2 - (r_{cyl} - a)^2) \cdot l_{cyl} \cdot \sigma}{2 \cdot p^2} \cdot (\pi \cdot r_{cyl} \cdot B_{max} \cdot \omega)^2 = \frac{\pi \cdot (r_{cyl}^2 - (r_{cyl} - a)^2) \cdot \sigma}{8 \cdot l_{cyl}} \cdot (\Phi_{max} \cdot \omega)^2 \tag{8.20}$$

Where, a is the parameter defining the penetration of the eddy currents in the vacuum barrier and it can be expressed in function of the well-known deep penetration thickness a0 and the barrier thickness e_{cyl}, as following:

$$e = \begin{cases} a_0 \ ; \ a_0 \ < \ e_{cyl} \\ e_{cyl} \ ; \ a_0 \ \geqslant \ e_{cyl} \end{cases} , \ and \ a_0 = \sqrt{\frac{1}{\mu_0 \cdot \sigma \cdot \omega}} \tag{8.21}$$

For a frequency range including all operating points of the WS, the minimum skin thickness $a_0 \approx 2\ cm$. So the parameter a remains constant and equals to e_{cyl}.

- Inox: $\sigma = 1/(79 \cdot 10^{-8})\ \Omega^{-1}m^{-1}$
- $\mu_0 = 1.255663706 \cdot 10^{-6}\ m \cdot kg \cdot s^{-2} \cdot A^{-2}$

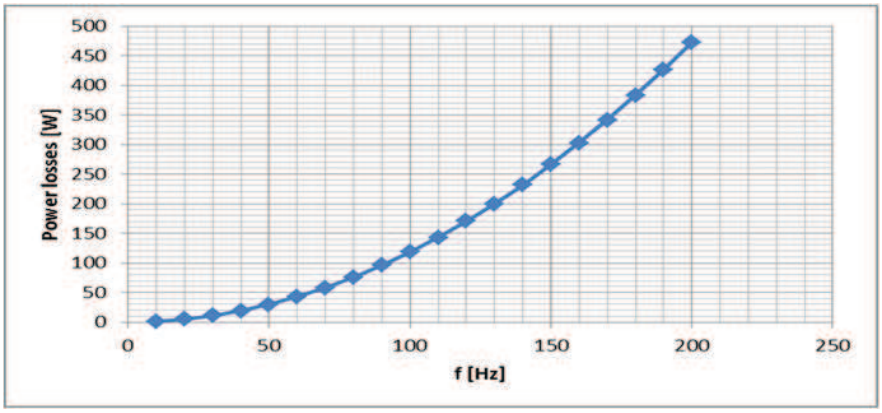

Figure 8.5: Variation of power losses in the vacuum barrier in function of power supply frequency.

The Fig. 8.5 shows the variation of the power losses in a barrier of inox 360LN16 in function of the power supply frequency for $\mu_0 = 1.255663706 \cdot 10^{-6}\ m \cdot kg \cdot s^{-2} \cdot A^{-2}$; $\sigma = 1315789\ \Omega^{-1} \cdot m^{-1}$ $r_{cyl} = 34.5\ mm$; $l_{cyl} = 75\ mm$ and $e_{cyl} = 0.25\ mm$. It can be seen that that the losses at the maximum speed of the WS, which corresponds to $f = 130\ Hz$, are about $170\ W$. These power losses will introduce an additional resistive torque of $0.24\ Nm$.

8.4 Datasheet of the linear amplifier APEX PA52

8.4.1 Description

Because of the EMC environment constraints the use of power switches was prohibited in the power supply of the PMSM acting the WS. So, the classical solution adopted in CERN is to use the power transistor in their linear mode of running. These power electronics components are generally called 'the linear amplifiers'. So, among the available linear amplifiers in the market, the PA52 component has performances very close to those needed by the WS application. The PA52 (Fig. 8.6) is a MOSFET power operational amplifier that extends the performance limits of power amplifiers in slew rate and power bandwidth, while maintaining high current and power dissipation ratings.

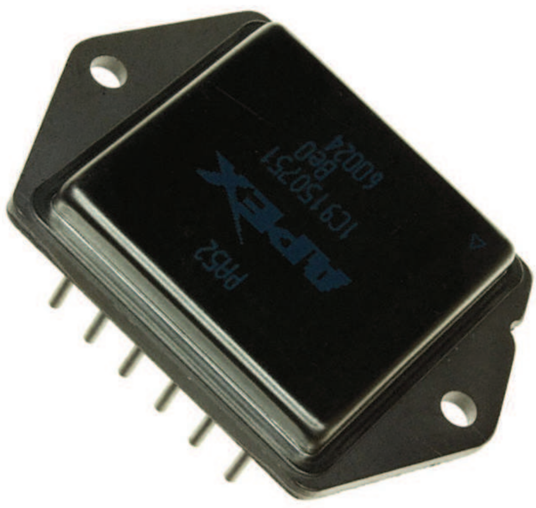

Figure 8.6: Picture of the linear amplifier APEX PA52.

8.4.2 Operating areas

The Fig. 8.8 shows the limits of the operating areas of the linear amplifiers used in our prototype. For the performed laboratory tests we have voluntarily limited the maximum speed of the PMSM to 150 $rad \cdot s^{-1}$ in order to avoid the destruction risk of the linear amplifiers which are very fragile and very expensive. So, according to the output characteristic given in Fig. 8.8, we conclude that using two linear amplifiers in parallel is necessary to ensure a good and secure functioning of the actuator.

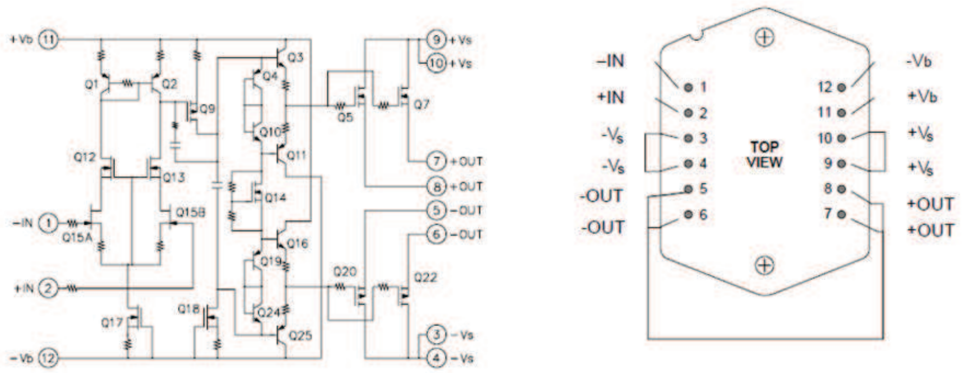

Figure 8.7: Equivalent schematic and external connections of the APEX PA52.

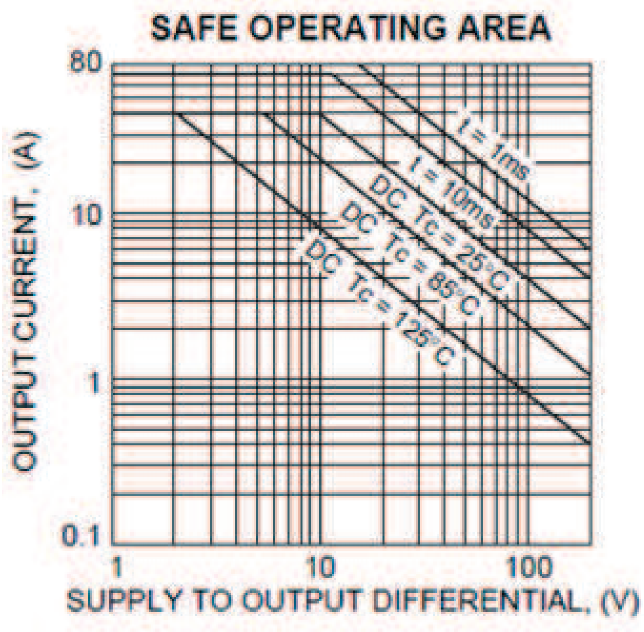

Figure 8.8: The rated operating areas the linear amplifiers.

Bibliography

[1] F. Roncarolo, "Accuracy of the transverse emittance measurements of the CERN large hadron collider," Ph.D. dissertation, Lausanne, 2005. [Online]. Available: http://library.epfl.ch/theses/?nr=3402 xii, 15, 20, 23

[2] M. Sapinski, "Model of carbon wire heating in accelerator beam. oai:cds.cern.ch:1123363," CERN, Geneva, Tech. Rep. CERN-AB-2008-030-BI, Jul 2008. xii, 24

[3] J. B. Milind Paradkar, "Design of a high performance ferrite magnet-assisted synchronous reluctance motor for an electric vehicle," *IECON12*. xiii, 45

[4] J. L. Sirvent Blasco, J. Emery, and J. M. Azorin Poveda, "Design of an optical fibre based angular position sensor for wire scanners complying with ultra-high vacuum, high temperature and radiation conditions of the cerns accelerators," Tech. Rep., 2012, presented 2012. xiv, 81, 85, 87

[5] B. Dehning, "Private communication," 2010. xix, 33

[6] F. Roncarolo, "Transverse emittance measurement and preservation in the lhc chain," March 2009. 12

[7] M. Sapinski, F. Cerutti, K. Dahlerup-Petersen, B. Dehning, j. Emery, A. Ferrari, A. Guerrero, E. B. Holzer, M. Koujili, A. Lechner, E. Nebot, M. Scheubel, J. Steckert, A. Verweij, and J. Wenninger, "Lhc magnet quench test with beam loss generated by wire scan. oai:cds.cern.ch:1379465," no. CERN-ATS-2011-062, p. 3 p, Sep 2011. 13, 22

[8] A. Lokhovitskiy, J. Koopman, and A. Guerrero, "Fast wire scanner calibration. oai:cds.cern.ch:1183402," CERN, Geneva, Tech. Rep. CERN-BE-2009-020, May 2009. 18

[9] E. Huttel, "Materials for accelerator vacuum systems," ANKA, Forschungszentrum Karlsruhe, Germany, Tech. Rep., Mai 1994. 25, 42, 45

[10] W. Voss, *A Comprehensible Guide to Servo Motor Sizing*, copperhill technologies corporation, greenfield, massachusetts ed., 2007. 32

[11] D. Ramos, "Cylindrical shell with external pressure according to en 13445-3:2002," March 2009. 34

[12] J. Puranen and L. teknillinen yliopisto, *Induction Motor Versus Permanent Magnet Synchronous Motor in Motion Control Applications: A Comparative Study*, ser. Acta Universitatis Lappeenrantaensis. Lappeenranta University of Technology, 2006. [Online]. Available: http://books.google.fr/books?id=voY_MgAACAAJ 35, 36, 42

[13] D. Fodorean, *Conception et réalisation d'une machine synchrone à double excitation: application à l'entraînement direct*, 2005. [Online]. Available: http://books.google.fr/books?id=izWEtgAACAAJ 35, 36, 42, 43

[14] L. Mutrel, *Électrotechnique: le moteur asynchrone*, ser. Technosup (Paris). Ellipses, 1999. [Online]. Available: http://books.google.fr/books?id=YcY5PQAACAAJ 36, 37

[15] I.-A. Viorel, L. Szabo, and L. Strete, "Speed-thrust control of a double sided linear switched reluctance motor (dsl-srm)," in *Electrical Machines, 2008. ICEM 2008. 18th International Conference on*, sept. 2008, pp. 1 –6. 37

[16] I. A. V. Nicoleta MEDREA, "Switched reluctance motors with concentrated stator windings and salient poles of different shape on rotor," *Annals of the University of Craiova, Electrical Engineering series*, vol. No. 32, 2008; ISSN 1842-4805. 37

[17] B. Multon, "Conception et alimentation électronique des machines réluctance variable double saillance," Ecole Normale Supérieure de Cachan, Cachan, Tech. Rep., Mai 1994. 38

[18] M. F. Marek Stulrajter, Valeria Hrabovcova, "Permanent magnets synchronous motor control theory," *Journal of ELECTRICAL ENGINEERING*, vol. 58, pp. 79–84. 39, 44

[19] A. Consoli, G. Scarcella, G. Scelba, A. Testa, and D. Triolo, "Sensorless rotor position estimation in synchronous reluctance motors exploiting a flux deviation approach," in *Industry Applications Conference, 2006. 41st IAS Annual Meeting. Conference Record of the 2006 IEEE*, vol. 4, oct. 2006, pp. 1989 –1994. 39

[20] H. Hofmann, S. Sanders, and A. EL-Antably, "Stator-flux-oriented vector control of synchronous reluctance machines with maximized efficiency," *Industrial Electronics, IEEE Transactions on*, vol. 51, no. 5, pp. 1066 – 1072, oct. 2004. 39

[21] G. Pellegrino, E. Armando, P. Guglielmi, and A. Vagati, "A 250kw transverse-laminated synchronous reluctance motor," in *Power Electronics and Applications, 2009. EPE '09. 13th European Conference on*, sept. 2009, pp. 1 –10. 39

[22] C. B. Jean-Paul LOUIS, "Commande numérique des machines synchrones," *Les Techniques de l'Ingénieur*, vol. D 3 644, pp. 1–22. 45

[23] *Frameless Kit Motors Product Manual*, Parker. 50, 150

[24] *Frameless Kit Motors Catalogue 192-062013 N1 UK, Version 1 January-2006*, Parker. 50

[25] *Power Operational Amplifiers PA52 - PA52A*, Apex Microtechnology, 2 2001. 54, 92, 140

[26] M. Koujili, Y. Ait-Amirat, B. Dehning, A. Djerdir, J. Emery, and J. Alvarez, "Design of an actuator for the fast and high accuracy wire scanner," in *Electric Machines Drives Conference (IEMDC), 2011 IEEE International*, may 2011, pp. 1450 –1455. 60

[27] "International vocabulary of metrology basic and general concepts and associated terms (vim)," Tech. Rep. 66

[28] D. Jouve and D. Bui, "Influence of the motor feedback sensor on ac brushless servo drive performances," May 2003. 66

[29] D. T. Robinson, "A new absolute inductive transducer for brushless servomotors," September 1995. 71

[30] "The farrand electrosyn transducer," Tech. Rep. 77

[31] D. Horwitz, "Fiber optic rotary encoder technology offers emi immunity for motion control application in harsh environments. two case studies." *Micronor Inc.* 78

[32] *Increasing Output Swing in Power Operational Amplifiers*, Apex Microtechnology, 10 2012. 93

[33] D. J. A. Quang, Nguyen Phung, *Vector Control of Three-Phase AC Machines*, springer ed., 2008. 97, 98

[34] H. Li, M. Le, Z. Gong, and W. Lin, "Motion profile design to reduce residual vibration of high-speed positioning stages," *Mechatronics, IEEE/ASME Transactions on*, vol. 14, no. 2, pp. 264 –269, april 2009. 102

[35] J. H. Alvarez, "2 dof wire dynamic model," CERN, Geneva, Tech. Rep. CERN EDMS Document Id 1246770. 104

[36] M. Hecquet and P. Brochet, "Time variation of forces in a synchronous machine using electric coupled network model," *Magnetics, IEEE Transactions on*, vol. 34, no. 5, pp. 3214 –3217, sep 1998. 151